
THE UNIVERSITY
*of* ADELAIDE

Faculty of Sciences
School of Physical Sciences

# Fast Simulation and a Search for Four-top-quark Production with the ATLAS Experiment

Albert Xing Yi Kong

MPhil Thesis

9 April 2020

# Contents

# Abstract

The Standard Model of particle physics is one of the most successful theories in physics. However there is still a range of natural phenomena that it is unable to explain. This thesis presents a measurement of Standard Model production of four top quarks, a rare process that is sensitive to influences from potential beyond Standard Model processes, using data from the ATLAS experiment at CERN's Large Hadron Collider (LHC). This thesis also documents a fast simulation software package that was developed for the ATLAS Fast Tracker system, which will be instrumental in adapting to the coming High-Luminosity LHC era.

# Statement of Originality

I certify that this work contains no material which has been accepted for the award of any other degree or diploma in my name, in any university or other tertiary institution and, to the best of my knowledge and belief, contains no material previously published or written by another person, except where due reference has been made in the text. In addition, I certify that no part of this work will, in the future, be used in a submission in my name, for any other degree or diploma in any university or other tertiary institution without the prior approval of the University of Adelaide and where applicable, any partner institution responsible for the joint award of this degree.

I give permission for the digital version of my thesis to be made available on the web, via the University's digital research repository, the Library Search and also through web search engines, unless permission has been granted by the University to restrict access for a period of time.

I acknowledge the support I have received for my rese
of an Australian Government Research Training Program

The University of Adelaide,
5th February 2020

Albert Kong

# Acknowledgements

Writing a thesis is no trivial undertaking, even at the level for a Master of Philosophy. I would like to take this opportunity to acknowledge everyone who has supported me in this endeavour. Many thanks to my supervisor Paul Jackson for his guidance throughout this journey and his ever-lasting faith in my abilities. Thanks to our visiting academic Frédéric Déliot; without his knowledge and insight much of my work for the four-top-quark analysis would not have been possible. Thanks to ATLAS computing experts Maximilian Swiatlowski, Jan Kuechler, and John Baines for putting with up the multitude of questions I fired at them over email and for patiently pointing out my mistakes and misunderstandings. Thanks to my co-supervisor Martin White for his support during my Masters program. I would also like to thank my fellow graduate students and ATLAS collaborators Abhishek Sharma, Emily Filmer, and Jason Oliver for the discussions we shared on how to write up the various parts of our theses. Finally, I would like to thank my parents for their love and patience during this latest endeavour; the foundation you provide is what makes everything possible.

Chapter 1

# Introduction

It is an exciting time to be in particle physics. With CERN's Large Hadron Collider (LHC) pushing the frontiers of high energy physics, there is a wealth of information to be gleaned about the innermost workings of the universe. The ongoing upgrades to the LHC have resulted in a steady increase in the instantaneous luminosity it can deliver to experiments. However this increase in instantaneous luminosity also presents new challenges to experiments in the form of more simultaneous interactions at any given time.

The ATLAS experiment is one of several experiments at the LHC. Its approach to handling this high luminosity environment has included the use of fast tracking. Tracking information is vital to understanding the collisions that occur within the ATLAS detector. Event reconstruction processes such as jet tagging and particle momenta determination rely on tracking information to produce optimal results. The previous software-based tracking system used by the ATLAS experiment is unfortunately unable to keep up with the high luminosity environment, as the time cost for tracking increases exponentially with detector occupancy. The Fast Tracker system was a massively parallel hardware system designed to overcome the previous computational bottleneck to provide timely and extensive tracking. This in turn provided significant benefits to the various physics analyses performed on data recorded by the ATLAS experiment.

In Chapter 2, an introduction to the Standard Model of particle physics is given, with particular emphasis on the concepts pertaining to the work done for the M.Phil and documented in subsequent chapters. Chapter 3 introduces the ATLAS detector and some of the reconstruction techniques used in physics analyses. Chapter 4 describes the Fast Tracker system and the simulation software that I developed for it. Chapter 5 documents an analysis performed on data recorded by the ATLAS experiment that measures the cross section of Standard Model production of four top quarks. Particular detail is provided on my contributions to the development of control and validation regions for the analysis. Chapter 6 highlights the synergies between the simulation development that I performed for the Fast Tracker and the four-top-quark analysis, then closes with a brief statement regarding future directions for this work.

Chapter 2

# The Standard Model

The Standard Model of particle physics [1–3] is a mathematical description of the fundamental particles that constitute all known visible matter in the universe. It describes the action of three of the four forces between these particles: the electromagnetic force, the strong force, and the weak force. The fourth force, gravity, is much weaker than the other three and is assumed to have negligible effect within the domain of particle physics. The Standard Model has been scrutinised by a variety of experimental tests in the years since its development in the 1950s and 1960s. Despite such scrutiny, the Standard Model has been remarkably successful in predicting experimental results to a high degree of precision (see Figure 2.2). This has led to it being described as one of the most successful scientific theories in history.

## 2.1 Particle Content

The Standard Model classifies elementary particles under two broad categories: fermions and bosons. Fermions have half integer spin and obey Fermi-Dirac statistics [6, 7], while bosons have integer spin and obey Bose-Einstein statistics [8].

Fermions can be further subdivided into quarks and leptons, each of which are arranged into three generations of increasing mass. Each generation of quark has an up-type quark with electric charge $+2/3$ and a down-type quark with electric charge $-1/3$. In order of generation, the quark flavours in the Standard Model are the up ($u$) and down ($d$), charm ($c$) and strange ($s$), top ($t$) and bottom ($b$). The leptons consist of three charged species with electric charge $-1$ and three neutral species. Each generation contains one of each. In order of generation, these are: the electron ($e$) and electron neutrino ($\nu_e$), muon ($\mu$) and muon neutrino ($\nu_\mu$), tau ($\tau$) and tau neutrino ($\nu_\tau$). Each of these particles also has an associated anti-particle. The anti-particle is typically denoted with a bar over the usual symbol, for example $\bar{t}$ for an anti-top quark.

The bosons are the mediators of interactions between fermions. A force between two fermions can be understood to be an exchange of the corresponding boson between those fermions. The electromagnetic force acts only on electrically charged particles; it is mediated by the electrically neutral and massless photon ($\gamma$). The strong force acts only on particles with colour charge; it is mediated by the massless and electrically neutral gluon ($g$). As the gluon also carries colour charge, it is able

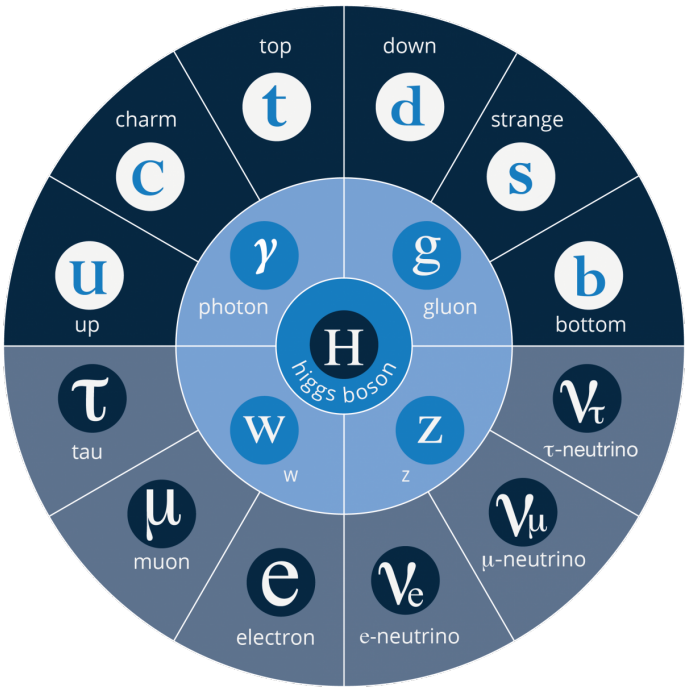


Figure 2.1: Particle content of the Standard Model [4]. Anti-particles are omitted for clarity.

to interact with itself. This leads to several interesting phenomena and has sparked the development of Quantum Chromo-Dynamics (QCD), an entire field dedicated to studying strong force interactions. The weak force can act on any fermion, and is mediated by three massive bosons: the $W^+$, $W^-$ and $Z^0$, which have electric charge $+1$, $-1$ and 0 respectively. The Higgs boson has a special role in the Standard Model, as the Higgs field is required to give mass to the other fundamental particles.

Figure 2.1 depicts the particle content of the Standard Model.

### 2.1.1 Feynman Diagrams

When calculating the probability amplitude of a particular process in the Standard Model, there are many possible pathways from the given initial state to the desired final state. Each of these pathways involve different interactions between different elementary particles, and contribute varying amounts to the total probability amplitude. Feynman diagrams depict these individual pathways graphically and allow a more intuitive understanding of the interactions taking place than otherwise might be gained from only looking at the mathematical expression. Fermions are typically represented by a solid line with an arrow indicating whether it is a particle or anti-particle. Gluons are represented by spiral lines while the other bosons are represented by either sinusoidal or dashed lines. The intersection points between different types of lines are called vertices.

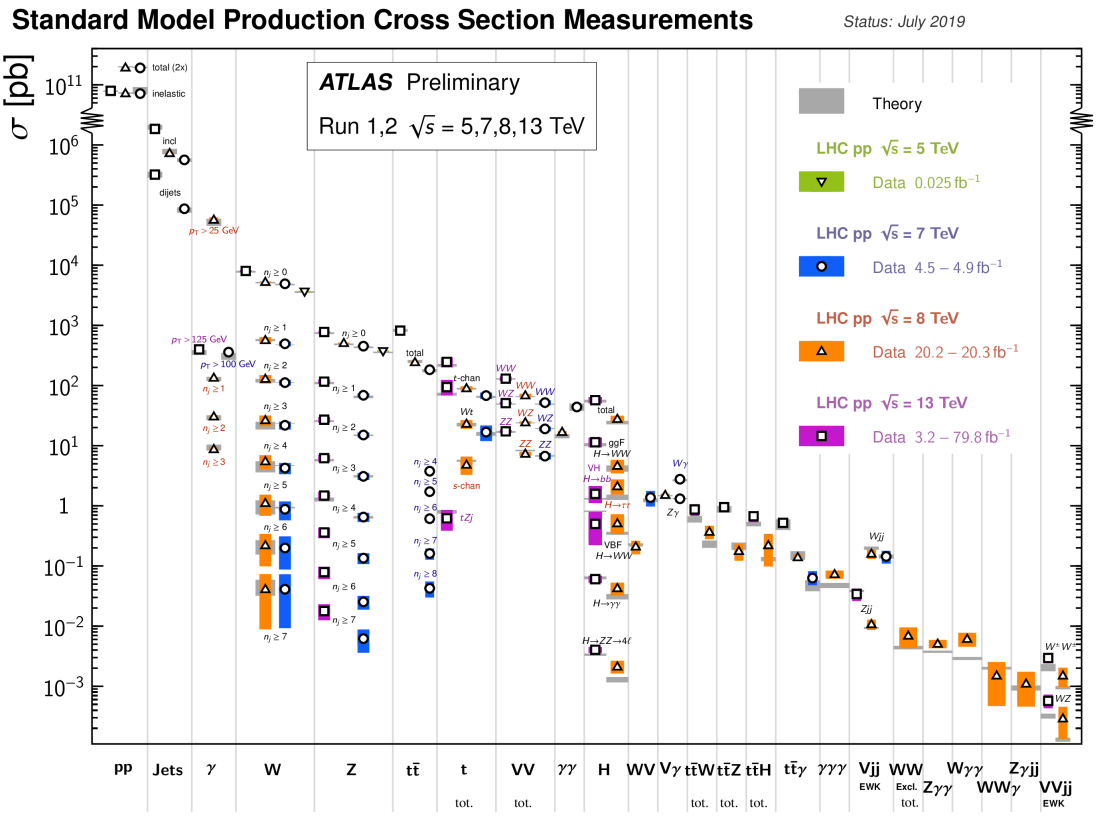


Figure 2.2: Cross section measurements and theoretical predictions for a range of Standard Model processes [5]. Note the strong agreement between theory and experiment for every measured process.

## 2.2 Mathematical Formulation

The Standard Model is formulated as a gauge quantum field theory, with gauge group given by the product of $SU(3)$ colour, $SU(2)$ isospin and $U(1)$ hypercharge. The fields used in the Standard Model are the fermion fields $\psi$; the electroweak boson fields $W^1, W^2, W^3$ and $B$; the gluon field $G_a$; and the Higgs field $\varphi$. These fields are the fundamental objects in SM theory, with the particles described in Section 2.1 being excitations of the corresponding fields. Each field has a set of quantum numbers associated with it that describe its interactions with other fields. The $W$ fields interact based on the weak isospin quantum number; the $B$ field interacts based on the weak hypercharge quantum number; and the $G_a$ fields interact based on the colour quantum numbers. These gauge fields will interact with another field exactly when that second field has a non-zero quantum number associated with the gauge field, so the $B$ field for instance interacts with any field with non-zero hypercharge.

### 2.2.1 Symmetries and the Lagrangian

The behaviour and interactions of objects in the Standard Model are defined by its lagrangian and the symmetries in its lagrangian. As given by Noether's theorem, symmetries lead to conserved quantities, while the Euler-Lagrange field equations,

$$\partial_\mu \frac{\partial \mathcal{L}}{\partial(\partial_\mu \Phi)} = \frac{\partial \mathcal{L}}{\partial \Phi}\,, \tag{2.1}$$

generate the classical equations of motion.

The full Standard Model lagrangian can be written as

$$\mathcal{L}_{\text{SM}} = \mathcal{L}_{\text{QCD}} + \mathcal{L}_{\text{EW}} + \mathcal{L}_{\text{Higgs}}\,, \tag{2.2}$$

where the terms on the right hand side refer to the three main sectors in the Standard Model: the quantum chromodynamical, electroweak, and higgs sectors respectively.

### 2.2.2 The QCD Sector

To construct the QCD lagrangian, consider the free lagrangian for quark fields $\psi$ as given by the Dirac equation,

$$\mathcal{L}_{\text{free}} = \bar{\psi}(i\gamma^\mu \partial_\mu - m)\psi\,. \tag{2.3}$$

We require the quark fields to be invariant under local SU(3) transformations

$$\psi(x) \to U(x)\psi(x)\,, \tag{2.4}$$

where $U(x) = \exp\left[-i\theta_a(x)\frac{\lambda_a}{2}\right]$, $\lambda_a$ are the Gell-Mann matrices and $\theta_a(x)$ is a real function with $a = 1, 2, \cdots, 8$. For local gauge invariance to be satisfied, we exchange

the usual derivative for the covariant derivative

$$D_\mu = \partial_\mu - igA_\mu(x)\,, \tag{2.5}$$

where $g$ is a dimensionless coupling strength and we have introduced the $SU(3)$ gauge fields $A^a_\mu(x)$ to define

$$A_\mu(x) = \sum_{a=1}^{8} \frac{\lambda_a}{2} A^a_\mu(x)\,. \tag{2.6}$$

These gauge fields give rise to 8 gauge bosons that we refer to as gluons - one for each generator of $SU(3)$. The locally gauge invariant QCD lagrangian can be written as

$$\mathcal{L}_{\text{QCD}} = \bar{\psi}(i\gamma^\mu D_\mu - m)\psi - \frac{1}{2}\,\text{tr}\{G_{\mu\nu}G^{\mu\nu}\}\,, \tag{2.7}$$

where the gluon field tensor $G_{\mu\nu}$ is defined analogously to the electromagnetic field strength tensor, but with an additional term added to maintain gauge invariance:

$$G^a_{\mu\nu}(x) = \partial_\mu A^a_\nu(x) - \partial_\nu A^a_\mu(x) + g\, f_{abc} A^b_\mu(x) A^c_\nu(x)\,. \tag{2.8}$$

If we compare this to the free lagrangian in Equation 2.3:

$$\mathcal{L}_{\text{QCD}} = \bar{\psi}(i\gamma^\mu\partial_\mu + g\gamma^\mu A_\mu(x) - m)\psi - \frac{1}{2}\,\text{tr}\{G_{\mu\nu}G^{\mu\nu}\} \tag{2.9}$$

$$= \mathcal{L}_{\text{free}} + gA_\mu(x)\bar{\psi}\gamma^\mu\psi - \frac{1}{2}\,\text{tr}\{G_{\mu\nu}G^{\mu\nu}\}\,, \tag{2.10}$$

we see that requiring the lagrangian to have local gauge symmetry leads to the introduction of an interaction term between the fermion and the gluon fields (and in this case, a self-interaction term for the gluon fields). Note that there is no mass term for the gluon field in the lagrangian, nor can one be added without violating gauge invariance. This is a general result for gauge bosons introduced via the principle of gauge invariance, and will need to be addressed when formulating a theory containing massive gauge bosons.

### 2.2.3 The Electroweak Sector

The electroweak sector is a unification of the electromagnetic and weak interactions under a single gauge group $SU(2)_L \times U(1)$. Here the subscript L indicates the $SU(2)$ group associated with the weak interaction is chiral and acts only on left-handed fermion fields. The lagrangian for the electroweak sector can be derived in a similar fashion to the QCD sector, however there are some complications. The first issue we encounter is that mass terms for the fermion fields are forbidden in a chiral theory as the mixing of the two chiralities would violate gauge invariance. This suggests we can only have a massless chiral theory. As we have seen previously, imposing gauge

invariance upon a free lagrangian would generate the desired interaction terms with the three gauge fields $W^1_\mu, W^2_\mu, W^3_\mu$ from $SU(2)$ and $B_\mu$ from $U(1)$, but these gauge fields must be massless. We would like to associate the $B_\mu$ field with the photon, but $B_\mu$ couples to all leptons (as they have non-zero hypercharge) whereas the photon does not couple to neutrinos. This leads us to construct physical boson fields as linear combinations of the $W_\mu$ and $B_\mu$ fields to prevent the photon from coupling to neutrinos:

$$\begin{pmatrix} A_\mu \\ Z_\mu \end{pmatrix} = \begin{pmatrix} \cos\theta_w & \sin\theta_w \\ -\sin\theta_w & \cos\theta_w \end{pmatrix} \begin{pmatrix} B_\mu \\ W^3_\mu \end{pmatrix}, \tag{2.11}$$

$$W^\pm_\mu = \frac{1}{\sqrt{2}}\left(W^1_\mu \mp i W^2_\mu\right), \tag{2.12}$$

where we are now able to identify $A_\mu$ as the photon field, $Z_\mu$ as the $Z$ boson field, and $W^\pm_\mu$ as the $W$ boson fields. Here $\theta_w$ is the electroweak mixing angle, which is chosen such that $A_\mu$ decouples from neutrinos but otherwise couples to left and right handed leptons equally. As the $W$ boson fields are composed only of $SU(2)_L$ gauge fields, they do not couple to right handed fermions. On the other hand, the $Z$ boson has an asymmetric coupling to left and right handed fermions due to it being a composition of the $B_\mu$ and $W^3_\mu$ fields.

### 2.2.4 The Higgs Sector and Electroweak Symmetry Breaking

Experimentally the $W^\pm$ and $Z^0$ bosons are known to be massive, but as mentioned at the end of Section 2.2.2, it is not possible to add a mass term to the electroweak lagrangian to account for this. Therefore a different mechanism will be required for providing the gauge bosons with mass. In 1964, Englert, Brout and Higgs were able to incorporate such a mechanism into electroweak theory [9, 10]. That mechanism has since become known as the Higgs mechanism.

We start by considering a scalar field $\phi(x)$ with lagrangian

$$\mathcal{L}_H = \partial_\mu \phi^\dagger \partial^\mu \phi - \mu^2 \phi^\dagger \phi - h(\phi^\dagger \phi)^2 . \tag{2.13}$$

For the field to have a stable ground state, the potential must be bounded from below so $h > 0$. There are two possibilities for $\mu^2$:

- $\mu^2 \geq 0$, in which the potential has only a trivial minimum at $\phi = 0$.
- $\mu^2 < 0$, in which there is a continuous set of possible ground states $\phi_0$ defined by

$$|\phi_0| = \sqrt{\frac{-\mu^2}{2h}} = \frac{v}{\sqrt{2}}, \tag{2.14}$$

where we let $v = \sqrt{-\mu^2/h}$ for convenience. The second case is very interesting, as there are infinitely many possible ground states, however just one of those must be

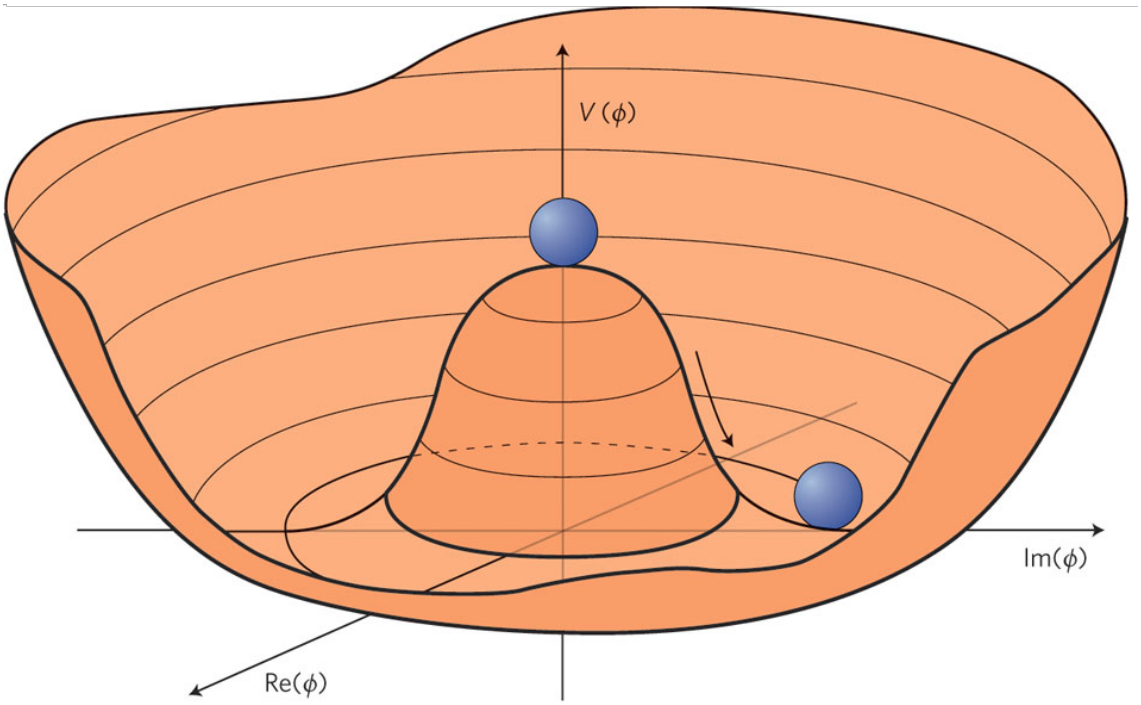


Figure 2.3: A visualisation of the Higgs potential and spontaneous symmetry breaking [11]. A ball placed on the local maximum at the origin would like to fall down into the valley where the potential is lower. Each direction is equally likely at first, but after the ball falls in one direction that initial symmetry is lost.

chosen by the system to be the "true" ground state. This phenomenon is known as *spontaneous symmetry breaking*. See Figure 2.3 for an illustration of this situation.

Now consider the equivalent gauged lagrangian

$$\mathcal{L} = (D_\mu \phi)^\dagger D^\mu \phi - \mu^2 \phi^\dagger \phi - h(\phi^\dagger \phi)^2 \,, \tag{2.15}$$

where $h > 0$, $\mu^2 < 0$, $\phi$ is now an $SU(2)_L$ doublet

$$\phi(x) = \begin{pmatrix} \phi^{(+)}(x) \\ \phi^{(0)}(x) \end{pmatrix} , \tag{2.16}$$

and the covariant derivative is defined as

$$D_\mu \phi = \left[ \partial_\mu + ig \frac{\sigma_i}{2} W_\mu^i + ig' y_\phi B_\mu \right] \phi \,, \tag{2.17}$$

for invariance under $SU(2)_L \times U(1)$ transformations. Once again, we have an infinite set of possible ground states defined by

$$\left| \langle 0 | \phi^{(0)} | 0 \rangle \right| = \sqrt{\frac{-\mu^2}{2h}} = \frac{v}{\sqrt{2}} \,. \tag{2.18}$$

Note that only the neutral field can acquire a vacuum expectation value due to conservation of electric charge. We now choose a ground state and parametrise the scalar doublet in terms of that state:

$$\phi(x) = \exp\left\{ i\frac{\sigma_i}{2}\theta^i(x) \right\} \frac{1}{\sqrt{2}} \begin{pmatrix} 0 \\ v + H(x) \end{pmatrix}, \tag{2.19}$$

where $H(x)$ and the three $\theta^i(x)$ are real fields. As the lagrangian is invariant under local $SU(2)_L$ transformations, the exponential term can be eliminated by choosing the unitary gauge $\theta^i(x) = 0$. If we now substitute this parametrised form of $\phi(x)$ into the derivative term of the lagrangian, we obtain

$$(D_\mu \phi)^\dagger D^\mu \phi = \frac{1}{2}\partial_\mu H \partial^\mu H + (v+H)^2 \left\{ \frac{g^2}{4} W_\mu^\dagger W^\mu + \frac{g^2}{8\cos^2\theta_w} Z_\mu Z^\mu \right\}, \tag{2.20}$$

where we have replaced the gauge fields with the physical boson fields for clarity (see Section 2.2.3). Notice that this generates quadratic mass terms for the $W$ and $Z$ bosons, resolving one of our previous issues.

To address the remaining issue of missing fermion masses, we consider a gauge-invariant interaction term between our scalar doublet and the fermions:

$$\mathcal{L}_{H,int} = -c_1 \left(\bar{u}, \bar{d}\right)_L \begin{pmatrix} \phi^{(+)} \\ \phi^{(0)} \end{pmatrix} d_R - c_2 \left(\bar{u}, \bar{d}\right)_L \begin{pmatrix} \phi^{(0)*} \\ -\phi^{(-)} \end{pmatrix} u_R - c_3 \left(\bar{\nu}_e, \bar{e}\right)_L \begin{pmatrix} \phi^{(+)} \\ \phi^{(0)} \end{pmatrix} e_R + \cdots \tag{2.21}$$

Using the same ground state parametrisation and choosing the unitary gauge simplifies the interaction lagrangian to the following form:

$$\mathcal{L}_{H,int} = -\frac{1}{\sqrt{2}}(v+H)\left\{ c_1\, \bar{d}d + c_2\, \bar{u}u + c_3\, \bar{e}e \right\}. \tag{2.22}$$

Once again, we observe that this generates quadratic mass terms for each of the fermions.

## 2.3 Top Physics

An interesting consequence of the Higgs mechanism for mass generation is that the heaviest fermions are those with the strongest coupling to the Higgs boson. The top quark, being the heaviest fermion in the Standard Model, becomes an important topic for study due to this strong coupling to the Higgs. The top quark was the last of the Standard Model quarks to be observed. It was jointly discovered in 1995 by the D0 and CDF collaborations at Fermilab [12, 13]. In doing so, both experiments needed to leverage some important properties of the top quark.

As the top is the only quark with sufficient rest mass to produce an on-shell $W$, it will undergo a weak decay instead of hadronisation through the strong force like the other quarks. A (charged) weak decay is a flavour changing decay, with transition

probabilities proportional to the corresponding element of the Cabibbo-Kobayashi-Maskawa (CKM) matrix:

$$V_{\text{CKM}} = \begin{pmatrix} V_{ud} & V_{us} & V_{ub} \\ V_{cd} & V_{cs} & V_{cb} \\ V_{td} & V_{ts} & V_{tb} \end{pmatrix}. \tag{2.23}$$

The CKM matrix is almost diagonal, so the generation of quarks undergoing this interaction tends to be preserved. In particular, the matrix element $V_{tb}$ is very close to 1 so the top quark decays almost exclusively to the bottom quark [14]. The decay modes for the top quark then depend only on the subsequent decay of the $W$, which can be either leptonic (to a lepton and neutrino) or hadronic (to two quarks which then hadronise through the strong interaction). This classification of top quark decays allows us to easily identify top quarks from their decay products that are reconstructed in a particle detector - a fact that was used by the experiments at Fermilab, and also in the analysis of Standard Model four-top-quark production that is documented in Chapter 5.

Chapter 3

# The ATLAS Detector

This chapter will provide a brief overview of CERN's Large Hadron Collider (LHC) and the various experiments at the LHC before focussing on the ATLAS experiment. The function of the ATLAS detector will be examined by breaking it down into its major subsystems, and then an explanation of object reconstruction and event simulation in ATLAS will be provided.

## 3.1 CERN and the LHC

CERN, the European Organisation for Nuclear Research, is the world's largest international particle physics laboratory. CERN operates the LHC, a circular proton collider located 100 metres underneath the France-Switzerland border near Geneva. The LHC is responsible for delivering proton-proton collisions to four collision points around the accelerator ring. These collision points are the sites of the major experiments at the LHC. The ATLAS and CMS collaborations use general-purpose detectors to undertake both Standard Model measurements as well as searches for physics beyond the Standard Model. The LHCb collaboration is specialised in $b$-physics measurements while the ALICE collaboration is designed to study heavy-ion collisions.

### 3.1.1 Cross Sections

Experiments are often interested in measuring the cross section of a process. A cross section is a measure of the probability of a particular interaction occurring during the collision of two particles. A cross section given as a function of a final state variable is known as a *differential* cross section, whereas a cross section that has been integrated over all scattering angles (and possibly other variables) is known as a *total* cross section. Cross sections are one of the few physical quantities that can be calculated from the Standard Model, so comparison between theoretical prediction and experimental measurement is one of the primary methods of testing the accuracy of the Standard Model.

### 3.1.2 Delivered Luminosity

The purpose of the LHC is to deliver proton-proton collisions for each experiment to record as data. The first operational period of the LHC is known as Run 1, which spanned 2009 to 2013. Its second operational period, Run 2, spanned 2015 to 2018, and is the dataset that recent physics analyses (such as the one described in Chapter 5) are based on.

The LHC itself is only the last link in a chain of accelerators used to reach the impressive 13 TeV centre-of-mass energy seen in Run 2. Starting from hydrogen gas, electrons are stripped from the gas by means of an electric field to yield protons. These protons are first accelerated to an energy of 50 MeV by LINAC 2, a linear accelerator. The protons are then further accelerated by the Proton Synchrotron Booster (PSB) to 1.4 GeV, the Proton Synchrotron (PS) to 25 GeV, and the Super Proton Synchrotron (SPS) to 450 GeV. At this stage, the protons are finally transferred to the LHC where they are accelerated to their maximum energy of 6.5 TeV in two counter-rotating beams, attaining the total centre-of-mass energy of 13 TeV. The protons within the beams are arranged in discrete packets called *bunches*, which are further grouped into *trains*. This gives rise to the term *bunch crossing*, which refers to the set of collision events that occur when two counter-rotating bunches are allowed to collide.

The rate of collision data delivered by the LHC is quantified by the *instantaneous luminosity*, which has units of $\mathrm{cm}^{-2}\mathrm{s}^{-1}$. The instantaneous luminosity is given by

$$\mathcal{L} = \frac{N_B^2 n_b f_b \gamma_b}{4\pi\sigma_x\sigma_y} F \,, \tag{3.1}$$

where $N_b$ is the number of particles per bunch, $n_b$ is the number of bunches per beam, $f_b$ is the frequency at which bunch crossings occur, $\gamma_b$ is the relativistic gamma factor, $\sigma$ is the (transverse) beam size at the collision point, and $F$ is a geometric factor that accounts for the crossing angle of the beams at the collision point. The LHC was designed to deliver an instantaneous luminosity of $10^{34}\ \mathrm{cm}^{-2}\,\mathrm{s}^{-1}$, which was first achieved in 2016 and exceeded by a factor of 2 in 2018 [15].

The total collision data provided by the LHC is measured using *integrated luminosity*, which as its name suggests is simply the time integral of the instantaneous luminosity:

$$L = \int \mathcal{L}\,\mathrm{d}t \ . \tag{3.2}$$

Given a particular physics process, the expected number of events containing that process can be related to the integrated luminosity by $N = \sigma L$, where $\sigma$ is the cross section of the process. The greater the integrated luminosity recorded by an experiment, the more statistically significant its results can be. Therefore, each experiment strives to record as much of the data as possible that is delivered by the LHC. For instance, the ATLAS collaboration recorded 94% of the delivered luminosity during Run 2 of the LHC (see Fig 3.1), with losses due to detector downtime and data acquisition inefficiencies.

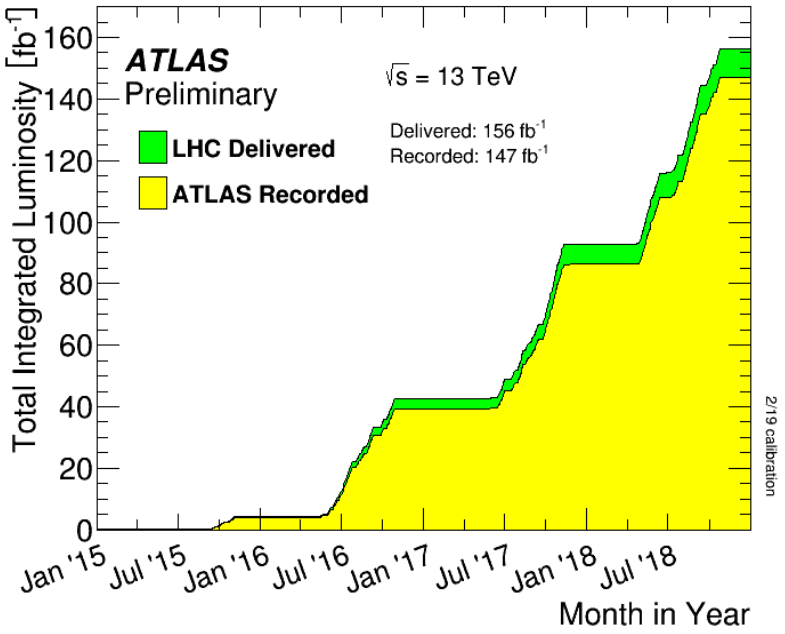


Figure 3.1: Total integrated luminosity at the end of Run 2 of the LHC [16].

### 3.1.3 Pile-up

In order to effectively probe rare, low cross-section processes, the LHC is designed to deliver a high instantaneous luminosity. It does so using a large number of protons per bunch, and a small bunch spacing. However, this leads to multiple simultaneous proton-proton interactions per bunch crossing. This presents a challenge for experiments as it becomes difficult to identify which particles were produced from which interaction. The severity of this issue is quantified by pile-up, which is defined as the average number of interactions per bunch-crossing. Pile-up is typically denoted by the symbol $\mu$.

## 3.2 The ATLAS Detector

The ATLAS detector [17] is a general purpose detector. It has forward-backward symmetry and provides nearly $4\pi$ solid angle coverage over the nominal interaction point. The detector records comprehensive tracking and calorimetry information to allow detailed reconstruction of the proton-proton collisions delivered by the LHC.

The ATLAS coordinate system is a right handed coordinate system which uses the nominal interaction point as its origin. The $x$-axis points towards the centre of the LHC ring, the $y$-axis points upward, and the $z$-axis points along the beamline (in the counter-clockwise direction when viewed from above). The $x-y$ plane is also called the *transverse plane* as it is transverse to the beamline. Given the cylindrical symmetry of the detector, a polar coordinate system is also commonly used. In this system, the azimuthal angle $\phi$ is measured around the beam axis from the $x$-axis.

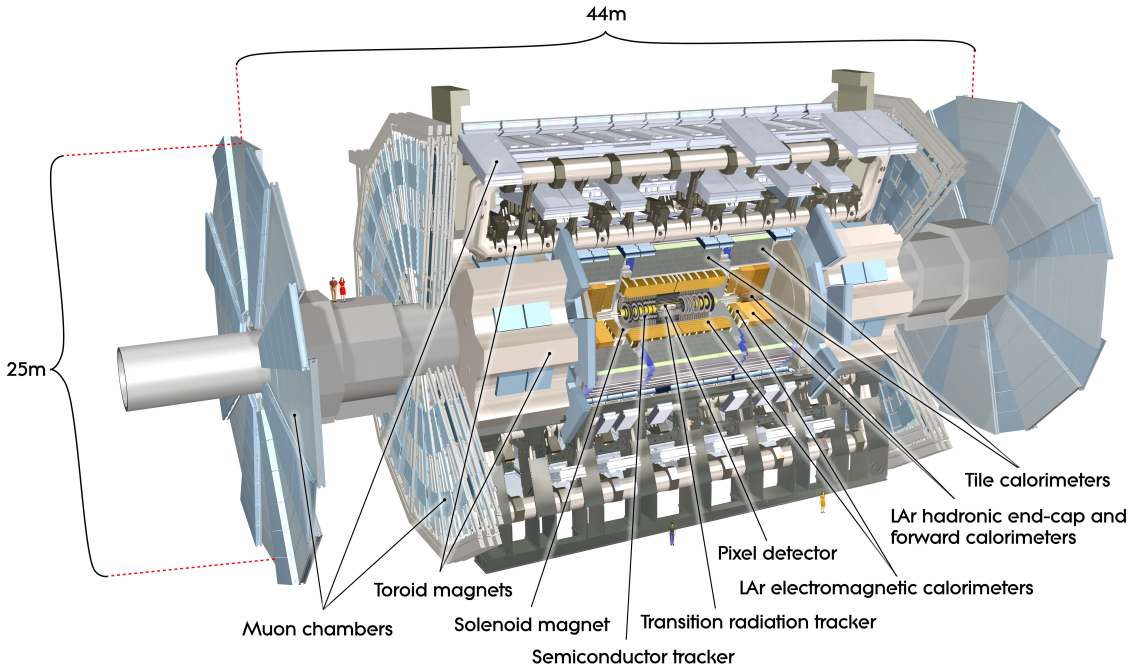


Figure 3.2: Computer generated image of the ATLAS detector [18].

Instead of directly using the angle $\theta$ up from the beamline, the *pseudorapidity*

$$\eta = -\ln \tan \frac{\theta}{2}, \tag{3.3}$$

is used instead.

### 3.2.1 Muon System

The outermost part of the ATLAS detector is the muon system [17]. Since muons have too low an interaction rate to be absorbed by a calorimeter, muon momenta are measured by tracking their deflection in a strong magnetic field. A superconducting toroidal magnet system is used to provide the deflecting magnetic field, while the precision tracking is performed by a series of Monitored Drift Tubes (MDTs). When a charged particle passes through a MDT, it ionises the gas contained in the tube and produces an electric signal. While this can provide spatial resolution on the order of 80 $\mu$m, any ionising radiation is capable of producing a (false) signal in this system, so it is important that all other hadronic and electromagnetic radiation is absorbed before it enters the muon system.

Cathode Strip Chambers (CSCs) are used in addition to the MDTs at larger pseudorapidities ($2.0 < |\eta| < 2.7$). The CSCs use a similar principle to the MDTs, where incident muons ionise the gas contained in the chambers and produce a current. The current flows between anode wires that run the length of a chamber, and a pair of cathode strip planes that sandwich the wires. Each chamber contains four such

wire-plane arrangements. The cathode strips are arranged in a grid formation with strips aligned either parallel to the wire, or orthogonal to the wire. This allows for 2D positional measurement of muons passing through the CSCs at a resolution of 60 $\mu$m in the $\eta$ direction and 5mm in the transverse direction.

Muons are independently triggered in the muon system by the Resistive Plate Chambers (RPCs) in the barrel region and by Thin Gap Chambers (TGCs) in the endcaps. These systems provide a combined coverage for muons within $|\eta| < 2.4$. Both systems are again based on the ionisation of their gas mixtures by incident muons to create a current that can be measured (read out). They were designed specifically to have an extremely rapid response time (on the order of 1 ns and 4 ns for the RPCs and TGCs respectively) in order to provide timely triggering on interesting events containing muon candidates. See Section 3.2.5 for further information about triggering in the ATLAS detector.

### 3.2.2 Calorimetry

The next layer inward contains the calorimetry system [17]. The calorimetry system consists of the electromagnetic calorimeter and the hadronic calorimeter. The calorimeters are designed to absorb as much of the radiation produced in an interaction event as possible, both to allow measurement of the energy of the radiated particles, and to minimise leakage into the muon system. The calorimeters are composed of a barrel which covers the range $|\eta| < 1.475$, and an end-cap which covers $1.375 < |\eta| < 3.2$. The area near the overlap between barrel and end-cap ($1.375 < |\eta| < 1.52$) is called the *crack region*. This region suffers from reduced performance due to the presence of additional equipment required for cooling and readout for the inner detector. Physics analyses that require high precision calorimetry typically exclude the crack region because of this.

### 3.2.3 Tracking

The inner detector is responsible for several key tasks. The most relevant of these tasks to the work that will be presented in Chapter 4 is the reconstruction of paths of charged particles, a process known as *tracking*. The inner detector is also used for reconstructing interaction vertices and identifying electrons.

The inner detector is composed of three major subsystems: the Pixel Detector [19], the Semi-Conductor Tracker (SCT) [20], and the Transition Radiation Tracker (TRT) [21]. The Pixel Detector is the innermost system of the three. It is composed of four silicon pixel layers. The closest of these layers to the beamline is called the Insertable B-Layer (IBL) [22], which was not part of the original design of the detector but rather was added during the technical stop prior to Run 2. The Pixel Detector provides the greatest level of precision of the three systems, which is needed for identifying *displaced vertices* created from particles that travel away from the interaction point before decaying. The SCT is the next closest system to the beamline. It consists of four layers of paired silicon strip detectors in the barrel region

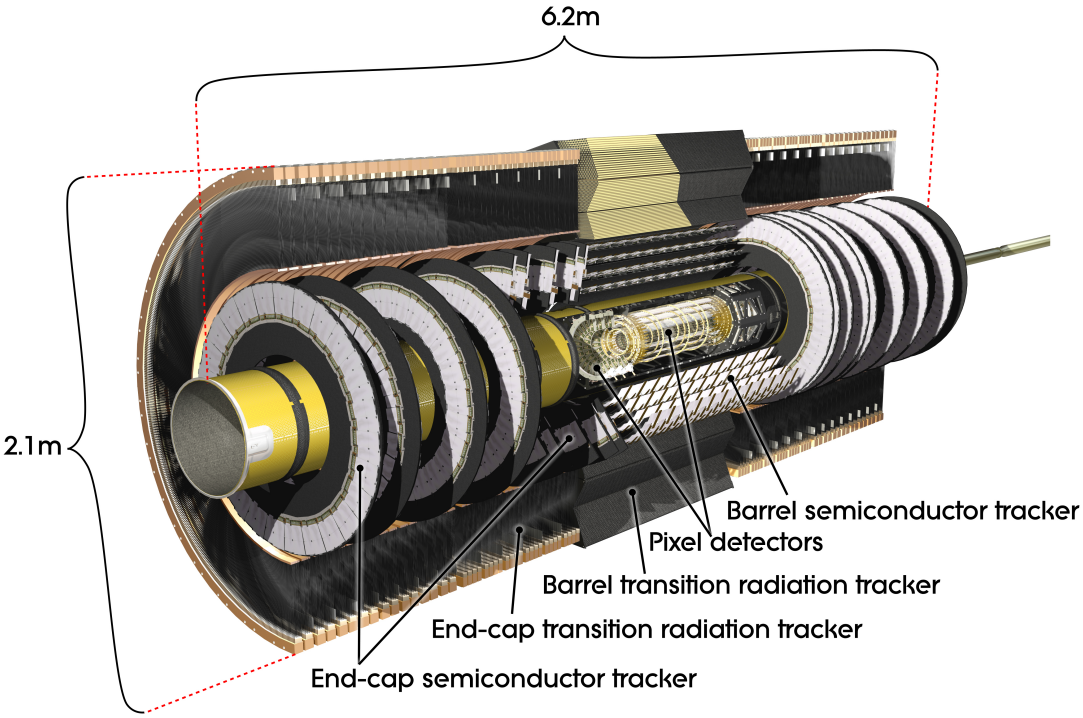


Figure 3.3: Computer generated image of the ATLAS inner detector [23].

and nine disk layers in the end-caps. The strip sensors in each pair are rotated 40 mrad with respect to each other to allow hits to be positioned in both $\phi$ and $z$ space. The strip sensor aligned with the $\phi$ coordinate plane is called the phi-layer, while the rotated sensor is called the stereo-layer. The SCT covers a larger area than the Pixel Detector, albeit at a lower level of precision, which is needed for reconstructing tracks that are perpendicular to the beamline. The outermost subsystem of the inner detector is the TRT. The TRT is composed of 73 layers (160 in the endcaps) of drift tube straws interleaved with transition radiation fibres. The precision afforded by the TRT is lower still than the SCT, but it provides a higher average hit multiplicity per track (36/22 hits for the barrel/end-cap region) and discriminates between heavy and light particles based on the response in the transition radiation fibres. These characteristics are ideal for track curvature measurement and particle identification.

### 3.2.4 Forward Detector

In order to measure the integrated luminosity delivered by the LHC, as well as collision remnants close to the beam pipe, there is a series of four detector systems positioned in the very forward region (*i.e.* at extremely high $\eta$). The first of these detectors is LUCID (LUminosity measurement using Cerenkov Integreting Detector) and the Beam Condition Monitor (BCM), both located within the region enclosed by the main detector [24]. These are the primary luminometers used by the ATLAS collaboration - detectors that are dedicated to measuring the delivered

bunch-by-bunch luminosity. The next detector system is the Zero-Degree Calorimeter (ZDC) [17], located at $z = \pm 140$ m where the beam pipe divides into two separate pipes. This system is intended for detecting forward neutrons produced from heavy-ion collisions. The final and furthest system from the interaction point is ALFA (Absolute Luminosity For ATLAS) [17] at $z = \pm 240$ m from the interaction point. ALFA, as its name suggests, is used for determining the luminosity delivered to ATLAS through measuring the cross section of particles that have been elastically scattered through extremely low angles.

### 3.2.5 Trigger and DAQ

The method by which events are selected to be recorded for further study is known as *triggering*. With the LHC delivering bunch crossings between billions of protons every 25 ns, many more interactions take place within the ATLAS detector than can be read out and recorded. This necessitates the use of fast and efficient triggers in order to retain the most interesting and useful events. The ATLAS experiment uses a two-level trigger system [25]. The first trigger level (L1) is hardware based. It simply selects events based on calorimetry and muon information to reduce the event rate to a maximum of 100 kHz. The second trigger level, known as the High Level Trigger (HLT), is software based. It uses tracking information derived from the ATLAS Inner Detector to determine whether a given L1-accepted event is interesting, further reducing the event rate to approximately 1 kHz.

The data acquisition system (DAQ) [26] handles the readout and storage of events that have passed the triggers. Selected events are transferred from local memory to permanent storage at the CERN computer centres. Outgoing events are assigned to one of several possible data streams based on which analyses are likely to make use of them.

## 3.3 Object Reconstruction and Definition

Physics analyses performed by ATLAS do not work directly with the raw information extracted from the detector, such as hits in the inner detector or energy deposits in the calorimeters. Instead, this information is used to reconstruct the particles that were produced in each interaction. Using these reconstructed physics objects is vital to be able to apply our physical intuition to help determine whether the observed data is consistent with the Standard Model.

### 3.3.1 Tracks and Vertices

A *track* encompasses the momentum and trajectory of a charged particle as it passes through the inner detector. The majority of tracks are reconstructed using an *inside-out* pattern recognition algorithm [28, 29]. Groups of three hits in the pixel and SCT layers of the inner detector are used to form track seeds, then candidate tracks are

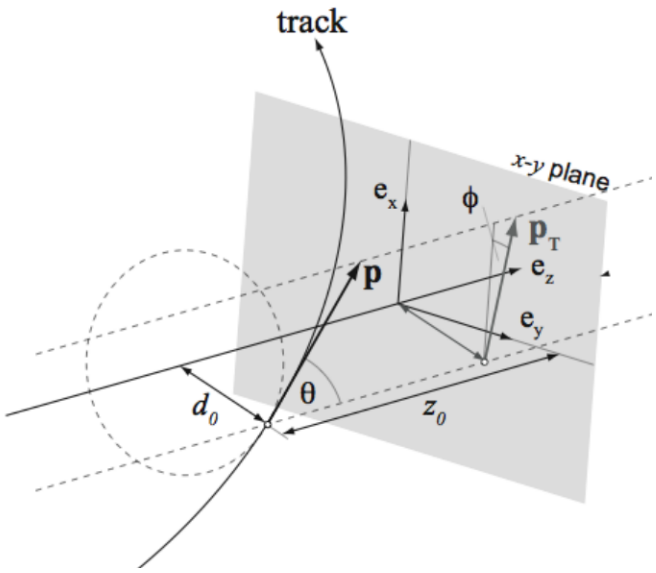


Figure 3.4: Visualisation of the parameters used to describe reconstructed tracks [27]. For reference, the Cartesian ATLAS coordinate system $(e_x, e_y, e_z)$ is also shown.

generated using additional hits in these layers that follow the initial trajectory of the seed. The tracks are then extended into the TRT by including hits in the TRT layers. Poor track candidates, such as those with poorly aligned hits or missing hits altogether in some layers, are filtered out using an ambiguity solver. Each track object that results from this algorithm is a collection of hits that represents the path of a single charged particle as it passes through the inner detector.

A *vertex* is a collection of tracks originating from the same proton-proton collision. Tracks passing certain quality requirements are passed to the vertex reconstruction algorithm. The reconstruction algorithm determines the best vertex position for these tracks and removes any tracks that are incompatible with this vertex. Rejected tracks are then passed back into the same algorithm until either all tracks have been associated with a vertex or no further valid vertices can be constructed. In events with multiple reconstructed vertices, the vertex with the greatest sum of $p_{\mathrm{T}}$ from associated tracks is designated the primary vertex (also called hard scatter vertex). Secondary vertices are typically considered to be from subsequent decays of unstable particles produced in the hard scatter event, while pile-up vertices are from less energetic interactions that occur simultaneously with the hard scatter.

Tracks are fitted with a helical trajectory, which is parametrised with the following five variables:

- $d_0$, the transverse distance from the beamline to the track's point of closest approach,
- $z_0$, the distance along the $z$-axis between the interaction point and the track's point of closest approach,
- $\eta$, the pseudorapidity,

- $\phi$, the azimuthal angle, and

- $q/p_{\mathrm{T}}$, the ratio between the track's charge and transverse momentum.

### 3.3.2 Electrons and Photons

Reconstruction for electrons and photons starts with identifying clusters of energy deposits in the EM calorimeter. The clustering is done by a *sliding-window* algorithm [30, 31], which positions rectangular $\eta - \phi$ windows such that the total energy deposited in the calorimeter elements within each window is (locally) maximised. The energy clusters are then matched with tracks from the inner detector by extrapolating the trajectory of the tracks to the calorimeter layers. An energy deposit and track is considered to be matched if their absolute $\eta$ and $\phi$ separation is less than 0.05 and 0.1 respectively. Energy clusters that are not matched to any tracks are labelled as photon candidates, while clusters with at least one matched track are labelled as electron candidates. The kinematics and charge of a candidate electron is determined from its primary track, which is the matched track that is closest to the centre of its cluster, with preference to tracks with hits in the pixel or SCT layers.

The next stage of processing after reconstruction is identification [31]. There are multiple background processes that can produce similar detector signals to a true photon or electron from the original proton-proton interaction. Identification algorithms are used to provide background rejection on reconstructed particle candidates to improve the purity of true particles. Likelihood profiles are created for various parameters from the reconstruction stage (e.g. number of SCT hits) and are convolved to produce three working points for photon and electron identification: *loose*, *medium* and *tight*. These working points offer progressively improved background rejection at the cost of reduced efficiency after identification by using stricter quality requirements to the reconstructed objects.

Electrons or photons produced from background processes such as photon conversion into electron-positron pairs, misidentification of hadrons as leptons or photons, and semileptonic decays of heavy quarks represent a significant background of "fake" electron or photon candidates that can be difficult to distinguish from true candidates. However, these fakes do tend to feature reduced activity in both the inner detector and calorimeter compared to particles from the hard scatter. Isolation algorithms [31] leverage this signature by quantifying detector activity in the vicinity of an electron or photon candidate. Different physics analyses will favour either signal efficiency or background rejection, and to varying extents. To accommodate for this, a large range of isolation working points are available. The efficiency of each working point varies based on the particular signal process of interest, so it is left to the analysis team to determine the optimal working point for their use case.

### 3.3.3 Muons

Muon reconstruction [32] makes use of data from the inner detector, the muon spectrometer, and any calorimetry deposits that are compatible with minimally ionising particles. This results in four classes of reconstructed muons based on which detector systems contributed to the reconstruction. *Combined* (CB) muons have independently reconstructed tracks in both the inner detector and the muon spectrometer which have been combined with a global fit. *Segment-tagged* (ST) muons have a reconstructed track in the inner detector that crosses only one layer of the muon spectrometer. *Calorimeter-tagged* (CT) muons have a reconstructed inner detector track and an associated calorimeter deposit. *Extrapolated* (ME) muons only have a reconstructed track from the muon spectrometer that is extrapolated to the primary vertex.

Similarly to electron and photon candidates, reconstructed muon candidates are passed through an identification algorithm [32] to reject similar backgrounds. Alongside the loose, medium and tight working points that were also offered for photons and electrons, muons additionally have a *high-pt* working point.

Muons also suffer from "fake" candidates originating from semileptonic decays, so isolation algorithms [32] based on detector activity are also used to provide further background rejection. A range of isolation working points for muons are available, optimised for different types of physics analyses.

### 3.3.4 Jets and *b*-jets

The individual quarks and gluons ejected from a proton-proton collision will almost instantaneously hadronise due to colour confinement. This results in a collimated spray of hadrons known as a jet. Jet reconstruction [33] makes use of two stages of clustering of energy deposits from the calorimeter. The first clustering stage creates *topo-clusters*. First calorimeter cells with a signal-to-noise ratio greater than four are used as cluster seeds. Calorimeter cells that have a signal-to-noise ratio greater than two and are neighbouring a seed or any of its associated cells are grouped with the seed to form a topo-cluster. These topo-clusters can be thought of as representing the energy deposits of individual hadrons from a jet. The second clustering stage then groups the various hadrons from a particular jet. The anti-$k_T$ algorithm [34] is used to perform the grouping of topo-clusters into jets. The algorithm prioritises grouping soft clusters with the nearest hard cluster, which leads to perfectly conical jets when the hard clusters are sufficiently separated.

The identity of the original parton from a proton-proton collision that produced a jet can be an important piece of information for physics analyses. The process of determining that underlying parton is known as *tagging*. The most common form of tagging is identifying jets produced from $b$ quarks, which is referred to as $b$-tagging. $b$-tagging methods [35] make use of the relatively long lifetime of $b$-hadrons to discriminate $b$-jets from other types of jets. The long lifetime leads to features such as displaced vertices (with respect to the beamline) and altered jet shape, which

are typically leveraged by a Boosted Decision Tree (BDT). See Section 5.8 for a general description of BDTs. The BDT score is used to define working points for b-tagged jets. In ATLAS $b$-tagging is performed by the MV2c10 algorithm [36] and the $b$-tagging score from this algorithm can either be used directly, or cut on, to determine whether a given jet originated from a $b$-quark.

### 3.3.5 Taus

Taus decay quickly after production, so reconstruction must be performed on their decay products. If a tau decays leptonically, i.e. to a neutrino and either an electron or muon, it is indistinguishable from the lighter lepton and will be reconstructed as such since neutrinos are not visible to the detector. Taus that decay hadronically, i.e. to a jet, can be separated from other types of jets as their energy is constrained by the tau mass, and exhibit other kinematic differences. A Boosted Decision Tree (BDT) trained on tracking and calorimetry information is used to perform this separation [37]. As with the other reconstructed particles, identification for taus offer the standard loose, medium and tight working points.

### 3.3.6 Missing Transverse Energy

Missing Transverse Energy [17], also referred to as MET or $E_T^{\text{miss}}$, is used as a proxy to determine the total energy of any invisible particles such as neutrinos in an event. Just prior to a collision event, the two colliding protons have no momentum in the plane transverse to the beam. By conservation of momentum, the vector sum of particle momenta in the transverse plane after the collision must also be zero. After reconstructing all visible particles in an event, the MET is assigned as the negative vector sum of those particles' transverse momenta and any remaining energy deposits not associated with a reconstructed object. The net momenta of all invisible particles produced in the event must equal the MET in order to satisfy momentum conservation.

## 3.4 Simulation

There are two stages of simulation that are used to generate predictions from the Standard Model. The first stage is the simulation of the proton-proton collision, which must accurately represent all possible interactions allowed by the Standard Model. The second stage is simulating the detector response and reconstruction of an event, which is required to be able to compare simulated events to recorded data in a meaningful fashion.

### 3.4.1 Event Simulation

The process for generating a simulated proton-proton collision takes several steps. First a parton from each proton is chosen to undergo the hard scattering interaction.

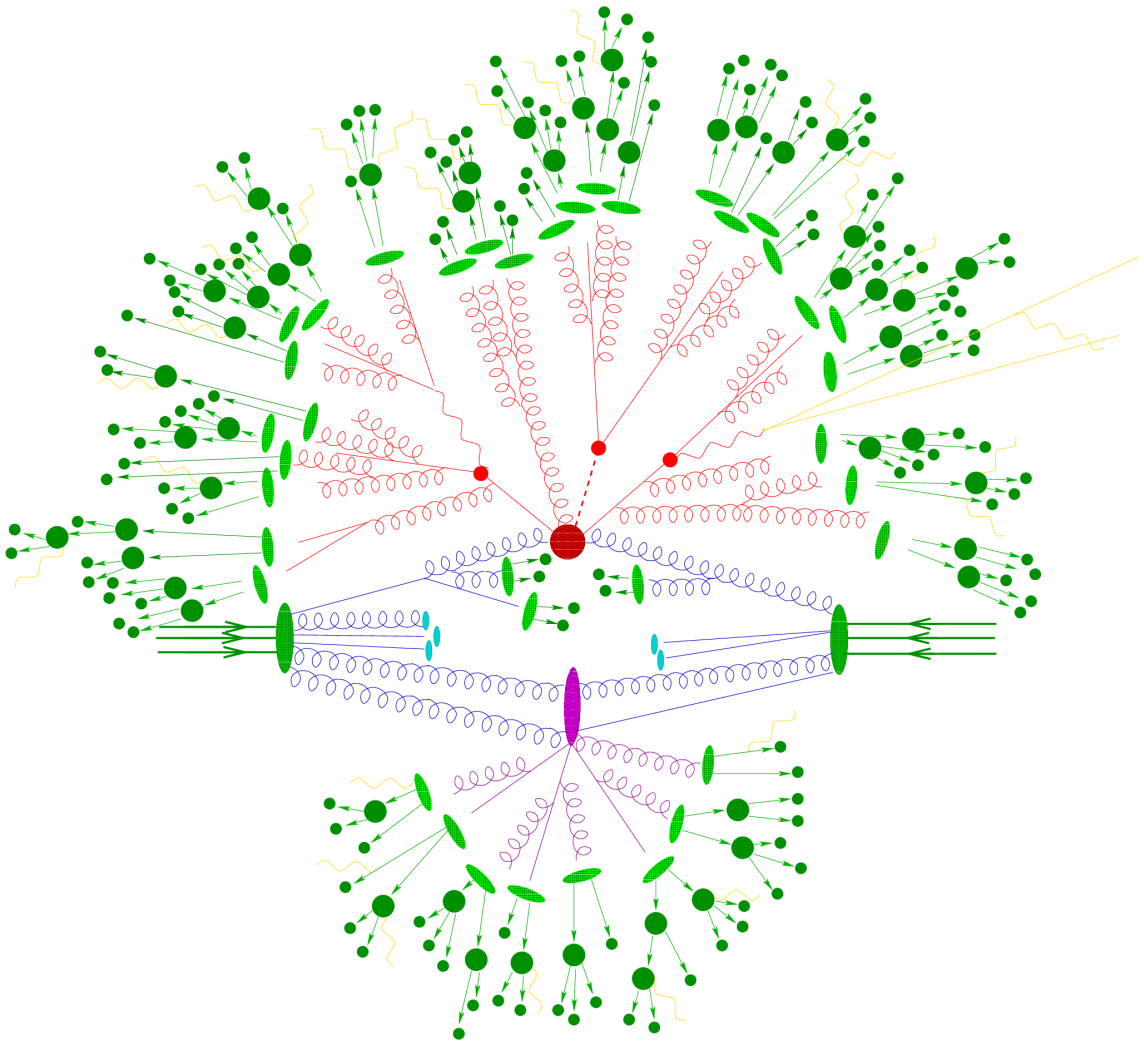

Figure 3.5: Visualisation of a simulated proton-proton collision [38]. The initial protons are represented by the green ellipses near the centre of the image, and their partons by the blue lines leading out from them. The large red circle represents the hard scatter interaction and the rest of the red network represents the resulting parton shower. The purple ellipse and network represents a secondary interaction and its own parton shower. Hadronisation and subsequent decays to stable states are represented by the light and dark green objects at the periphery of the image. The straight yellow lines produced at the right side of the image represent leptons and/or neutrinos, while the wavy yellow lines represent soft photon radiation.

The protons are modelled as bags of partons based on the proton's Parton Distribution Function (PDF), and the possible parton interactions are determined by Standard Model matrix elements. Any unstable particles, e.g. $W$ and $Z$ bosons, that are produced at this stage are also allowed to decay as part of the hard scattering simulation. Next the parton showering is simulated. Parton showering refers to the QCD radiation emitted by any of the partons at any point during the collision event. A specialised algorithm is used to handle the production of jets, as parton showering algorithms tend to be based on small-angle and low-energy approximations. The process so far can be repeated for other parton pairs to generate events with multi-parton interactions. After parton showering, a hadronisation algorithm is applied to reduce all partons to hadronic states. Some of these hadrons also may be unstable and decay further. Hadrons with a decay length less than 10 mm will have their decay simulated by the event generator. Tau leptons with a decay length of 87 $\mu$m are also decayed by the generator. Finally, the effects of electromagnetic radiation is simulated during the hadronic and tau decays. Further details regarding the simulation software and datasets used for event simulation are given in Section 5.3.

### 3.4.2 Detector Simulation

The final state information produced by the event generator is suitable for computing theoretical quantities such as cross section predictions, but not for comparison with experimental data. In order to make the simulated events compatible with data, the detector response to the final state particles must also be simulated. The full simulation process uses a GEANT4 [39] model of the ATLAS detector to accurately reproduce the energy deposits and inner detector hits for each particle in the event. The electronic readout from the detector response is also reproduced, so that simulated events have the same format as recorded data events. This allows simulated events to be processed with the same reconstruction algorithms that were discussed in Section 3.3, resulting in an output that can be directly compared with data.

The full simulation using GEANT4 is very time-consuming to run. To save on the computational resources required to generate a sample of simulated events, a faster simulation of the detector can be used. The ATLAS FAST-II (AF2) [40] simulation software is a factor of ten faster than GEANT4 simulation, however it vastly simplifies the calorimeter response as a compromise. As a consequence, details such as jet sub-structure are lost. For analyses that do not need this additional detail, the use of AF2 allows the production of higher statistics samples without increasing the required computational budget.

Chapter 4

# The Fast Tracker

In order to extend the LHC's ability to probe rarer processes in the Standard Model, an upgrade project known as the High-Luminosity LHC (HL-LHC) is being undertaken. This upgrade is expected to at least double the peak instantaneous luminosity of the LHC (see Figure 4.1). With the increased pile-up expected with the HL-LHC upgrade, comprehensive tracking becomes too expensive for the current HLT to perform with its available computational resources [41]. This is further exacerbated as the reconstruction time per track increases exponentially with detector occupancy (see Figure 4.2). The Fast TracKer system (FTK) was commissioned to alleviate this problem by providing tracking information directly to the HLT instead. The FTK would be provided with an identical copy of the pixel and SCT read-outs following a L1-triggered event. It would make use of the hit data from the 12 logical layers in the inner detector to reconstruct and output all tracks with $p_T > 1$ GeV and their corresponding helix parameters [42].

The need for fast tracking was already known prior to the start of Run 2. Even with the trigger upgrades that were performed during the first long shutdown (LS1) of the LHC, software based tracking was only available to a fraction of the level-1 triggers that were in use at the time. The inclusion of the FTK would provide tracking information to all level-1 triggers, which in particular is highly beneficial for $b$- or $c$-jet identification. The FTK was scheduled to have coverage of the detector barrel by early 2016, and full volume coverage 6 months later in time for Run 2 data taking. Due to various delays, the FTK project remained in development through to 2019, during which it was succeeded by the Hardware Track Trigger (HTT) upgrade project [43].

## 4.1 Hardware Design

The FTK was designed as a highly parallel hardware system to enable it to produce comprehensive tracking information in the timeframe required for HLT event selection, and under the high pile-up conditions expected with HL-LHC. The detector volume is divided into 64 overlapping $\eta - \phi$ sectors (16 $\eta$ bins by 4 $\phi$ bins), each of which is assigned to an FTK tower. An FTK tower is responsible for performing track reconstruction and fitting on the inner detector hits within its assigned sub-region.

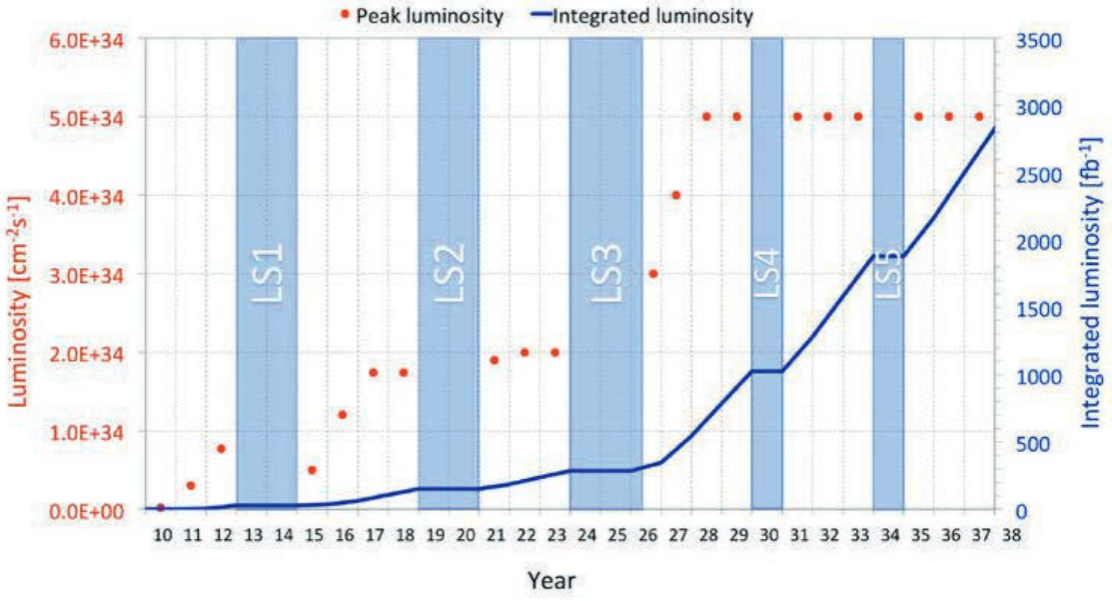


Figure 4.1: Forecast for peak luminosity (red dots) and integrated luminosity (blue line) into the HL-LHC era, assuming nominal HL-LHC parameters [44].

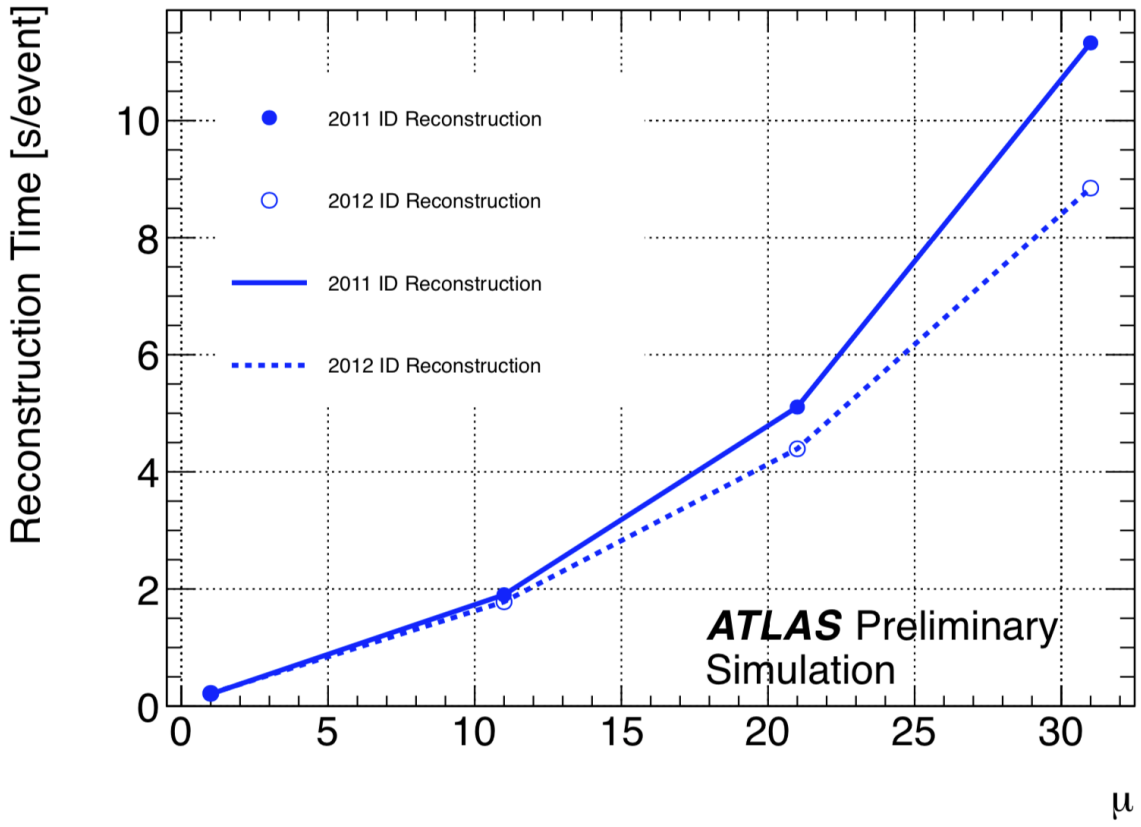


Figure 4.2: The CPU reconstruction time for all tracks in an event as a function of the pile-up [45].

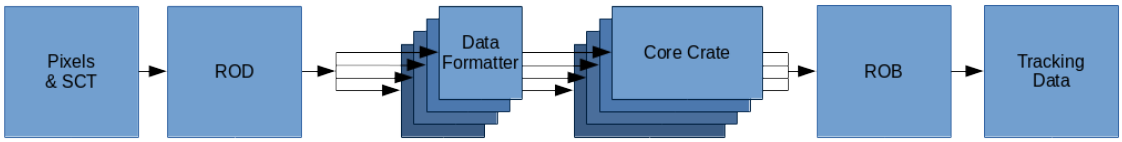


Figure 4.3: Diagram showing the flow of data from the inner detector through the FTK. The ROD is the silicon Read Out Driver; it is responsible for reading hit information from the inner detector upon a level-1 trigger. The hits are distributed to their corresponding $\eta - \phi$ tower by the Data Formatters. The $\eta - \phi$ towers are grouped into sets of 8 towers per core crate. The ROB is the ATLAS Read Out Buffer; it collates tracking information from the FTK for transmission to the HLT.

The overlap is intended to counteract the difficulty in reconstructing tracks near or at the boundaries between towers.

The major innovative development of the FTK is the Associative Memory (AM) system used for track reconstruction [46–48]. The Associative Memory system is based on application specific integrated circuits (ASICs) that store patterns of hits in the silicon layers that correspond to real particle tracks. These patterns are determined in advance based on full simulation of the ATLAS detector's response to single particles. The AM is designed with a massively parallel architecture such that each stored pattern receives the silicon hit information almost simultaneously, so that the pattern matching process completes soon after the last hit has been received from the detector readout system. See Figure 4.3 for a visualisation of the flow of data through the FTK.

## 4.2 Track Reconstruction and Fitting

A two-stage process is used to perform the track reconstruction and fitting. The first stage uses 8 of the 12 silicon layers from the inner detector: pixel layers 1 through to 3, both phi and stereo sides of SCT layer 0, and the phi sides of SCT layers 1 through to 3. A coarse resolution view of this hit data is passed to the Associative Memory system for identification of track candidates. Track parameters are calculated from full resolution data for track candidates that have hits in all 8 layers, or all except one layer. Instead of performing a helical fit to obtain these parameters, a series of linear calculations are used as a fast approximation. This approximation uses the scalar product between hit coordinates and a set of pre-calculated constants to estimate the track parameters and $\chi^2$ components. This method produces accurate estimates when the region of validity for a given set of constants is small. Regions the size of a single silicon module from the inner detector were found to be sufficient for this purpose. Finally, duplicate track candidates are removed and a basic quality cut is applied. Track candidates which use fewer than 6 different hits are considered duplicates, and the candidate with the best $\chi^2$ estimate and most logical layers with hits is retained. Tracks with $\chi^2 < 6$ pass on to the second stage, and tracks with

hits in all layers that are close to the $\chi^2$ cut boundary are refit with one fewer layer included in its reconstruction. This allows for tracks with true hits in seven layers and one falsely associated hit in the last layer.

In the second stage, the candidate tracks are extrapolated to the remaining 4 silicon layers: pixel layer 0 (also known as the IBL), and the stereo sides of SCT layers 1 through to 3. Hits near an extrapolated track are included in the track's definition. Then each track is refit using its hits in all silicon layers. Tracks which are missing hits in more than two layers or hits in both a pixel and SCT layer are discarded. A tighter $\chi^2 < 4$ cut is applied and duplicate track removal is performed again. All remaining tracks are now considered to have passed second stage tracking. The track parameters and associated hits for second stage tracks with $p_T > 1$ GeV are then passed on to the HLT for event selection.

## 4.3 Simulation

Simulation of the FTK is vital for both development purposes and for physics analyses that make use of the improved tracking from the FTK. For development, it is important to be able to test and optimise the algorithms used in the FTK. Having an accurate simulation will enable rapid prototyping to ensure optimal use of the system. For physics analyses, it is always important to understand what the expected detector response to Standard Model processes will be, as discussed in greater detail in Section 3.4.

The current simulation code for the FTK is integrated into Athena [49], the ATLAS software framework. The simulation does *not* emulate every detail of the FTK, such as data transmission protocols between the various hardware components, but these differences were deemed to have no measurable impact on the tracking output [42].

## 4.4 Fast Simulation

As the FTK is part of the planned trigger upgrade for the ATLAS detector, the simulation of the FTK will eventually need to be integrated into the overall detector simulation workflow discussed in Section 3.4.2. To provide compatibility with the current detector simulation software suite, a fast simulation of the FTK will also need to be developed. The simulation should take truth-level tracks as input, and output the FTK tracks that would result from them being processed by the FTK.

The core idea for implementing a fast simulation of the FTK is to parametrise the response of the FTK based on the position of a track within the detector. This is a similar idea to the method for quickly estimating fits for candidate tracks as described in Section 4.2. Two aspects of the FTK response are parametrised: the efficiency, and the fitted track parameters. Instead of simulating the performance of the FTK hardware, these parametrisations are used alongside a random number stream to reproduce the same distributions as the full simulation. This means that

| Bin index | 0 | 1 | 2 | 3 |
|---|---|---|---|---|
| $\lvert q/p_T \rvert$ | 0-0.4 | 0.4-0.8 | 0.8-1.0 | |
| $\lvert \eta \rvert$ | 0-0.5 | 0.5-1.5 | 1.5-2.0 | 2.0-2.5 |
| $\lvert d0 \rvert$ | 0-1.2 | 1.2-1.6 | 1.6-2.0 | |
| $\lvert z0 \rvert$ | 0-72 | 72-96 | 96-120 | |

Table 4.1: Binning scheme of helix parameters for the efficiency map. Each combination of bins represents one sub-region used in the efficiency map.

| Bin index | 0 | 1 | 2 | 3 | 4 | 5 | 6 | 7 | 8 | 9 | 10 | 11 |
|---|---|---|---|---|---|---|---|---|---|---|---|---|
| $\lvert q/p_T \rvert$ | 0-0.2 | 0.2-0.3 | 0.3-0.4 | 0.4-0.5 | 0.5-0.6 | 0.6-0.7 | 0.7-0.8 | 0.8-0.9 | 0.9-1.0 | | | |
| $\lvert \eta \rvert$ | 0-0.3 | 0.3-0.5 | 0.5-0.7 | 0.7-0.9 | 0.9-1.1 | 1.1-1.3 | 1.3-1.5 | 1.5-1.7 | 1.7-1.9 | 1.9-2.1 | 2.1-2.3 | 2.3-2.5 |

Table 4.2: Binning scheme of helix parameters for the smearing map. Each pair of $q/p_T$ and $\eta$ bins represents one sub-region used in the smearing map.

while the simulated response for any given track may not agree between fast and full simulation, the distribution of a statistically significant sample of such simulated responses will agree.

### 4.4.1 The Efficiency and Smearing Maps

The parametrisation of the overall FTK efficiency is called the efficiency map. The intent of the efficiency map is to account for variations in reconstruction efficiency across different regions of track phase space. It assumes azimuthal symmetry, but discriminates by the remaining 4 track parameters: $q/p_T$, $\eta$, $d0$ and $z0$. The 4-dimensional phase space spanned by these parameters is divided into 3 $q/p_T$ bins by 4 $\eta$ bins by 3 $d0$ bins by 3 $z0$ bins to form a total of 108 sub-regions (see Table 4.1 for further details). Each of these regions is assigned a floating point value between 0 and 1, which represents the fraction of successfully reconstructed tracks from the hits of all tracks that were passed to it (which is known at truth-level).

The parametrisation for FTK track fitting is called the smearing map. The smearing map models the distribution of errors between the fitted track parameters from the FTK and the true track parameters which are known from simulation. Unlike the efficiency map, the smearing map only discriminates on the $q/p_T$ and $\eta$ track parameters, divided into 9 $q/p_T$ bins by 12 $\eta$ bins (see Table 4.2). With this finer binning scheme, the smearing map also uses a total of 108 sub-regions. Each sub-region is assigned a set of 5 double gaussian distributions - one for each track parameter. These distributions were found to provide the most accurate modelling of the errors in FTK track parameters. The double gaussian distributions used in the smearing map are characterised by 4 parameters: $\sigma_{\text{narrow}}$, the standard deviation of the core gaussian; $\sigma_{\text{wide}}$, the standard deviation of the tail gaussian; $\mu$, the mean for both gaussians; and $f$, the ratio of integrals of the tail gaussian to the core gaussian.

### 4.4.2 The Smearing Algorithm

The smearing algorithm takes a truth-level track as input and produces an FTK reconstructed track as output. First, the algorithm determines the efficiency map bin indices (and hence sub-region) from the input track's helix parameters. If the track has parameters outside the mapped range, it is discarded. Next the efficiency mapping is applied. This is done by generating a random number from a uniform random distribution in the interval $[0, 1)$ and comparing it to the efficiency value mapped to the track's sub-region. If the random number is greater than the efficiency value, the track is discarded. Otherwise, the algorithm proceeds to apply the smearing map to the track.

In a similar process as before, the bin indices and sub-region for the smearing map is determined, discarding the track if it lies outside the parametrised region. Then it will generate an offset for each of the 5 track parameters. It does this by sampling from each of the double gaussian distributions contained in the smearing map: first generate a uniform random number in the range $[0, 1)$ and compare it with the $f$ ratio to determine whether to use the core or tail gaussian; then generate a random number from that gaussian to use as the offset. The output track can then be created, where each of its helicity parameters are given by the sum of the original parameter and the offset that was generated from the smearing map. These gaussian offsets can be interpreted as a "smearing" of the true track parameters to emulate FTK reconstruction, which gave rise to the name of the algorithm.

The track object that is created requires some additional properties as part of its construction. These remaining properties are technical objects that are either copied from the input track object or derived from the smeared track parameters. During this process, the first and second stage FTK track selections are emulated. Recall from Section 4.2 that first stage tracks require hits in at least 7 of the 8 first stage layers, and second stage tracks require hits in at least 3 of the 4 remaining layers. Due to ambiguities in the mapping between the logical layers (that are accessible in the simulation software framework) and the physical layers of the inner detector, a slightly altered version of this selection criteria was implemented instead. In this version, the stereo side of SCT layer 0 is considered a second stage layer and the hit counts are adjusted accordingly: at least 6 of the remaining 7 first stage layers must have hits, and similarly at least 4 of the 5 second stage layers must have hits. At the end of this process, an FTK reconstructed track is produced.

### 4.4.3 Validation

A vital part of the implementation of the smearing algorithm, as for any software development project, is the testing and validation of the produced code. This helps to identify errors and mistakes that the compiler will not detect. The method used to validate the smearing algorithm was to produce histograms of the smeared track parameters and compare them to the track parameters from the full FTK simulation. If the algorithm was implemented correctly, the histograms of the fast-

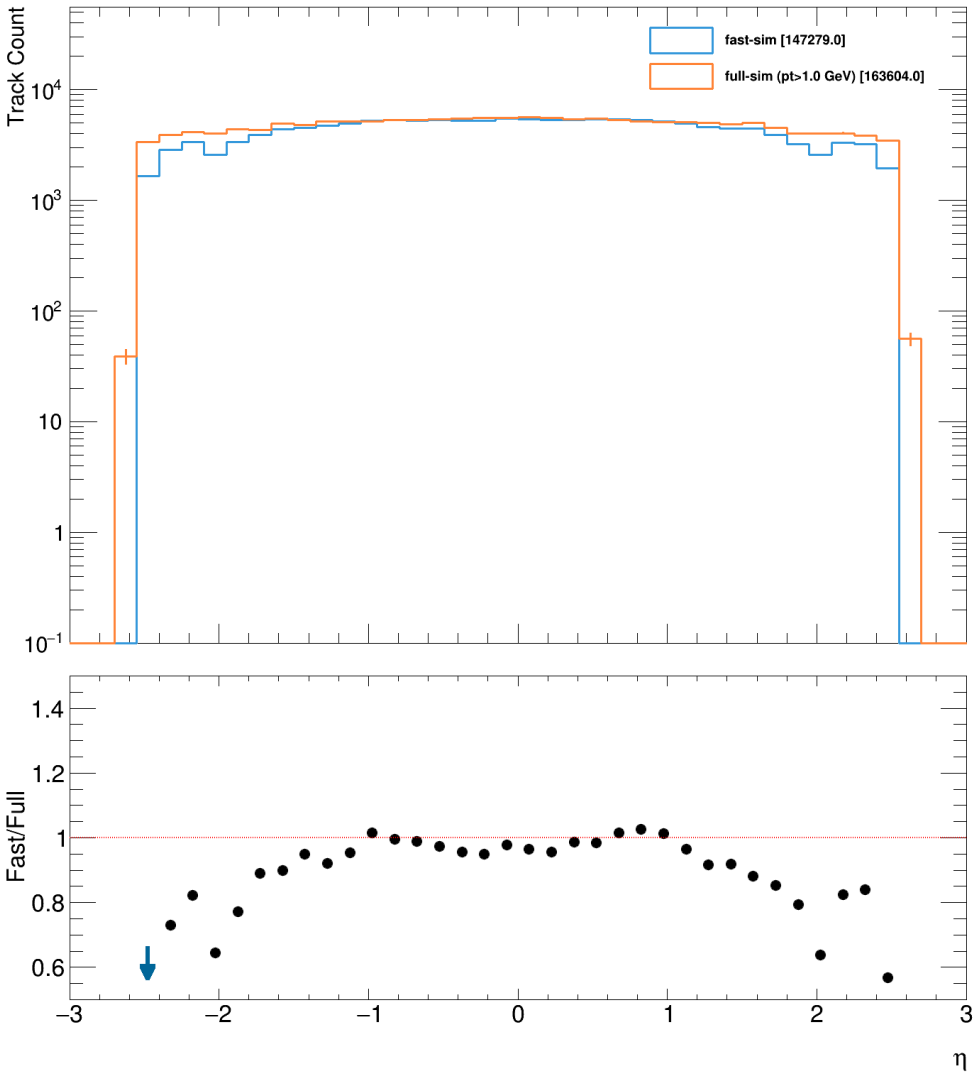


Figure 4.4: A histogram comparing the distribution of the $\eta$ track parameter for FTK tracks generated from full- and fast-simulation for a sample of $t\bar{t}$ events. The bracketed values are the total number of tracks present in the depicted region.

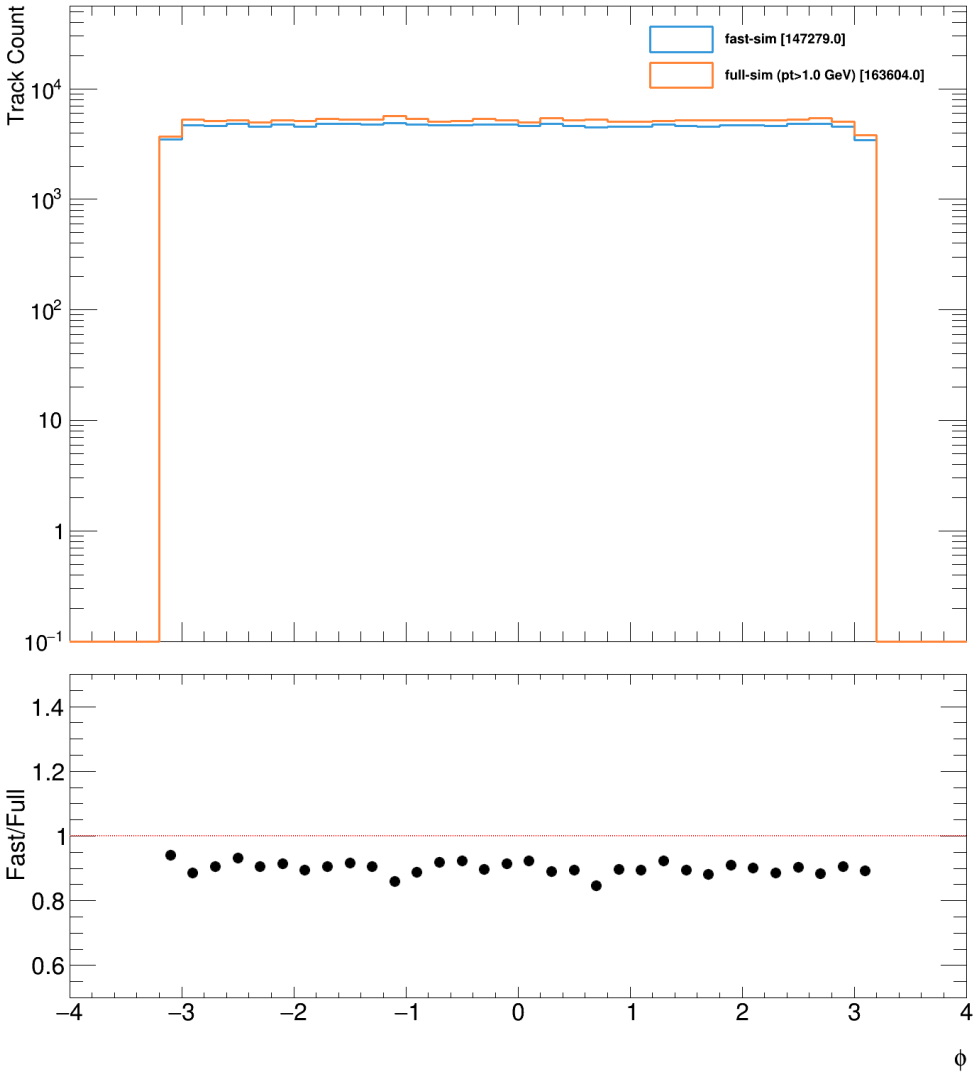


Figure 4.5: A histogram comparing the distribution of the $\phi$ track parameter (measured in radians) for FTK tracks generated from full- and fast-simulation for a sample of $t\bar{t}$ events. The bracketed values are the total number of tracks present in the depicted region.

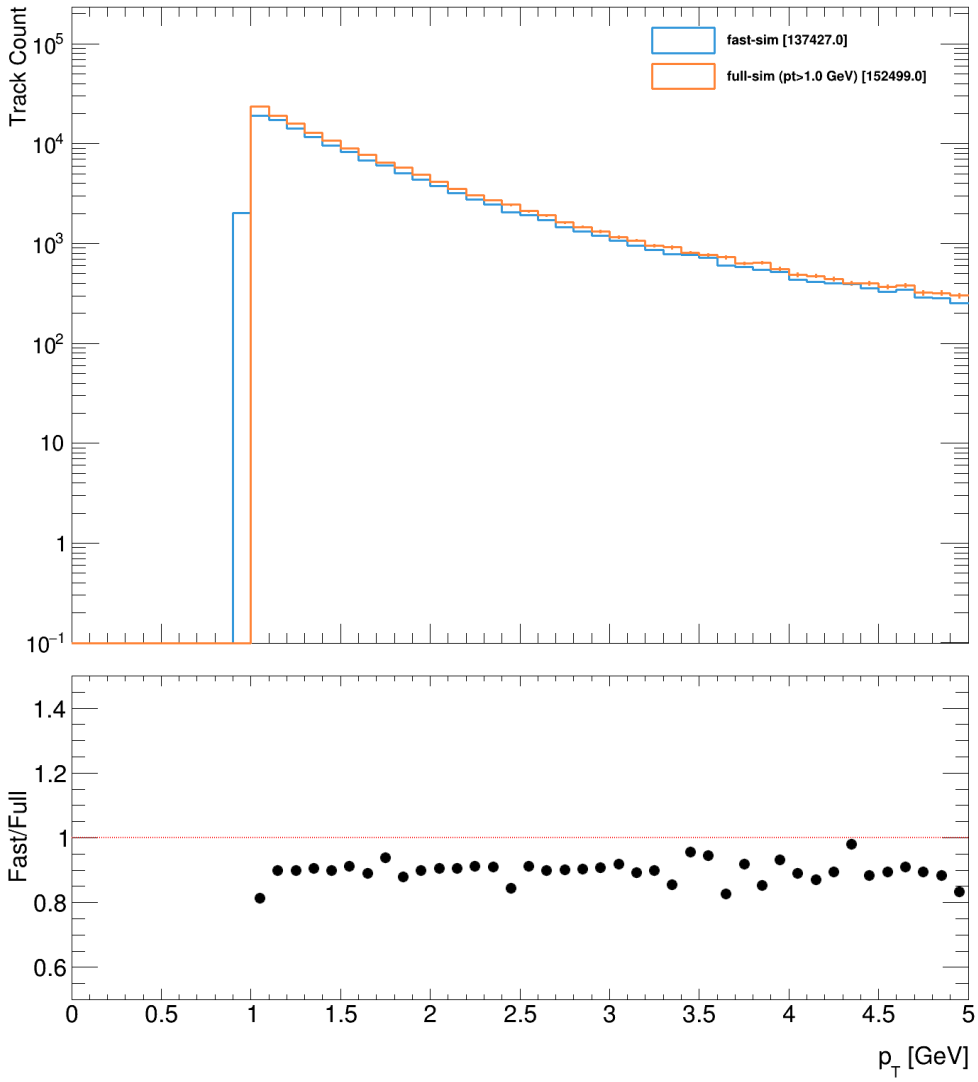


Figure 4.6: A histogram comparing the distribution of the $p_T$ track parameter for FTK tracks generated from full- and fast-simulation for a sample of $t\bar{t}$ events. The bracketed values are the total number of tracks present in the depicted region.

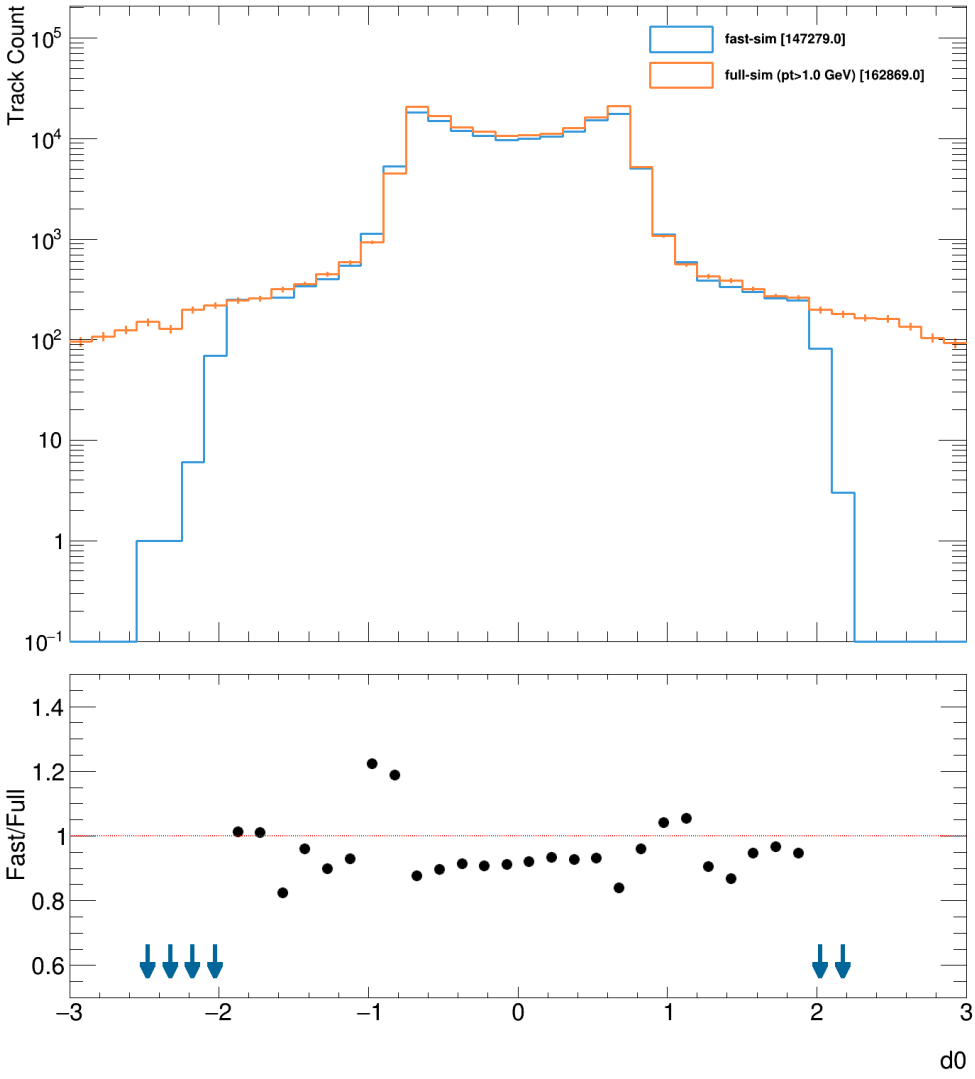


Figure 4.7: A histogram comparing the distribution of the $d0$ track parameter (measured in mm) for FTK tracks generated from full- and fast-simulation for a sample of $t\bar{t}$ events. The bracketed values are the total number of tracks present in the depicted region.

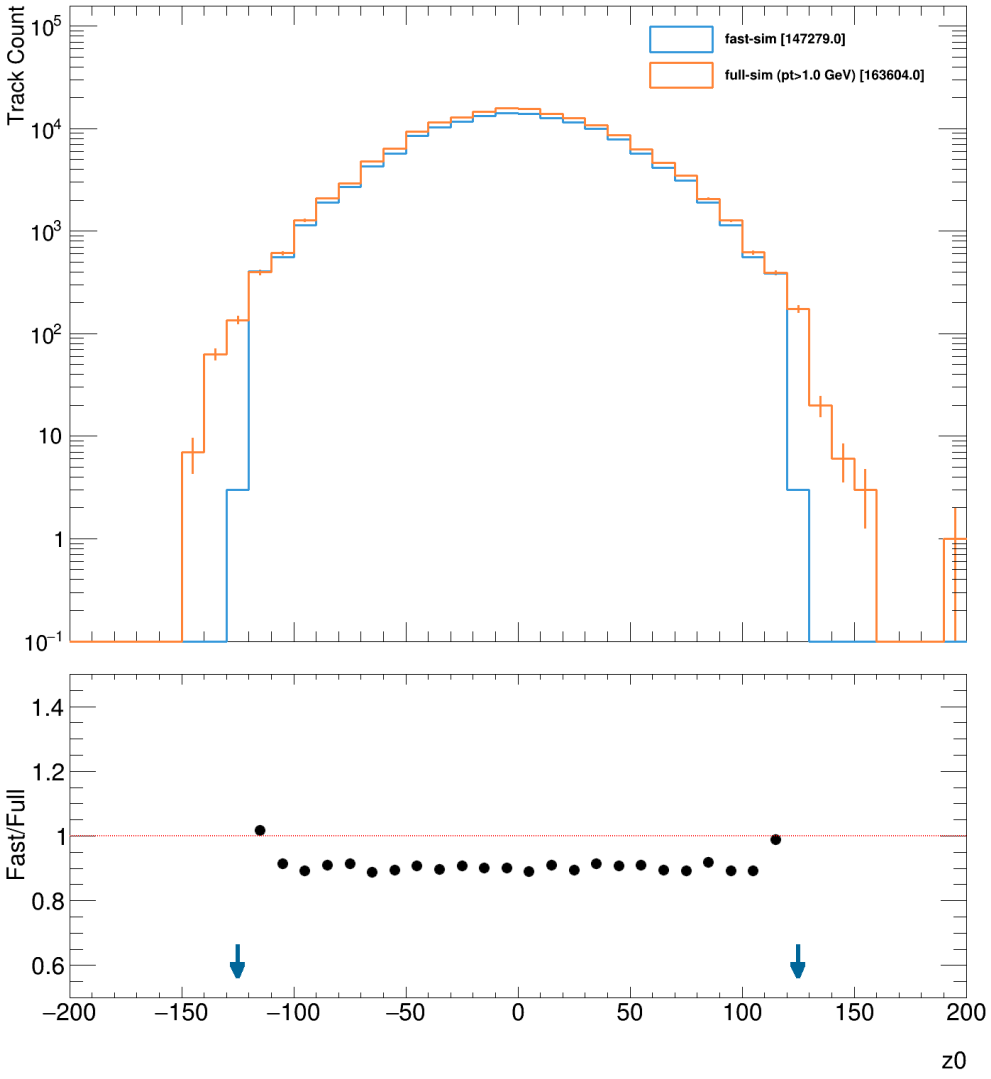


Figure 4.8: A histogram comparing the distribution of the $z0$ track parameter (measured in mm) for FTK tracks generated from full- and fast-simulation for a sample of $t\bar{t}$ events. The bracketed values are the total number of tracks present in the depicted region.

and full-simulation track parameters should agree very closely, in terms of both shape and yield.

Figures 4.4 to 4.8 compare the distributions of the various track parameters for the two simulation versions. Note that an additional selection on the track $p_T$ was applied to the full-simulation tracks as they did not respect the 1 GeV minimum for reconstruction present in the FTK hardware. Even with this correction applied, the yield for full-simulation tracks was still higher than that for fast-simulation in each of the validation plots. As the yield for fast-simulation can be corrected simply by applying an overall normalisation factor to the efficiency map for instance, further investigation of the discrepancy between yields was considered secondary to understanding any differences in the shape of the track parameter distributions.

In general, the shapes of the track parameter distributions agreed quite closely between fast- and full-simulation. The distribution for $\eta$ as seen in Figure 4.4 exhibited particularly good agreement in the central (barrel) region, and degraded performance further towards higher $|\eta|$. This is to be expected to some degree due to the relatively poorly-understood conditions near the boundary between barrel and endcap regions. The shape of the $\phi$ distribution as seen in Figure 4.5 is consistent between the two versions across the whole detector. Naively, one would expect this to be the case given that the detector was designed to be azimuthally symmetric. The shape agreement for track $p_{\mathrm{T}}$ as seen in Figure 4.6 is also quite uniform across the entire $p_{\mathrm{T}}$ range. The only major deviation is at the low $p_{\mathrm{T}}$ cutoff. It is thought that this is due to the poorer modelling of low-$p_{\mathrm{T}}$ tracks, and the differences in how the low-$p_{\mathrm{T}}$ cutoff is handled between simulation versions. The distributions for $d0$ and $z0$ seen in Figures 4.7 and 4.8 respectively feature strong shape agreement in the central region, but the tails for the fast-simulation version terminate sooner than that of the full-simulation. This is due to the presence of hard cutoffs at high $|d0|$ or $|z0|$ in the efficiency map that limit the range of tracks that fast-simulation can handle, while the full-simulation evidently had no such limitations.

With good general agreement between the shapes of track parameter distributions for both full-simulation and fast-simulation, and an understanding of any differences in shape that are present, the smearing algorithm is considered to be a successful candidate for implementing FTK fast simulation. While it would be useful to understand the slight discrepancy in track yields, this discrepancy is easily corrected with an overall normalisation factor and hence it is of lesser concern.

## 4.5 Outlook

The development of a fast simulation was an essential part of the FTK project, and will continue to be of great importance for the development of the FTK's successor, the HTT. As the HTT will reuse the highly successful design of the Associative Memory boards from the FTK, much of the simulation software that was originally written for the FTK will remain relevant and transferable to the HTT. With the unprecedented level of pile-up expected with the HL-LHC upgrade, fast tracking

remains a pertinent field of development for the ATLAS Collaboration, and other experiments at the LHC.

Chapter 5

# Towards a measurement of four-top-quark production in the Standard Model

Of the myriad elementary particles in the Standard Model, the top quark is the heaviest. This affords it a coupling with the Higgs boson that is close to unity. The high mass of the top quark also grants it unparalleled sensitivity to influences from potential sources of new physics beyond the Standard Model. This uniquely positions the top quark as a probe into the nature of the universe at the smallest of scales.

## 5.1 Motivation

The production of four top quarks ($t\bar{t}t\bar{t}$) is one of the rarest processes in the Standard Model due to the large mass of the top quark. The cross section of this process is still yet to be measured. Many of the contemporary beyond Standard Model (BSM) theories predict an enhancement in the $t\bar{t}t\bar{t}$ cross section $\sigma_{t\bar{t}t\bar{t}}$ (for example supersymmetric models [50, 51], pair production of scalar gluons [52, 53], or Type II two-Higgs-doublet models [54–56]), so its measurement may provide insights into the type of BSM theory that nature has chosen.

The predicted Standard Model cross section for four top quark production has been computed to next-to-leading order in both QCD and electroweak interactions, and the latest calculation [57] gives

$$\sigma_{t\bar{t}t\bar{t}} = 11.97^{+18\%}_{-21\%} \text{ fb}^{-1} \tag{5.1}$$

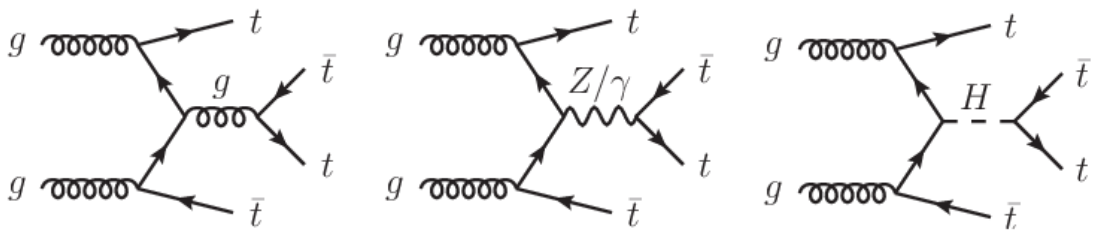


Figure 5.1: Example Feynman diagrams of Standard model $t\bar{t}t\bar{t}$ production.

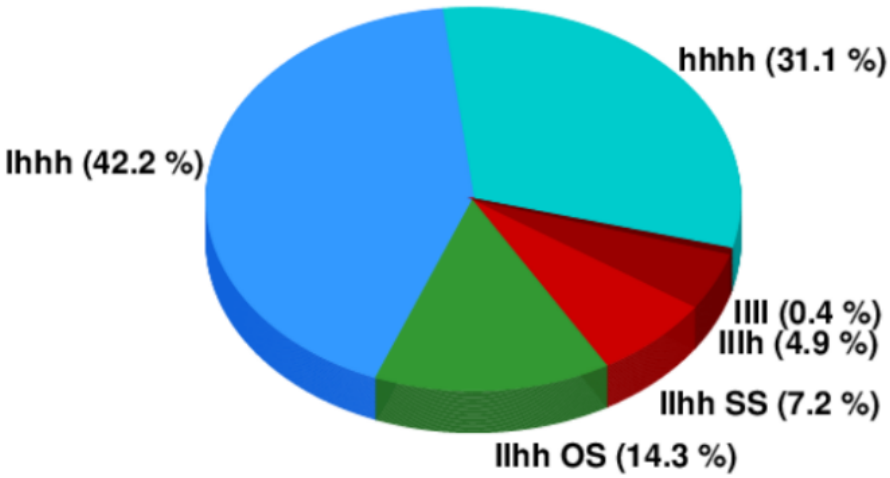


Figure 5.2: Branching ratios of the possible decays of four top quarks. 'l' represents a leptonic decay (i.e. to electron or muon and corresponding neutrino), and 'h' represents an hadronic decay. 'SS' and 'OS' are short for 'same-sign' and 'opposite-sign' respectively, and refer to the charges of the two produced leptons.

at $\sqrt{s} = 13$ TeV. The errors in the predicted cross section account for both uncertainties in the parton distribution function and scale uncertainties. Figure 5.1 shows examples of Feynman diagrams that contribute to the overall cross section.

## 5.2 Analysis Strategy

Top quarks decay almost exclusively into $b$-quarks through the emission of a $W$ boson (see Section 2.3). The $b$-quark subsequently hadronises and forms a $b$-jet, while the $W$ boson can either decay hadronically or into leptons. Hence, the final state of $t\bar{t}t\bar{t}$ production processes will be rich in charged leptons, jets, $b$-jets, and missing transverse energy. Figure 5.2 shows the relative magnitudes of the branching ratios for the possible four-top final states.

In this analysis, the possible final states of four top quark production is separated into two classes: two same-sign leptons or multilepton states (SSML), and one lepton or two opposite-sign lepton states (1LOS). Note that leptons only refer to either electrons or muons, but include those that were produced from the decay of a tau. The 1LOS region has a relatively high branching ratio, but suffers from a proportionally high level of background from $t\bar{t}$ + light jet and $t\bar{t}$ + $b\bar{b}$ events. The SSML channel has a much smaller branching ratio in comparison, however it is compensated by a lower level of background that mainly originates from fake and non-prompt leptons, or $t\bar{t}$ production with additional electroweak bosons. This thesis will primarily document the work that was performed for the SSML channel.

Given the previous characterisation of four top quark production events, the search for these events is focused on final states with at least 6 light jets (of which at least 2 are tagged as $b$-jets) within the SSML channel. Regions of phase space with lower

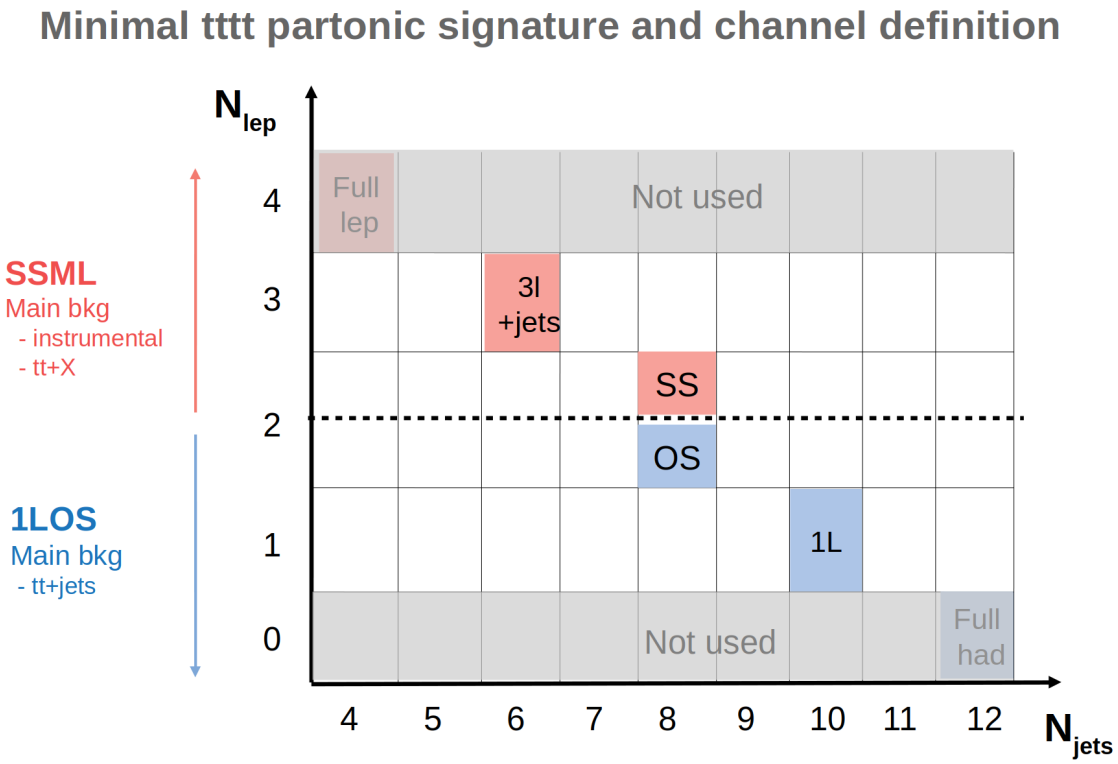


Figure 5.3: Schematic showing the division of $t\bar{t}t\bar{t}$ production final states into the two channels considered in this analysis.

jet multiplicity or object momentum are reserved as control and validation regions. These regions are used for background estimation and adjustment of systematic uncertainties. Figure 5.3 illustrates the division of the phase space across the two channels. Further detail on the definition of regions within the SSML channel is presented in Section 5.6.

## 5.3 Data and Monte Carlo Samples

The dataset used for this analysis is the full LHC Run 2 dataset as recorded by the ATLAS detector during stable beam conditions and nominal detector operation. The average number of interactions per bunch crossing during this period increased from 14 in 2015 to 38 in 2017-2018. Some basic quality selection was performed to remove events with noise bursts or coherent noise in the calorimeters. The integrated luminosity of this dataset was determined to be $139.0 \pm 2.4$ fb$^{-1}$ based on luminosity measurements from LUCID-2 and calibrations from x-y-beam-separation scans [58].

Both the $t\bar{t}t\bar{t}$ signal and the physics background are estimated using Monte Carlo (MC) simulation. These simulation samples are produced by a dedicated team within the ATLAS collaboration. There are four simulation campaigns that correspond to the major beam conditions and configurations during Run 2.

The $t\bar{t}t\bar{t}$ signal process is simulated at both leading order (LO) and next-to-leading order (NLO) using the MadGraph5_aMC@NLO v2.6.2 [59] generator with the NNPDF3.1NLO [60] parton distribution function (PDF). The leading order sample is used in training Boosted Decision Trees as it is more difficult to deal with negatively weighted events in the NLO sample. Top quarks are decayed at leading order (LO) using MadSpin [61, 62] and interfaced with Pythia8.230 [63] for parton showering and hadronisation under the A14 tuned parameter set [64] and the NNPDF2.3LO PDF set [60]. These parameter sets are also used for the modelling for most other processes in this analysis. Bottom and charm decays are simulated using EvtGen v1.6.0 [65]. The ATLAS detector response is simulated with AF2 rather than FullSim - see Section 3.4.2 for more details regarding this difference.

$t\bar{t}$ events are simulated with the PowhegBox v2 generator [66–69] to NLO using the NNPDF3.0NLO PDF set [60] and the $h_{\text{damp}}$ parameter set with 1.5 times the normal top mass [70]. Parton showering and hadronisation is performed by the same Pythia configuration as was used for the signal process. Detector response for these events were simulated with FullSim.

$tW$-associated and s-channel single-top production is modelled using the PowhegBox v2 generator to NLO in QCD in the five flavour scheme [67–69, 71] with the NNPDF3.0NLO PDF set. Single-top t-channel production is modelled using with the same PowhegBox v2 generator to NLO in QCD, but in the four flavour scheme [67–69, 72] with the NNPDF3.0NLOnf4 PDF set [60]. All single top events are interfaced with the same Pythia configuration as the signal process for showering and hadronisation.

$t\bar{t}Z$ events are modelled using the MadGraph5_aMC@NLO v2.3.3 generator [59], while $t\bar{t}W$ events are modelled using the Sherpa v2.2.1 generator [73], both using the NNPDF3.0NLO PDF set. The $t\bar{t}Z$ events are interfaced directly with Pythia8.210 [63] using the usual parameter sets, whereas the matrix elements for $t\bar{t}W$ events were calculated for up to one additional parton at NLO and up to two additional partons at LO using the Comix [73] and OpenLoops [74, 75] libraries before being merged with the Sherpa parton shower [76] using the MEPS@NLO prescription with a merging scale of 30 GeV [77–80]. $tWZ$ events are generated with the MadGraph5_aMC@NLO v2.3.3 generator using the NNPDF2.3NLO PDF set, and interfaced with Pythia8.212 [63] using the usual parameter sets. Other rare top quark processes, i.e. $tZ$, $t\bar{t}WW$ and $ttt$, are all modelled using the MadGraph5_aMC@NLO v2.3.3 generator at LO and interfaced with Pythia8.212 using the A14 tuned parameter set.

$V$+jets production is simulated using the Sherpa v2.2.1 generator with NLO-accurate matrix elements for up to two jets, and LO-accurate matrix elements for up to four jets. The matrix elements were calculated using the Comix [81] and OpenLoops [74, 75] libraries and merged with the Sherpa parton shower using the MEPS@NLO prescription with the tuned parameter set developed by the Sherpa authors. The NNPDF3.0NNLO set of PDFs [60] is used and the samples are normalised to a next-to-next-to-leading order (NNLO) prediction [82].

The final states of diboson processes ($VV$) are modelled with Sherpa v2.2.1 or v2.2.2 [73] depending on the process. Fully leptonic and semileptonic final states are generated using matrix elements to NLO accuracy in QCD for up to one additional parton emission and to LO accuracy for up to three additional parton emissions. Loop-induced processes $gg \to VV$ are generated using LO-accurate matrix elements for up to one additional parton emission, for both fully leptonic and semileptonic final states. The matrix element calculations are matched and merged with the Sherpa parton shower based on Catani-Seymour dipoles [76, 81] using the MEPS@NLO prescription. Virtual QCD corrections are provided by the OpenLoops library. The NNPDF3.0NNLO set of PDFs is used, along with the dedicated set of tuned parton shower parameters developed by the Sherpa authors [73].

Triboson events ($VVV$) are modelled with the Sherpa v2.2.2 generator using factorised gauge boson decays. NLO-accurate matrix elements are used for the inclusive process, and LO-accurate matrix elements are used for emissions of up to two additional partons. The matrix elements are matched and merged with the Sherpa parton shower based on Catani-Seymour dipoles using the MEPS@NLO prescription. The virtual QCD correction for the matrix elements is calculated using the OpenLoops library to NLO accuracy. The samples are generated using the NNPDF3.0NNLO set and the dedicated set of tuned parton shower parameters developed by the Sherpa authors.

| | Electrons | | Muons | | Jets | $b$-jets |
|---|---|---|---|---|---|---|
| | loose | tight | loose | tight | | |
| $p_{\mathrm{T}}$[GeV] | $> 28$ | | $> 28$ | | $> 25$ | $> 25$ |
| $\lvert\eta\rvert$ | $< 2.47$ (excluding crack region) | | $< 2.5$ | | $< 2.5$ | $< 2.5$ |
| ID quality | mediumLH<br>ECIDS ($ee$, $e\mu$) | tightLH<br>ECIDS ($ee$, $e\mu$) | medium | | cleaning + JVT | MV2c10 77% |
| Isolation | none | FCTight | none | FixedCutTightTrackOnly | | |
| Track vertex : | | | | | | |
| – $\lvert d_0/\sigma_{d_0}\rvert$ | $< 5$ | | $< 3$ | | | |
| – $\lvert z_0 \sin\theta\rvert$ [mm] | $< 0.5$ | | $< 0.5$ | | | |

Table 5.1: Summary of object definitions and selections. Items centred across both loose and tight subcolumns apply to both.

## 5.4 Object Definitions

The physics objects that were used in this analysis are electrons, muons, jets, $b$-jets and missing transverse momentum. This section gives the definitions for these objects in terms of selections and choice of working points. See Table 5.1 for a summary of these definitions.

Electrons used in this analysis are defined by the "TightLH" working point from the likelihood-based electron identification, and have the "FCTight" isolation requirement. Electrons in the crack region ($1.375 < |\eta| < 1.475$) are rejected, and the additional selections $p_{\mathrm{T}} > 28$ GeV and $|\eta| < 2.47$ are applied for the SSML channel. A further selection is available for reducing the frequency of events with mis-reconstructed electron charges; the electron charge identification selector (ECIDS) is a boosted decision tree (BDT) discriminant based on the variables $p_{\mathrm{T}}, \eta, q \times d_0, E/p, \Delta\phi_2^{\text{re-scaled}}$ (angle between the location of the deposit in the second calorimeter layer and the extrapolated track) and the average charge weighted by the number of SCT hits.

Muons are based on the "Medium" working point for muon identification, the "FixedCutTightTrackOnly" working point for isolation, and have the additional selections of $p_{\mathrm{T}} > 28$ GeV and $|\eta| < 2.5$. A set of standard cuts recommended by the Muon Combined Performance Working Group are also applied to muon $d_0$ and $z_0$.

Jets are reconstructed from topological calorimeter clusters using the anti-$k_t$ algorithm with a radius parameter of $R = 0.4$. The JetVertexTrigger (JVT) is applied to these reconstructed jets to minimise jets originating from pile-up collisions. Furthermore, a selection of $p_T > 25$ GeV and $|\eta| < 2.5$ are applied to jet candidates.

$b$-tagging for the analysis is performed with a multivariate algorithm called MV2c10 which produces a discriminant $w$ with values between $-1$ and $+1$. MV2c10 provides four working points that correspond to different tagging efficiencies: 60%, 70%, 77% and 85%. However, a pseudo-continuous $b$-tagging score is also used in the analysis. This pseudo-continuous score is based on which (if any) of the working points a given jet passes, taking a value of 1 for jets that do not pass any of the

working points, and increasing for each passed working point up to a value of 5 for jets that pass the 85% working point.

The missing transverse momentum vector $\mathbf{p}_{\mathrm{T}}^{\mathrm{miss}}$ with magnitude $E_{\mathrm{T}}^{\mathrm{miss}}$ is used to define candidate neutrinos and other weakly interacting particles as they otherwise leave no trace in the detector. $\mathbf{p}_{\mathrm{T}}^{\mathrm{miss}}$ is defined by

$$\left(\mathbf{p}_{\mathrm{T}}^{\mathrm{miss}}\right) = \left(\mathbf{p}_{\mathrm{T}}^{\mathrm{miss}}\right)^{\mathrm{Electrons}} + \left(\mathbf{p}_{\mathrm{T}}^{\mathrm{miss}}\right)^{\mathrm{Muons}} + \left(\mathbf{p}_{\mathrm{T}}^{\mathrm{miss}}\right)^{\mathrm{Jets}} + \left(\mathbf{p}_{\mathrm{T}}^{\mathrm{miss}}\right)^{\mathrm{Soft\ Term}}, \qquad (5.2)$$

where the missing transverse momentum for a set of objects is the negative vector sum of their momentum, and $\left(\mathbf{p}_{\mathrm{T}}^{\mathrm{miss}}\right)^{\mathrm{Soft\ Term}}$ is the missing transverse momentum assigned to tracks and calorimeter deposits not associated with any physics objects.

## 5.5 Event Selection

All events that were considered in the analysis were required to pass a preliminary set of requirements known as the preselection. Preselection places requirements on the data quality, triggers, and physics objects in each event to narrow down the dataset to events that are relevant to the signal of interest. For the SSML channel, the preselection requirements were as follows:

- at least one vertex containing at least two tracks with $p_{\mathrm{T}} > 0.4$ GeV,
- at least 2 same-sign leptons with $p_{\mathrm{T}} > 28$ GeV,
- at least 1 $b$-tagged jet,
- a reconstructed $Z$-mass $m_{ll}$ outside a window centred on $m_Z$ defined by $81 < m_{ll} < 101$ GeV, where $m_{ll}$ is calculated from the two leptons for same-sign events, or from the opposite-sign same-flavour lepton pair for 3 lepton events.

## 5.6 Background Estimation

In order to extract the $t\bar{t}t\bar{t}$ cross section from the data, an estimate of the backgrounds present in the selected region must be made. The primary backgrounds in the SSML channel can be grouped into three main categories. The first category is for events where the leptons originated from the decays of $W$ or $Z$ bosons. The second category is for charge misidentification ("QmisID"), which contains events with an opposite sign dilepton pair where one lepton has its charge mis-reconstructed to appear as a same sign pair. The final category is referred to as "fake/non-prompt leptons", which includes events which have either one lepton that originated from heavy flavour $c$ or $b$ decays, an electron that originated from $\gamma$-conversion, or another particle (originating from quark or gluon jets) that was mis-reconstructed as an electron.

The $W$ and $Z$ background is evaluated using Monte Carlo simulation. These processes were found to be mostly well modelled, except for $t\bar{t}W$ which has its overall normalisation and signal strength fitted against data.

The QmisID background is estimated using a data-driven method. There are two main sources of charge misidentification for electrons: extremely high momenta electrons with almost straight tracks; and electrons that radiate a photon through bremstrahlung, which subsequently converts into an electron-positron pair and interferes with identifying the initial electron. The rate of charge mis-identification for muons is negligible in comparison due to the large tracking volume provided by the muon spectrometer and the reduced level of bremstrahlung for muons. The data-driven method calculates the probability of electron charge misidentification from a sample of dilepton events at the $Z$ mass peak which otherwise has the same selections as the signal region. This probability is used to determine the expected number of charge misidentification events in a given sample.

The fake/non-prompt background was estimated using a template fit method. In this method, a number of regions within the preselection are defined: control regions (CRs), validation regions (VRs) and signal regions (SRs). Each region is defined by a set of further *cuts* or requirements on the preselection events. The SRs are defined first, in regions where the signal process is expected to be most dominant. The CRs and VRs are defined next so that they are orthogonal to the SRs (no overlap of events), but still nearby in the sense that the kinematics of contained events will not be too dissimilar. The SRs are *blinded*, so data events in SRs are not available until the analysis is finalised. This is an effort to prevent optimisation of region definitions based on the perculiarities of the dataset that is available, rather than on the physics of the events that are being studied. The idea of the template fit method is to first investigate the data/MC agreement for each major background in a control region in which it is enhanced. The overall normalisation for each background's MC is then adjusted to match the data in a *fit*. This fit is then propagated to the VRs to test how well the adjusted MC matches data outside its fitted region. Once satisfied that the fit is correctly adjusting MC to match the data it is propagated to the SRs where, after unblinding, it will be used to test the significance of the signal against a background-only hypothesis. If sufficient evidence for four top production is found, a measurement of the cross section will also be performed.

Signal extraction for the SSML region in this analysis is performed using a Boosted Decision Tree (see Section 5.8 for more details).

### 5.6.1 Control Region Studies

For the background template fit to perform optimally, each fitted background requires a control region in which it is suitably enhanced and a kinematic variable over which that background distributes itself differently to other backgrounds. To this end, a number of studies were performed to identify the optimal control region definitions and kinematic variables to fit on. Initially the shapes of the various fake and non-prompt background events were investigated for a range of different variables. A histogram was created for each variable, and the contributions of each MC background were normalised to unit integral. Good candidates for variables to use in the fit would have a drastically different shape for one background category compared

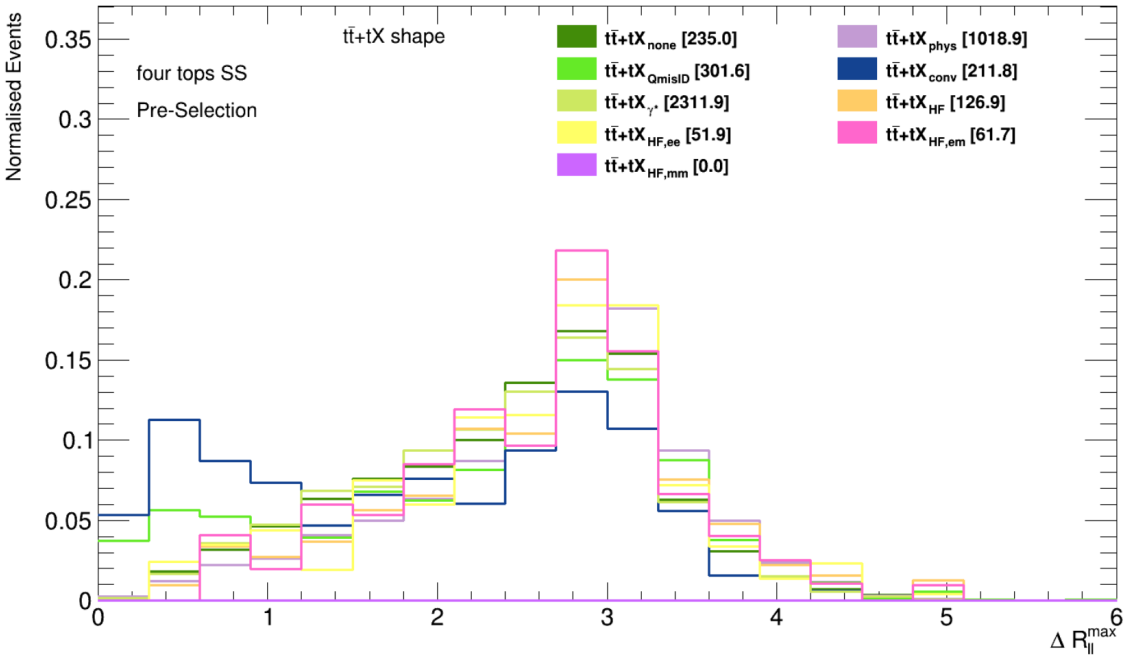


Figure 5.4: Histogram showing the shape of the fake/non-prompt backgrounds for $t\bar{t}$ events for the variable $\Delta R_{ll}^{\max}$. The bracketed values are the total number of MC simulation events for each background.

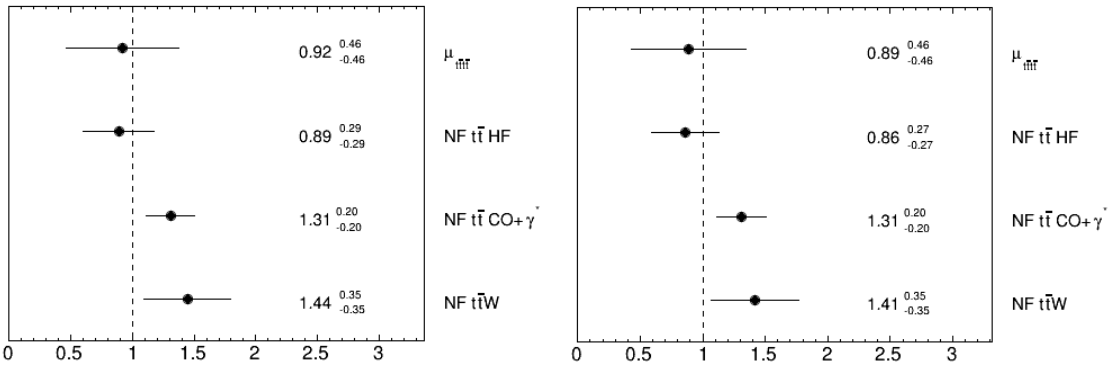


(a) (b)

Figure 5.5: Fitted normalisation factors (NFs) for two configurations. Subfigure 5.5a shows the NFs for the original configuration, while Subfigure 5.5b shows the NFs for the improved baseline configuration. The $x$-axis shows the value of the normalisation factor. Values closer to 1 are better.

to the others. An example of such a variable is shown in Figure 5.4, where the conversions background is separated from the rest of the backgrounds that all peak near $\Delta R_{ll}^{\max} = 3$. The candidate variables that were identified were $\Delta R_{ll}^{\max}$ and lepton charge sum for the $t\bar{t}W$ control region, and lead lepton $p_{\mathrm{T}}$ for the heavy flavour control region (labelled CR1b3l or just 1b3l).

The effectiveness of the candidate variables were then investigated. A series of variations on the initial region definitions were tested, using the correlation matrix and normalisation factors (NFs) after fitting to gauge the effectiveness of each variation. See Appendix A for tabulations of the initial region definitions. Ideally the non-diagonal entries of the correlation matrix would all be zero, as higher correlations (or anti-correlations) between variables leads to higher overall uncertainties. The ideal for the set of normalisation factors is for them all to be 1, as that indicates each region is well modelled.

One of the first variations tested used lead lepton $p_{\mathrm{T}}$ for the CR1b3l variable and lepton charge sum for the CRttW variable. Other changes in this version included adding a $nJets \geq 6$ cut to the CRttZ definition to enhance purity, and fixing the QmisID normalisation rather than using the fit to determine it (this was prior to using the data-driven estimate). This led to a modest improvement in both the $t\bar{t}W$ normalisation factor and in the correlation matrix, so this configuration was used as a new baseline on which further variations were tested. Figure 5.5 compares the fitted normalisation factors between the original configuration and the improved baseline configuration. See Appendix B for comparisons of the correlation matrices between configuration versions.

The next set of variations (collectively labelled as the "Combined" variations) investigated whether further improvements could be gained by subdividing the signal regions based on lepton flavour, and secondly by subdividing the $t\bar{t}W$ control region by lepton flavour or number of $b$-jets (or both). The first configuration that was tested implemented a splitting of the $t\bar{t}W$ control region into the three lepton flavour combinations: $ee$, $em$ and $mm$. This resulted in a comparable set of NFs and correlations to the previous configuration. The next variation implemented a splitting of the control regions by their lepton flavours: $ee$, $em$, $mm$ for 2 lepton regions, and $eee$, $eem$, $emm$, $mmm$ for 3 lepton regions. This resulted in a somewhat worse set of NFs and correlations than the baseline configuration. The two sets of splittings were combined in a third variation. This version also used a separate normalisation factor for each $t\bar{t}W$ subregion, but exhibited even poorer NFs and correlations than previous versions. The next variation split the $t\bar{t}W$ control region (and normalisation factor) by the number of $b$-jets while still splitting the signal regions by flavour. This produced some comparable correlations to the baseline configuration, but the NFs were still somewhat worse. The last variation split the $t\bar{t}W$ control region by both $b$-jets and lepton flavour in addition to the signal region splitting, while using a single normalisation factor for $CRt\bar{t}W$. Interestingly, this resulted in a somewhat improved set of NFs and comparable correlations. See Figure 5.6 for a comparison

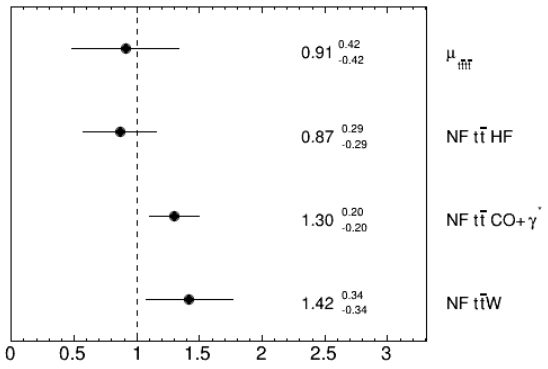


(a) Signal regions split by flavour

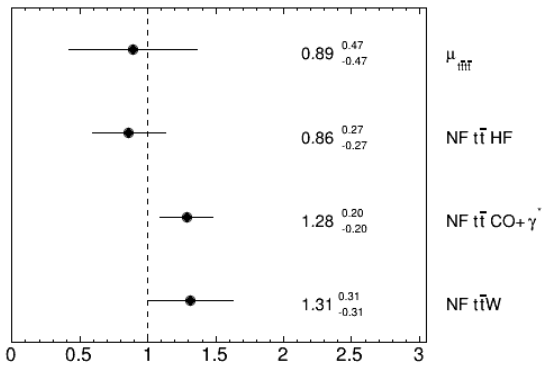


(b) $CRtt\bar{W}$ split by flavour

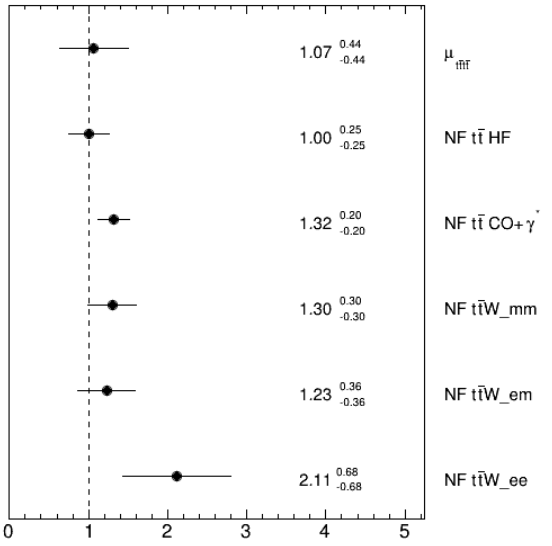


(c) Both signal and $CRtt\bar{W}$ regions split by flavour

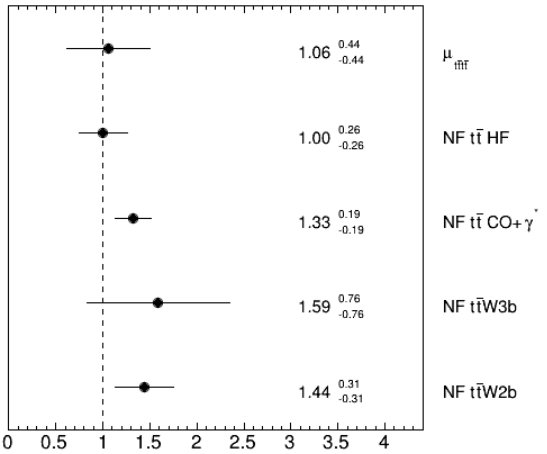


(d) Signal region split by flavour, $CRtt\bar{W}$ split by $b$-jets

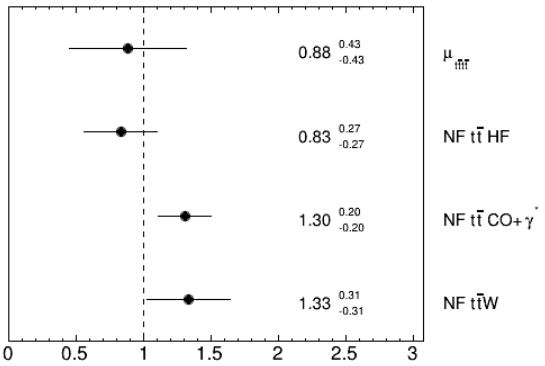


(e) Signal region split by flavour, $CRtt\bar{W}$ split by flavour and $b$-jets

Figure 5.6: Fitted normalisation factors (NFs) for the "Combined" set of variations. The $x$-axis shows the value of the normalisation factor.

| | Single | Flavour | Bjets | Full |
|---|---|---|---|---|
| Main correlations | NF ttW vs QmisID ∼ 45%<br>QmisID vs NF tt CO+$\gamma^*$ ∼ 38% | QmisID vs NF tt CO+$\gamma^*$ ∼ 39%<br>$\mu_{t\bar{t}t\bar{t}}$ vs btag Light0 ∼ 33% | NF ttW vs QmisID ∼ 48%<br>btagCO vs NF ttW ∼ 45% | btagCO vs NF ttW ∼ 45%<br>QmisID vs NF tt CO+$\gamma^*$ ∼ 38% |
| ttW NF | 1.42±0.35 | 1.36±0.32 | 2b 1.36±0.32<br>3b 1.56±0.75 | 2b 1.28±0.28<br>3b 1.54±0.72 |
| 4top sig. | 2.43 | 2.46 | 2.25 | 2.26 |

Table 5.2: Summary of results from the $t\bar{t}W$ control region splitting study.

| | Main correlations | ttW NF | 4top sig. |
|---|---|---|---|
| Baseline | NF ttW vs QmisID ∼ 78%<br>ttZ Xsec vs others Xsec ∼ 54% | $1.0^{+0.42}_{-0.42}$ | 2.50 |
| Cbtag | NF ttW vs QmisID ∼ 78%<br>btagLight0 vs btagC0 ∼ 56% | $1.01^{+0.42}_{-0.42}$ | 2.52 |
| 1b3l | NF ttW vs QmisID ∼ 79%<br>btagLight0 vs btagC0 ∼ 57% | $0.96^{+0.42}_{-0.42}$ | 2.50 |
| QmisID | NF ttW vs QmisID Xsec ∼ 55%<br>ttZ Xsec vs others Xsec ∼ 54% | $1.11^{+0.32}_{-0.32}$ | 2.55 |
| ttW | NF ttW vs QmisID ∼ 66%<br>NF ttW vs ttW Xsec ∼ 57% | $1.64^{+0.49}_{-0.40}$ | 2.38 |
| ttZ | NF ttW vs QmisID ∼ 77%<br>btagLight0 vs btagC0 ∼ 64% | $0.93^{+0.42}_{-0.42}$ | 2.47 |
| SR_Split | NF ttW vs QmisID ∼ 74%<br>ttZ Xsec vs others Xsec ∼ 54% | $1.05^{+0.39}_{-0.39}$ | 2.54 |
| Combined | NF ttW vs QmisID Xsec ∼ 54%<br>NF ttW vs ttW Xsec ∼ 52% | $1.11^{+0.32}_{-0.32}$ | 2.60 |

Table 5.3: Summary of results from the *debug* control region study.

of the normalisation factors for each of these variations. The correlation matrices for each variation can be found in Appendix B.

At this point a similar study was required for a new trial splitting scheme for the signal regions; this intermediate scheme split the signal regions into the flavour categories $ee + em$ and $mm$. The aim of the new study was to investigate the effect of different splittings of the $t\bar{t}W$ control region under the updated scheme. A total of four different configurations were tested in this study. The first configuration (labelled as "Single") was simply a baseline configuration with no splitting of the $t\bar{t}W$ control region for comparison purposes. The "Flavour" variation split the control region into the $ee + em$ and $mm$ flavour categories while maintaining a single normalisation factor to fit on. The "Bjets" configuration split the $t\bar{t}W$ region into the $2b$ and $\geq 3b$ categories, and had one normalisation factor for each of the two sub-regions. The "Full" configuration used a hybrid splitting scheme: $2b$ $ee$+$em$, $2b$ $mm$, and $\geq 3b$, with two normalisation factors (for each $b$-jet category). It was determined that splitting the $t\bar{t}W$ control region by lepton flavour tended to improve correlations, whereas the splitting by $b$-jets tended to be ineffective. The recommendation from this study was the "Flavour" configuration, which exhibited the best overall behaviour. Table 5.2 summarises the results from testing these configurations.

After the conclusion of the $t\bar{t}W$ control region study, the analysis group released a new major configuration version. The next study investigated the effect of reimplementing many of the previous changes in the latest configuration version. This time a total of 8 different variations were tested, including a baseline version with no change from the official version. The 7 remaining variations were as follows:

- *Cbtag*: changes the Monte-Carlo event weight to use a continuous $b$-tagging score instead of the 77% working point
- *1b3l*: fit on lead electron $p_{\mathrm{T}}$ for the 1b3l control region
- *QmisID*: fix the normalisation factor for QmisID rather than fitting it
- *ttW*: fit on lepton charge sum for the $t\bar{t}W$ control region
- *ttZ*: add the nJets $\geq 6$ cut to the CRttZ control region definition and adjust the binning (since it fits on the nJets variable).
- *SR_split*: split all signal regions (except the $4b$ region) by lepton flavour category ($ee + em$ and $mm$)
- *Combined*: combines the changes from *Cbtag*, *1b3l*, *QmisID* and *SR_split*, the variations with the best significance values

The results from this series of variations are summarised in Table 5.3. The recommendation from this study was to use the *Combined* configuration as it improved upon the significance and correlations, while maintaining a reasonable $t\bar{t}W$ normalisation factor.

### 5.6.2 Anomaly Investigation

An anomaly was discovered in the 2b3l validation region, where the data exhibited a significant excess compared to the MC prediction (see Figure 5.7). To better understand the cause of this discrepancy, a study was undertaken to identify the source of the anomalous data events. First the region was split over lepton flavour categories ($eee + eem$ and $emm + mmm$) and by year. As shown in Figure 5.8, the excess is present in both electron and muon categories. From the plots in Appendix C that further split each flavour category over data period, it can be seen that there is also a smaller excess in the $Njets = 3$ bin for the 2015-2016 and 2017 data taking periods, which was previously hidden by an under-fluctuation in the 2018 period. To study the anomalous events in more detail, an additional cut of $Njets == 2$ was applied. The distributions of other kinematic variables were then investigated to try and gain some intuition on the cause of the mismodelling.

The first two variables investigated were the $\eta$ and $p_{\mathrm{T}}$ of the lead electron or muon depending on the flavour category. Their distributions can be seen in Figures 5.9 and 5.10 respectively. Further plots showing the splitting by year in addition to flavour category can be found in Appendix C. From these, it can be seen that the

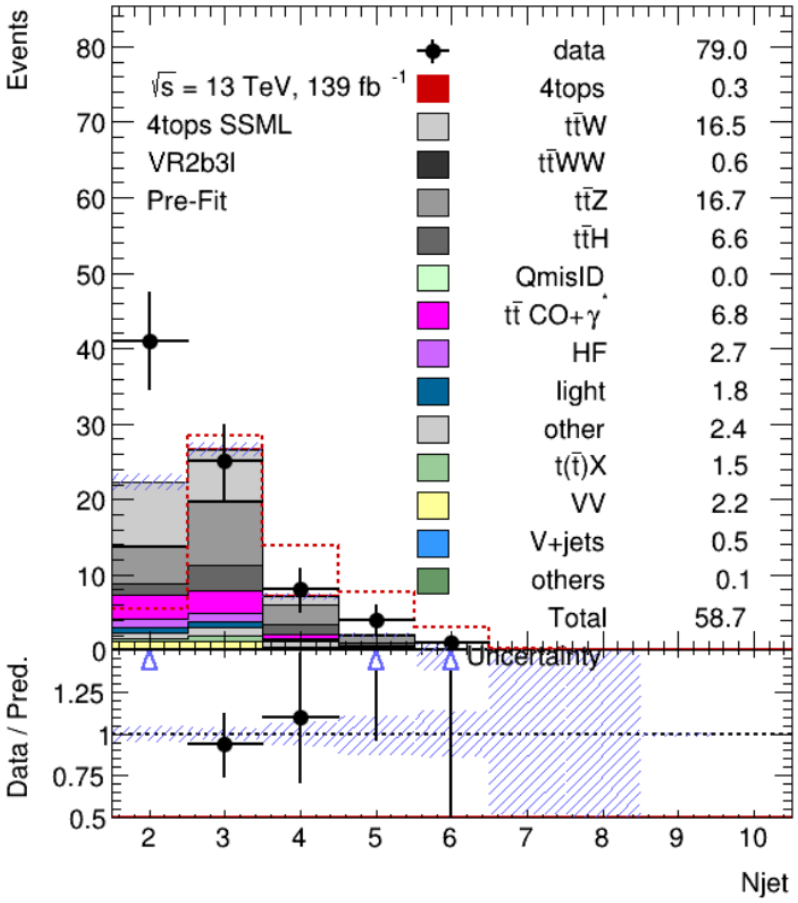


Figure 5.7: The 2b3l validation region. The black points with error bars are the data events from 2015-2018. The coloured bars are the Monte Carlo estimates for each background process. Note the large discrepancy between data and MC in the first $Njet = 2$ bin.

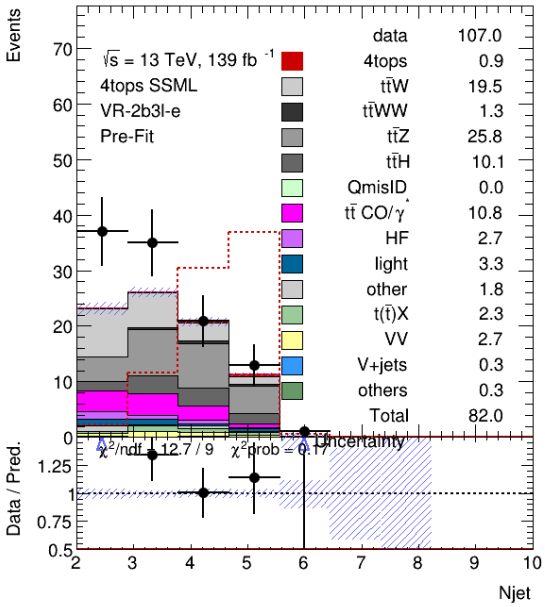


(a) $eee + eem$ events, pre-fit

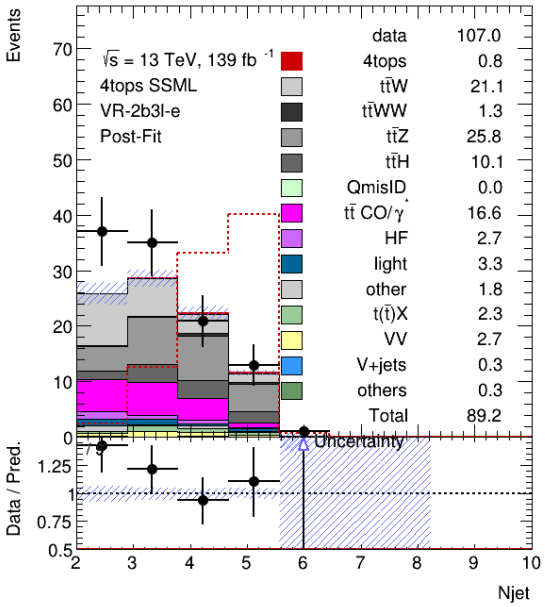


(b) $eee + eem$ events, post-fit

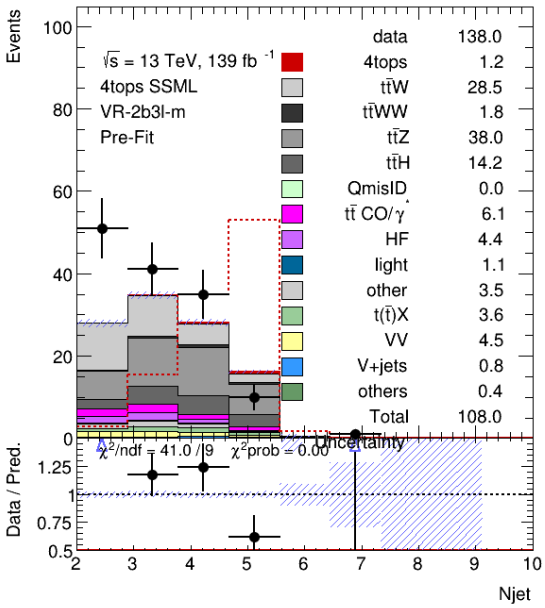


(c) $emm + mmm$ events, pre-fit

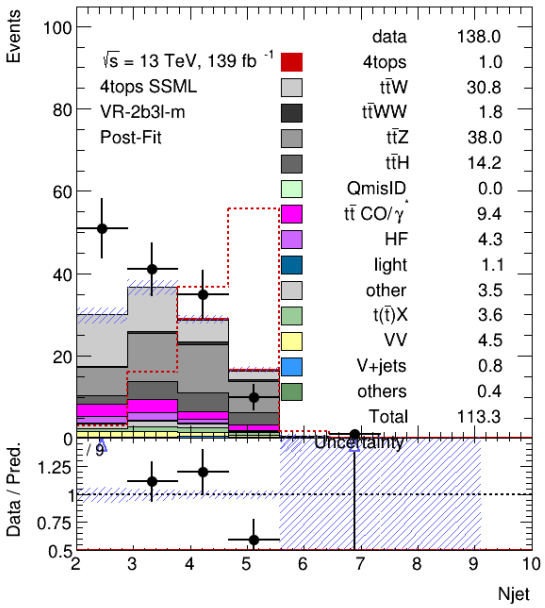


(d) $emm + mmm$ events, post-fit

Figure 5.8: Flavour category split of the 2b3l validation region.

data excesses are relatively uniform across $\eta$, but are concentrated in low $p_{\mathrm{T}}$ bins. When looking at individual data periods, the modelling for 2015-2016 muons and 2018 electrons appears particularly poor in the $p_{\mathrm{T}}$ plots. A further "variable" that was investigated was the lepton flavour combination in each event, in case the excess primarily comes from mixed electron and muon events for instance. Figure 5.11 shows the distribution of lepton flavour combinations in each flavour category, while the plots showing further splitting over data period can be found in Appendix C.

Overall, there were no clear kinematic features for this excess other than the concentration in the low $p_{\mathrm{T}}$ region. One explanation that was investigated was that a process was missing from the Monte Carlo modelling, however all candidate processes that were considered were unable to account for the observed excess. While there was no consensus on an explanation for this excess, it was concluded that the validation region in consideration was kinematically too distant from the control and signal regions for this to affect the analysis, as no such excess was visible in the control regions.

## 5.7 Systematic Uncertainties

The measurement of the $t\bar{t}t\bar{t}$ cross-section is impacted by several sources of systematic uncertainties. These uncertainties can be grouped into two broad categories: experimental systematics, and theoretical systematics. The experimental systematics account for errors in calibration and measurement in the various detector systems. It includes uncertainties for luminosity measurement; pile-up reweighing; lepton reconstruction, identification, isolation and triggers; lepton momentum scale and resolution; jet vertex tagging; jet energy scales; jet energy resolution; jet tagging; charge flips; and fake leptons. The theoretical systematics cover uncertainties in Standard Model parameters that are used for MC generation of backgrounds. These include uncertainties in the $t\bar{t}$ matrix element; $t\bar{t}$ parton showers and hadronisation; $t\bar{t}$ radiation modelling; the parton distribution function for protons; and overall background normalisation factors.

## 5.8 Multivariate Analysis

As mentioned in Section 5.6, a Boosted Decision Tree (BDT) is used for signal extraction in the SSML channel. The ROOT Toolkit for Multivariate Analysis [83] (TMVA) is used to perform the BDT analysis, using ROOT version 6.10.04. A BDT is an example of a multivariate analysis. It consists of an ensemble of decision trees which are combined via *boosting* to form a strong classifier. A decision tree is composed of a series of *nodes*. Each node splits input data based on a given variable. Terminal nodes are called *leaves*, and represent the output of a decision tree. See Figure 5.12 for a visualisation of a typical decision tree. A decision tree on its own is ineffective at making accurate classifications. Boosting refers to any technique that can produce an arbitrarily accurate prediction model from an ensemble of weaker

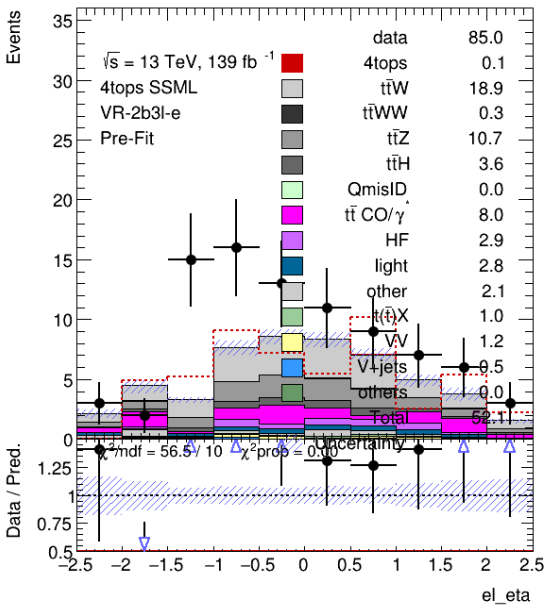


(a) $eee + eem$ events, pre-fit

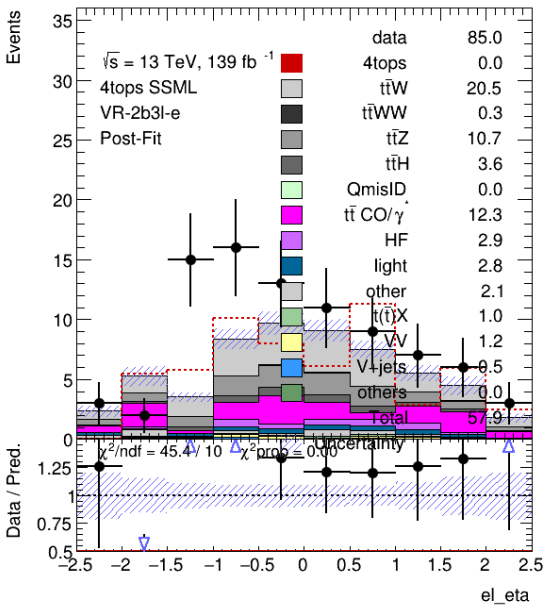


(b) $eee + eem$ events, post-fit

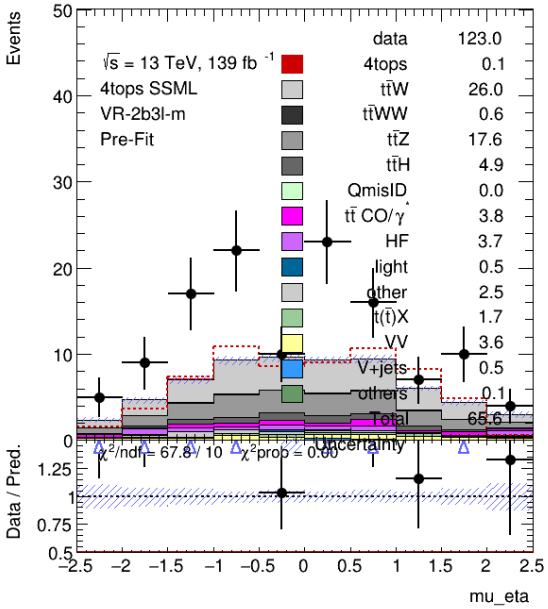


(c) $emm + mmm$ events, pre-fit

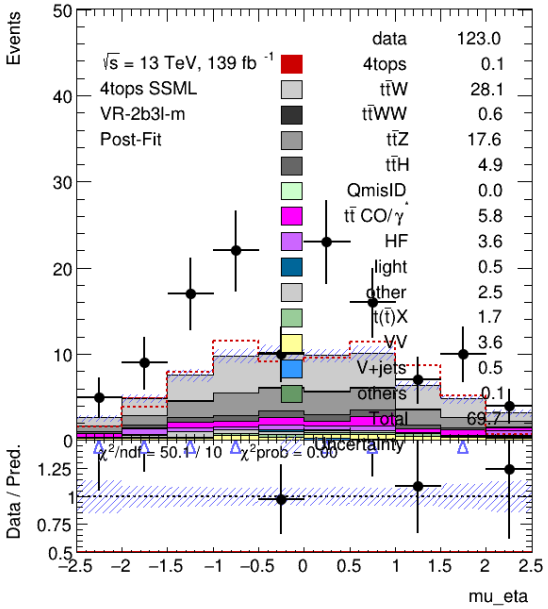


(d) $emm + mmm$ events, post-fit

Figure 5.9: Flavour category split of the 2b3l validation region, showing the distribution of the lead electron $\eta$ for $eee + eem$ events and lead muon $\eta$ for $emm + mmm$ events.

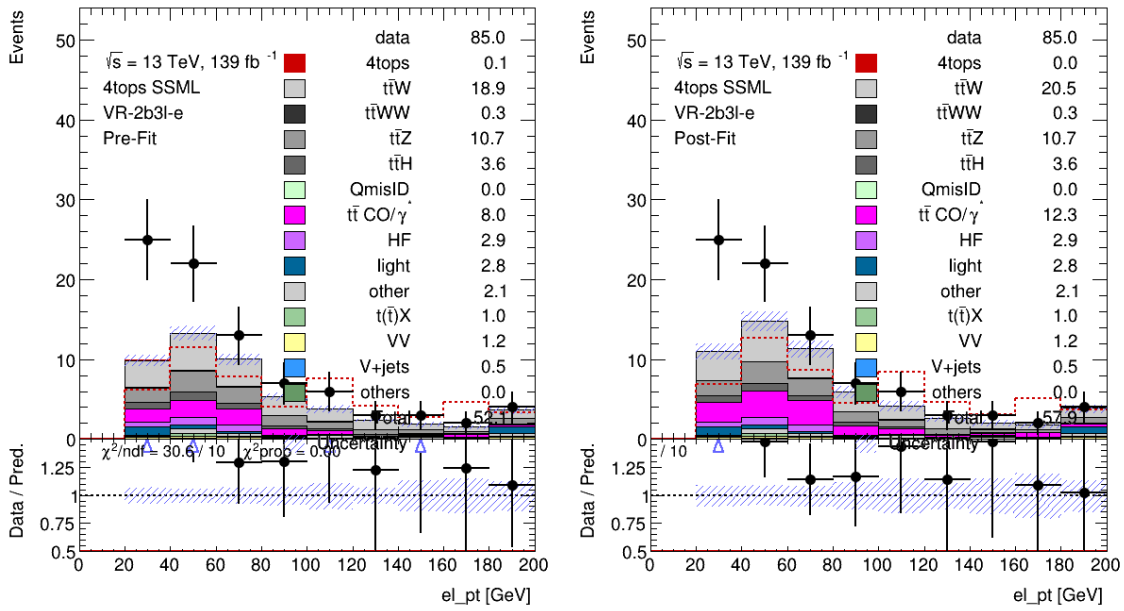


(a) $eee + eem$ events, pre-fit

(b) $eee + eem$ events, post-fit

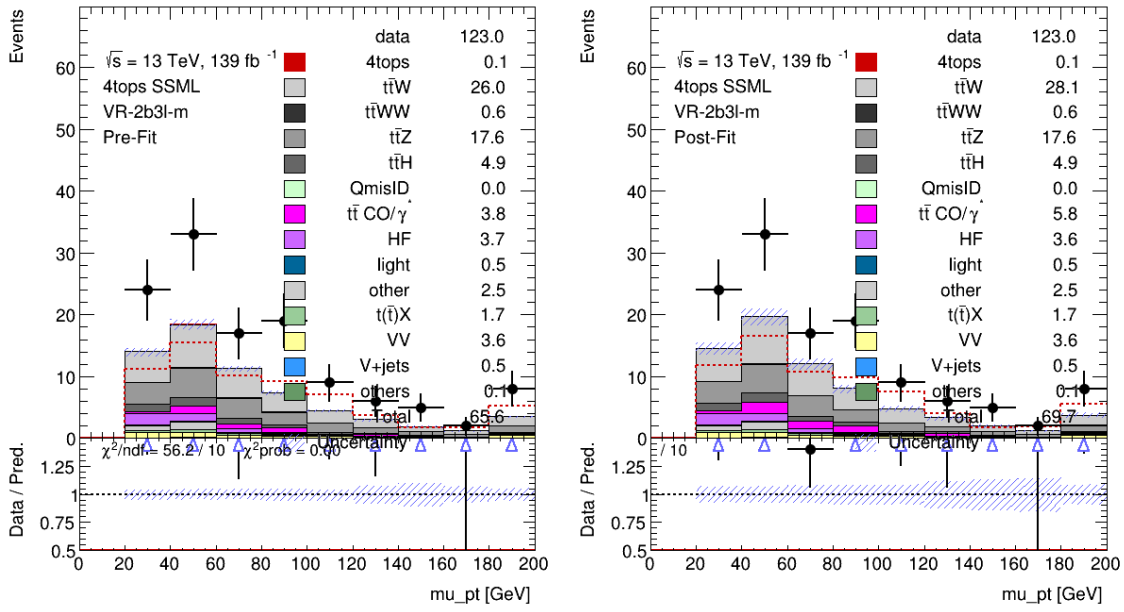


(c) $emm + mmm$ events, pre-fit

(d) $emm + mmm$ events, post-fit

Figure 5.10: Flavour category split of the 2b3l validation region, showing the distribution of the lead electron $p_{\mathrm{T}}$ for $eee + eem$ events and lead muon $p_{\mathrm{T}}$ for $emm + mmm$ events.

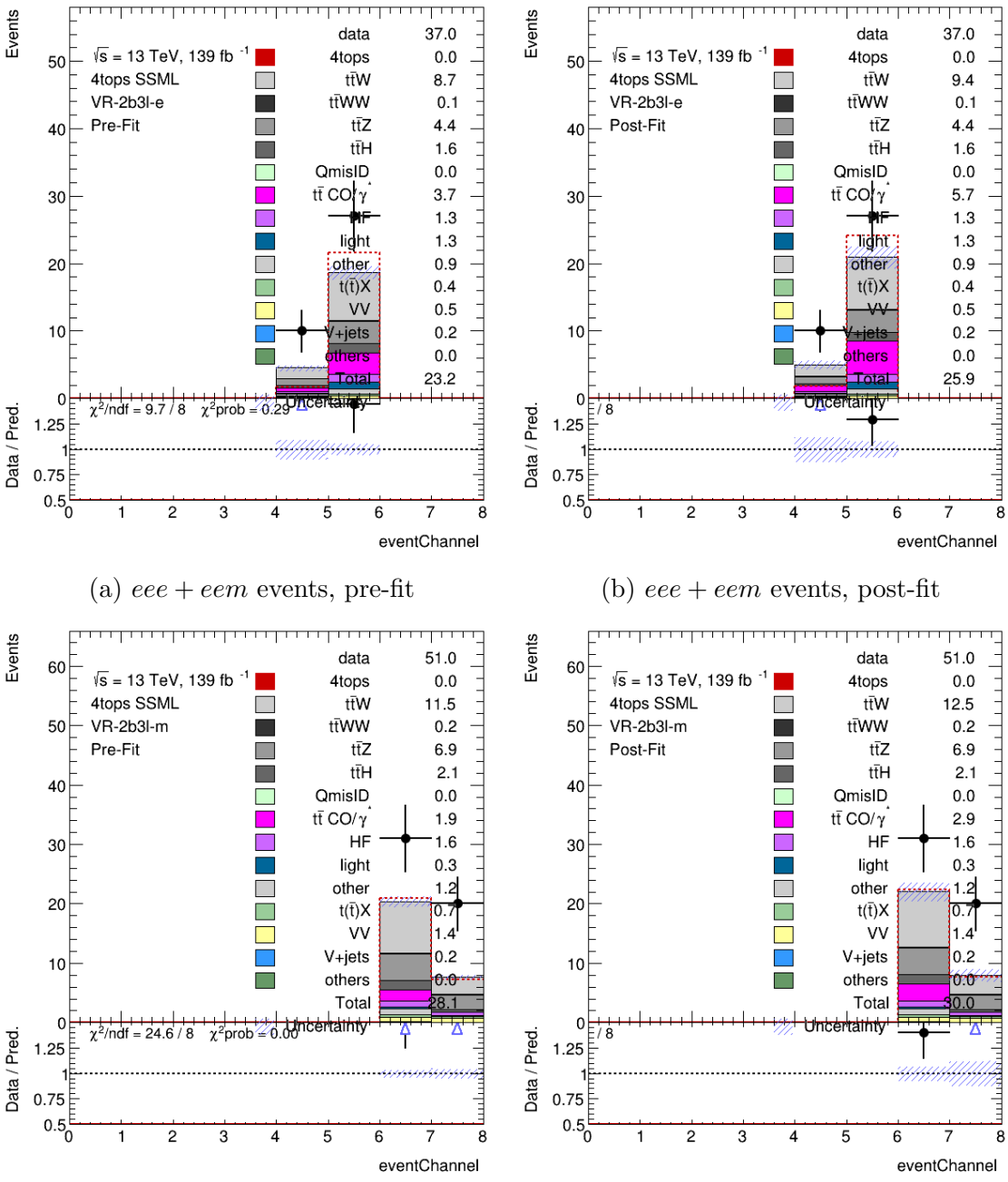


(a) $eee + eem$ events, pre-fit

(b) $eee + eem$ events, post-fit

(c) $emm + mmm$ events, pre-fit

(d) $emm + mmm$ events, post-fit

Figure 5.11: Flavour category split of the 2b3l validation region, showing the distribution of lepton flavour combinations within each category. Here a value of 4 represents $eee$ events, 5 for $eem$, 6 for $emm$, and 7 for $mmm$ events.

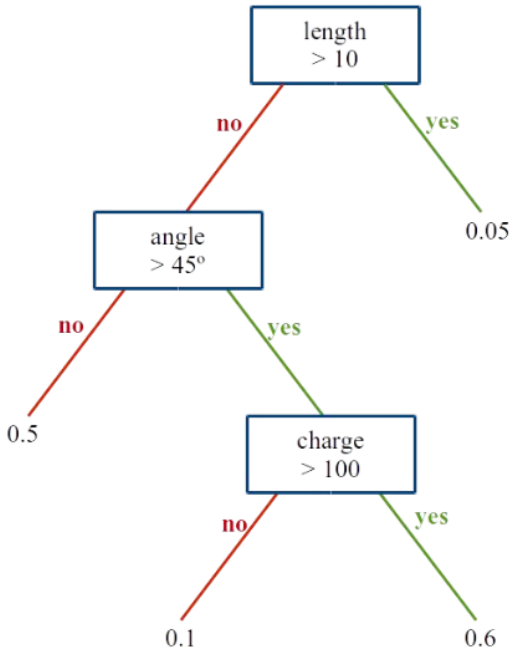


Figure 5.12: Schematic of a decision tree. Each blue box represents a node, and the terminal nodes or leaves are the classification output of the decision tree.

classifiers in an iterative fashion. A typical boosting technique used for decision trees is known as gradient boosting. Each iteration of this process constructs a new decision tree that tries to predict the residuals of the previous tree. The cumulation of all these trees is used as the final model. In this analysis, the BDT is used to classify events in the signal region as being either signal-like or background-like.

### 5.8.1 Training Scheme

There are three major steps in the production of a BDT: training, testing and validation. During the training phase, the BDT is provided with true classification data with which it "learns" to classify events through the boosting algorithm. In the testing phase, the trained BDT is provided with an orthogonal dataset to produce predictions on. The BDT predictions are compared with the true event classification to test and correct for *overtraining*. Overtraining or overfitting is where the BDT is discriminating based on features particular to the sample rather than real features that distinguish signal and background events. The validation step is similar to the testing step; the BDT is provided with another orthogonal dataset on which its predictions are tested against true classification data. While a BDT could be considered ready for use after just the training and testing steps, the validation step is used to make doubly sure that any overtraining has been corrected as overtraining was found to be a prevalent issue in early BDT studies.

| Parameter | Value |
|---|---|
| Max D | 6 |
| nCuts | 15 |
| nMin% | 3 |
| Shrinkage | 0.01 |
| Bagging | 0.7 |
| nTrees | 800 |

Table 5.4: Optimised BDT hyperparameters.

The BDT for this analysis was trained on the MC events in the signal region (see Table 5.6 for the definition of this region). The events from the signal region was divided into three subsets. The first subset contained 20% of the total number of events and was withheld for the validation step. The remaining 80% of the signal region events was further divided into odd and even numbered events resulting in two further subsets each containing 40% of the total number of events. One BDT was trained on the odd event set and tested on the even events, while a second BDT was trained on the even events and tested on the odd events. Both odd and even BDTs were then retested on the validation set.

### 5.8.2 Hyperparameter Selection

There are two sets of parameters that need to be set to define the behaviour of the boosting algorithm. The first set of parameters relate to how the decision trees are constructed; these are:

- Maximum depth (Max D), the number of nodes between the first node and the furthest leaf.
- Number of cuts (nCuts), the total number of nodes in a tree, which can be thought of as controlling the width of a tree.
- Minimum event fraction (nMin%), the minimum number of events (as a percentage of the total dataset) that each leaf should represent. This controls how finely separated the data should be.

The second set of parameters relate to the boosting algorithm itself; these are:

- Shrinkage (also called learning rate), this is a weighting applied to each new tree to control how quickly the residuals are corrected.
- Bagging, the number of samples (as a fraction of the total dataset) required to train each tree.
- Number of trees (nTrees), the total number of trees to create (*i.e.* the number of iterations to perform).

Collectively these are known as the *hyperparameters* for a BDT. The hyperparameters were optimised by scanning a range of values for each hyperparameter and testing a BDT for each combination. The final hyperparameters that were used in the analysis are listed in Table 5.4.

| Rank | Variable | Category | Description | IR |
|---|---|---|---|---|
| 1 | $\Sigma w_{\mathrm{MV2c10}}$ | b-tagging | Sum of MV2c10 pseudo-continuous b-tagging score over all jets | ✓ |
| 2 | $p_{\mathrm{T}}^{\ell_0}$ | Lepton | Transverse momentum of leading lepton | ✓ |
| 3 | $E_{\mathrm{T}}^{\mathrm{miss}}$ | Energy | Missing transverse energy | ✓ |
| 4 | $\Delta R(\ell,\ell)_{\mathrm{min}}$ | Distance | The minimum distance between any lepton pair | ✓ |
| 5 | $p_{\mathrm{T}}^{jet_5}$ | Jet | Transverse momentum of 6th leading jet | ✓ |
| 6 | $\Delta R(\ell,b)_{\mathrm{max}}$ | Distance | The maximum distance between leptons and b-tagged jets | ✓ |
| 7 | $H_{\mathrm{T}}^{\mathrm{no\ lead\ jet}}$ | Energy | Scalar sum of all lepton and jet pT except leading jet | ✓ |
| 8 | $\Sigma\Delta R(\ell,\ell)_{\mathrm{min}}$ | Distance | Sum of the distance between leading and sub-leading leptons in SS or leading, sub-leading and third-leading leptons in $3\ell$ | ✓ |
| 9 | $m_{jet}/pTjet$ | Event | Jet mass divided by pT for the highest ratio | ✓ |
| 10 | $\Delta\phi(\ell_0, j_0)$ | Distance | The transverse angle between leading lepton and jet | |
| 11 | $p_{\mathrm{T}}^{jet_0}$ | Jet | Transverse momentum of leading jet | ✓ |
| 12 | $\Delta R(j,b)_{\mathrm{min}}$ | Distance | The minimum distance between b-tagged jets and jets | ✓ |
| 13 | $\Delta R(\ell,j)_{\mathrm{min}}$ | Distance | The minimum distance between leptons and jets | |
| 14 | $p_{\mathrm{T}}^{b-jet_0}$ | Jet | Transverse momentum of leading b-tagged jet | ✓ |
| 15 | $\Delta R(\ell,b)_{\mathrm{min}}$ | Distance | The minimum distance between leptons and b-tagged jets | |
| 16 | $p_{\mathrm{T}}^{\ell_1}$ | Jet | Transverse momentum of sub-leading lepton | |
| 17 | $p_{\mathrm{T}}^{jet_2}$ | Jet | Transverse momentum of third-leading jet | |
| 18 | $p_{\mathrm{T}}^{jet_1}$ | Jet | Transverse momentum of sub-leading jet | ✓ |
| 19 | nJets | Jet | Number of jets | ✓ |
| 20 | nleps | Lepton | Number of leptons | |
| 21 | $p_{\mathrm{T}}^{\ell_2}$ | Lepton | Transverse momentum of third-leading lepton | |

Table 5.5: The initial set of variables used during the optimization studies. Rank is a measure of the importance of a variable and is based off of a ranking score reported by TMVA. Variables retained after the Iterative Removal procedure are marked by a '✓' in the last column.

### 5.8.3 Variable Selection

The input variables for the BDT were determined using the Iterative Removal method. In this method, the BDT is repeatedly retrained and tested after the removal of a single input variable. If the performance of the BDT remains unchanged (up to some threshold) from the baseline BDT after the removal of a variable, that variable is excluded from future iterations. Otherwise, that variable is returned to the variable list and a different variable is removed for the next iteration. With this method, a list of 14 input variables was obtained from an initial list of 21 candidate variables. These variables are listed in Table 5.5.

| Region | Channel | nJets | nBjets | Other Selections | Fitted variable |
|---|---|---|---|---|---|
| SR | SS+3$\ell$ | $\geq 6$ | $\geq 2$ | $H_T > 500$ | BDT |
| VRttZ3$\ell$ | 3$\ell$ (no Z-veto) | $\geq 6$ | $\geq 2$ | $H_T > 500$ | BDT |
| CRttbarCO | SSee‖SSem | $4 \leq$nJets$\leq 6$ | $\geq 1$ | $0 < M_{ee}$@$ConvV < 0.1$<br>$200 < H_T < 500$ | $M_{ee}$@$PV$ |
| CR1b3$\ell$e | eee‖eem | - | $= 1$ | $100 < H_T < 250$ | lead el $p_{\mathrm{T}}$ |
| CR1b3$\ell$m | emm‖mmm | - | $= 1$ | $100 < H_T < 250$ | lead $\mu$ $p_{\mathrm{T}}$ |
| CRttW2$\ell$ | SSem‖SSmm | $\geq 4$ | $\geq 2$ | $M_{ee} < 0$ or $M_{ee} > 0.1$, $\lvert\eta(e)\rvert < 1.5$<br>for nBjets $= 2$, $H_T > 500$ or nJets $< 6$<br>for nBjets $\geq 3$, $H_T < 500$ | sum lepton $p_{\mathrm{T}}$ |
| CRlowBDT | SS+3$\ell$ | $\geq 6$ | $\geq 2$ | $H_T > 500$, BDT $< 0.0$ | BDT |

Table 5.6: Final region definitions for the SSML template fit method.

## 5.9 Final Region Definitions

The final region configuration used for the template fit method consisted of five control regions, a single validation region, and a single signal region. The control regions were:

- CRttbarCO, for constraining the normalisation of the $\gamma$-conversion and material conversion backgrounds;
- CR1b3le, for constraining the normalisation of events with one electron originating from heavy flavour decays;
- CR1b3lm, for constraining the normalisation of events with one muon originating from heavy flavour decays;
- CRttW2l, for constraining the normalisation of $t\bar{t}W$ events;
- CRlowBDT, which has identical selections to the signal region except for a reversed cut on the BDT discriminant. This was intended to provide a kinematically close region to the signal region for the fit, but no significant constraints were obtained from this region.

The validation region, VRttZ3l, was used to check the normalisation and modelling of the $t\bar{t}Z$ background. An additional validation region for the problematic $t\bar{t}W$ background was used, but it was not part of the template fit method. A summary of the definitions for the regions used in the template fit method, including the signal region, is given in Table 5.6.

## 5.10 Results

As the analysis is still ongoing as of the writing of this thesis, the main signal region remains blinded. However, preliminary results are available from performing the fit

| Process | Expected yield |
|---|---|
| $t\bar{t}t\bar{t}$ | 24.3 ± 9.4 |
| $t\bar{t}W$ | 29.9 ± 7.1 |
| $t\bar{t}WW$ | 3.2 ± 1.6 |
| $t\bar{t}Z$ | 13.2 ± 2.8 |
| $t\bar{t}H$ | 12.3 ± 2.9 |
| QmisID | 3.6 ± 0.5 |
| Mat CO | 5.9 ± 2.2 |
| $\gamma^*$ | 1.3 ± 0.7 |
| HFe | 2.0 ± 1.2 |
| HFm | 2.8 ± 1.4 |
| LF | 0.7 ± 0.8 |
| other fake | 2.0 ± 0.8 |
| t($\bar{t}$)X | 1.3 ± 0.4 |
| VV | 0.3 ± 0.2 |
| V+jets | 0.03 ± 0.01 |
| others | 2.2 ± 1.1 |
| Total | 105.2 ± 8.7 |

Table 5.7: Expected signal and background yields in the SSML signal region.

using data in control regions only, then injecting the extracted normalisation factors into the full model which includes the (blinded) signal region. The expected signal yield and estimated background yields are shown in Table 5.7. Figures 5.13 and 5.14 (respectively) show the normalisation factors and correlation matrix from the control region only fit. Figure 5.15 shows the distribution of the BDT discriminant for the expected signal and background events within the signal region. The expected significance from this analysis is 3.0 standard deviations above the background-only hypothesis (3.7$\sigma$ without systematic uncertainties).

The four most impactful systematics are `b-tagging MV2c10 Light0`, `ttW truth gbb`, `ttW modelling (generator)` and `tttt modelling (shower)`. The $b$-tagging systematic is related to uncertainties in separating light jets from $b$-jets, and is well justified as the dominant uncertainty as we have made use of $b$-jet selections in all of our regions. The remaining three systematics deal with uncertainties in modelling $t\bar{t}W$ and $t\bar{t}t\bar{t}$ processes, specifically with regards to the production of additional $b$-jets from gluon radiation. The $t\bar{t}W$ process is already known to be difficult to model, and $t\bar{t}t\bar{t}$ showering is not well understood, especially given our high jet multiplicity selection in the signal region.

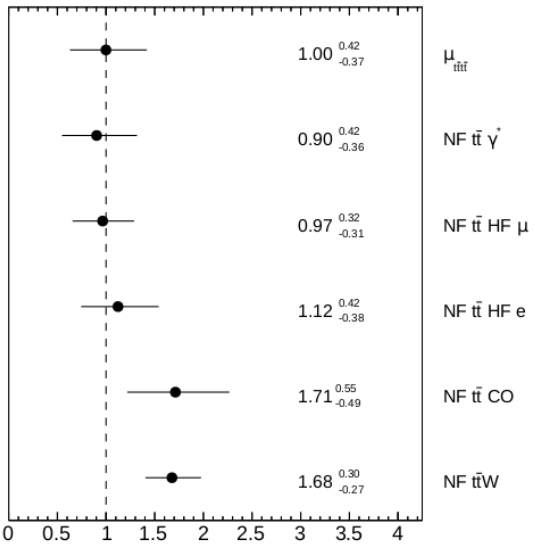


Figure 5.13: Fitted normalisation factors from the control region only fit. The $x$-axis shows the value of the normalisation factor. The NFs for material conversions and $t\bar{t}W$ are notably larger than the others, but this is to be expected due to the difficulties in modelling these events and in isolating the conversions background.

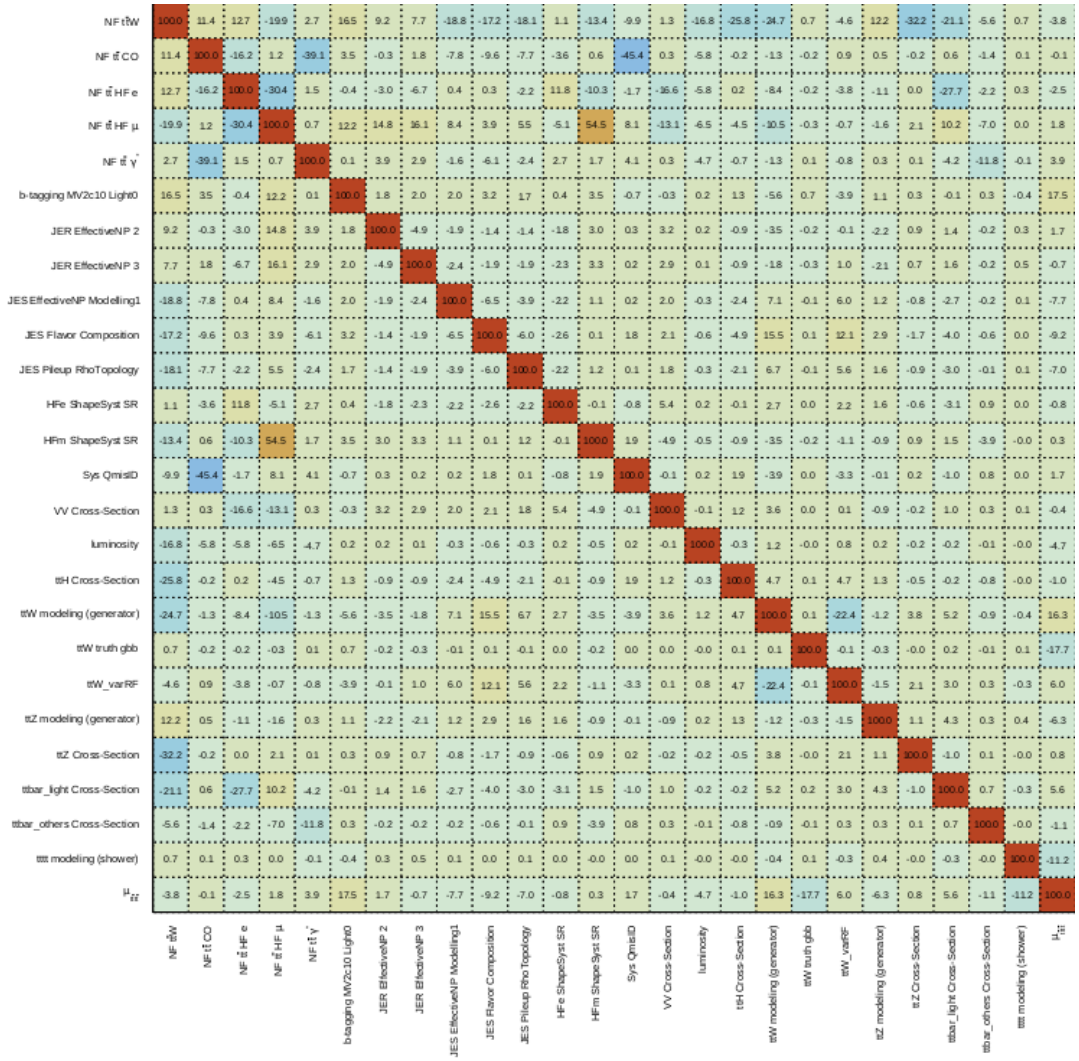


Figure 5.14: Correlation matrix generated from the control region only fit. The principal correlations are between the muon heavy flavour NF and shape systematic, the QmisID systematic and material conversions NF, and the $\gamma^*$ NF and material conversions NF. In general, a normalisation factor and shape systematic for a given background will be correlated when fitting its distribution as they are both used to adjust the distribution. The correlations between QmisID, material conversions, and $\gamma^*$ are understood due to these backgrounds occupying very similar regions of phase space, and no sufficiently discriminating variables between these backgrounds were found.

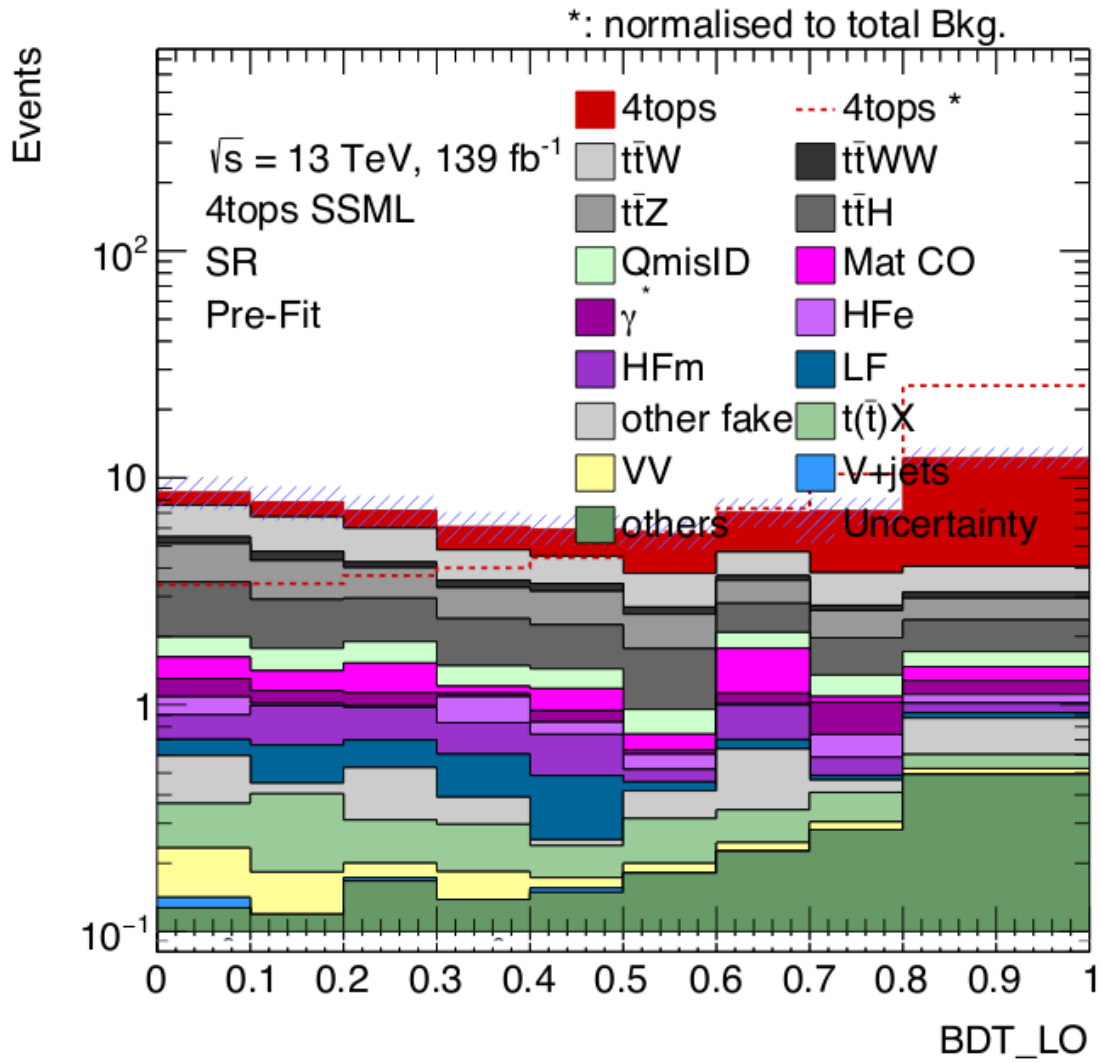


Figure 5.15: Distribution of the BDT discriminant for events within the signal region. This region is blinded, but the normalisations of the backgrounds depicted here are determined using data in the control regions. The dotted line shows the distribution of 4top signal events if its yield is scaled to match the total yield of background events.

Chapter 6

# Conclusions and Future Directions

The coming years will bring many new opportunities in the field of particle physics, but also new challenges. The High Luminosity LHC for instance will give us the opportunity to probe rarer processes if we can cope with the high pile-up environment that will accompany it. The FTK was one such system that was being developed by the ATLAS Collaboration to adapt to the increased pile-up. While the FTK project has been discontinued, the fast simulation software that was developed for it will be used in its successor project, the Hardware Track Trigger. The improved tracking that will be delivered by this system will bring innumerable benefits to physics analyses using ATLAS data through improvements to areas such as triggering and jet tagging.

The analysis of Standard Model production of four top quarks described in this thesis is one such analysis that would benefit greatly from improvements to jet tagging, as the leading systematic error in this analysis pertained to the tagging of $b$-jets. While the analysis remains ongoing as of the writing of this thesis, an expected significance of $2.99\sigma$ above the background-only hypothesis has been obtained from preliminary results. Assuming that evidence for four top production is found in the final analysis, some possible future directions to consider are performing an extraction of the top Yukawa coupling, or obtaining constraints on Effective Field Theory operators [84].

There remains much to be learned about the innermost workings of the universe, but perhaps the upcoming generation of collider experiments will bring us closer to the understanding we desire.

**Appendix A**

# Initial region definitions for the four-top-quark analysis

The following tables give the definitions of the control, validation and signal regions that were in use as of the commencement of my involvement with the four-top-quark analysis.

| CR | Lepton Flags | nJets | Other Selections |
|---|---|---|---|
| 1b3$\ell$ | eee_Zveto ‖ eem_Zveto ‖ emm_Zveto ‖ mmm_Zveto | - | nBTags_MV2c10_77==1 && HT_all>200000 &&HT_all<500000 |
| ttbarCO | SSee_passECIDS ‖ SSem_passECIDS | <6 | HT_all>200000 && HT_all<500000 && el_RadiusCO>-100 && el_RadiusCO<50 |
| ttW | SSee_passECIDS‖ SSem_passECIDS‖SSmm | 2≤nJets<6 | nBTags_MV2c10_77≥2 && HT_all>500000 ‖ nBTags_MV2c10_77≥3 && HT_all<500000 |
| ttZ | (eee&&!eee_Zveto) ‖ (eem&&!eem_Zveto) ‖ (emm&&!emm_Zveto) ‖ (mmm&&!mmm_Zveto) | - | nBTags_MV2c10_77≥2 && HT_all>500000 |

Table A.1: Initial control region definitions.

| VR | Lepton Flags | nJets | Other Selections |
|---|---|---|---|
| 1b2$\ell$ | SSee_passECIDS‖ SSem_passECIDS‖SSmm | ≥6 | nBTags_MV2c10_77==1 && HT_all>500000 |
| 1b3$\ell$ | eee_Zveto‖eem_Zveto‖ emm_Zveto‖mmm_Zveto | ≥6 | nBTags_MV2c10_77==1 && HT_all>500000 |
| 2b2$\ell$ | SSee_passECIDS‖ SSem_passECIDS‖SSmm | ≥6 | nBTags_MV2c10_77==2 && HT_all>200000 && HT_all<500000 |
| 2b3$\ell$ | eee_Zveto‖eem_Zveto‖ emm_Zveto‖mmm_Zveto | - | nBTags_MV2c10_77==2 && (nJets<6 ‖ (HT_all>200000 && HT_all<500000)) |
| 3b2$\ell$ | SSee_passECIDS‖ SSem_passECIDS‖SSmm | ≥6 | nBTags_MV2c10_77≥3 && HT_all>200000 && HT_all<500000 |

Table A.2: Initial validation region definitions.

| SR | Lepton Flags | nJets | Other Selections |
|---|---|---|---|
| 2b2$\ell$ | SSee_passECIDS‖ SSem_passECIDS‖SSmm | ≥6 | nBTags_MV2c10_77==2 && HT_all>500000 |
| 2b3$\ell$ | eee_Zveto‖eem_Zveto‖ emm_Zveto‖mmm_Zveto | ≥6 | nBTags_MV2c10_77==2 && HT_all>500000 |
| 3b2$\ell$ | SSee_passECIDS‖ SSem_passECIDS‖SSmm | ≥6 | nBTags_MV2c10_77==3 && HT_all>500000 |
| 3b3$\ell$ | eee_Zveto‖eem_Zveto‖ emm_Zveto‖mmm_Zveto | ≥6 | nBTags_MV2c10_77==3 && HT_all>500000 |
| 4b | SSee_passECIDS‖ SSem_passECIDS‖SSmm‖ eee_Zveto‖eem_Zveto‖ emm_Zveto‖mmm_Zveto | ≥6 | nBTags_MV2c10_77≥4 && HT_all>500000 |

Table A.3: Initial signal region definitions.

Appendix B

# Additional figures for four-top-quark analysis control region studies

The following figures compare the correlation matrices generated after fitting using different variations on the initial region configuration. See Section 5.6.1 for a description of these variations. One of the goals of testing these variations was to find a configuration that minimised the correlations between different systematics (the off-diagonal entries in the matrices). Figure B.1 compares the original configuration to the improved baseline version. Figures B.2 to B.6 show the correlation matrices for the versions in the "Combined" set of variations.

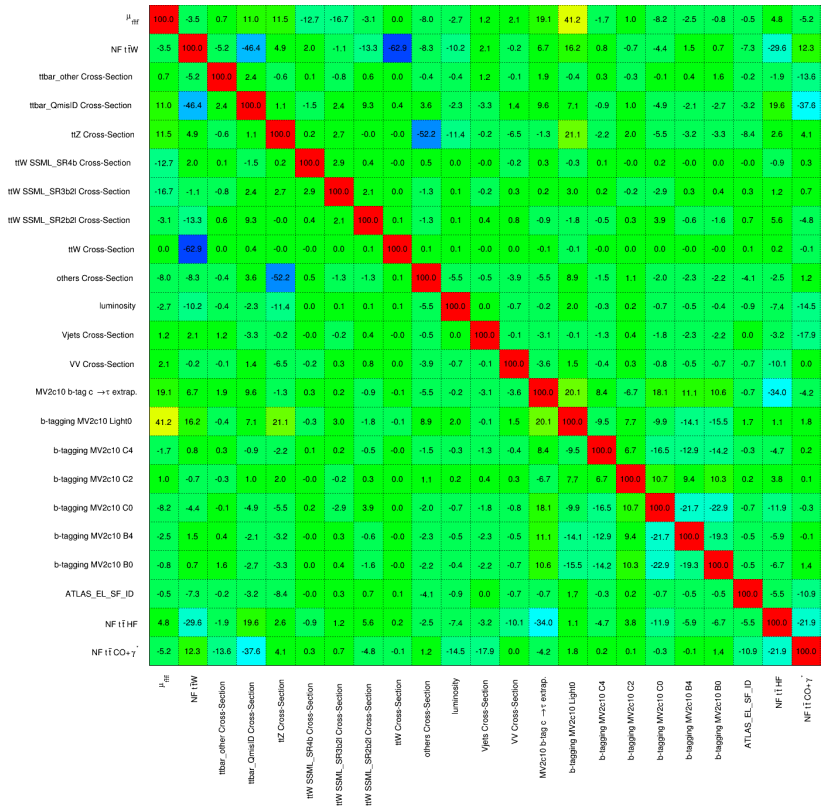


(a)

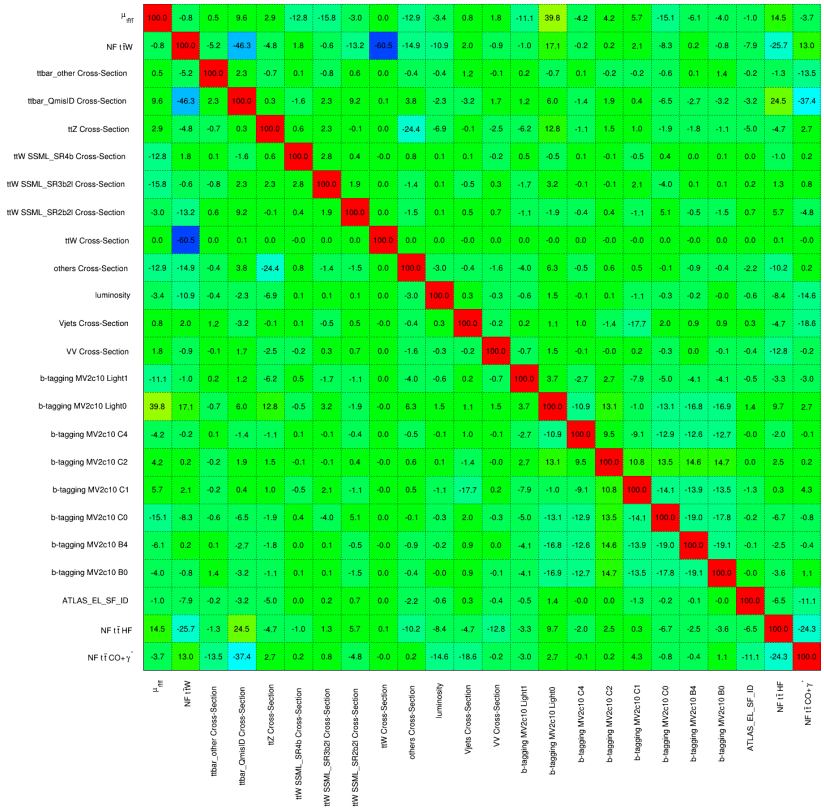


(b)

Figure B.1: A comparison of correlation matrices between the original configuration (Subfigure B.1a) and the improved baseline configuration (Subfigure B.1b).

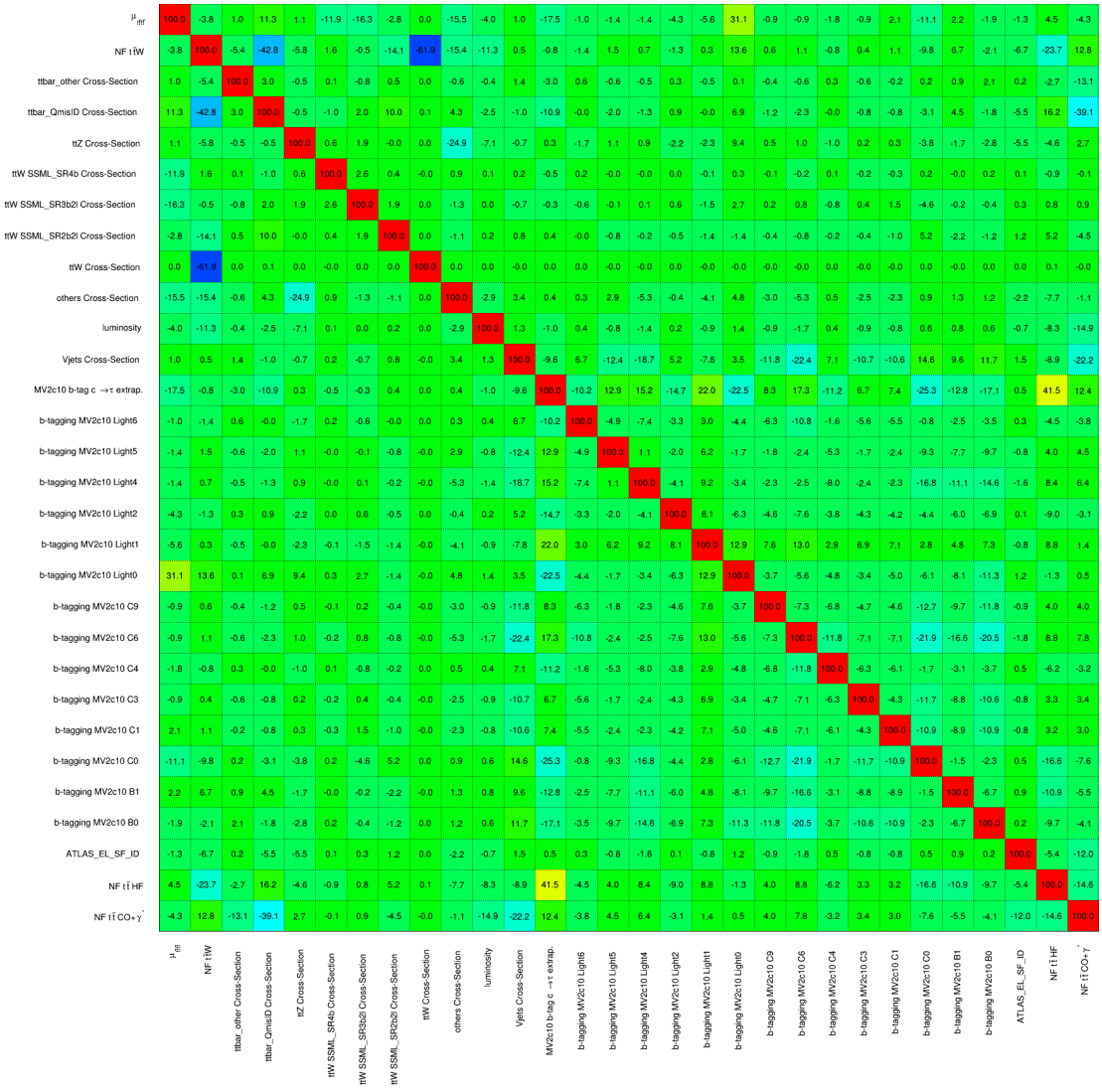


Figure B.2: Correlation matrix for a configuration from the "Combined" set of variations where the signal regions have been split by flavour.

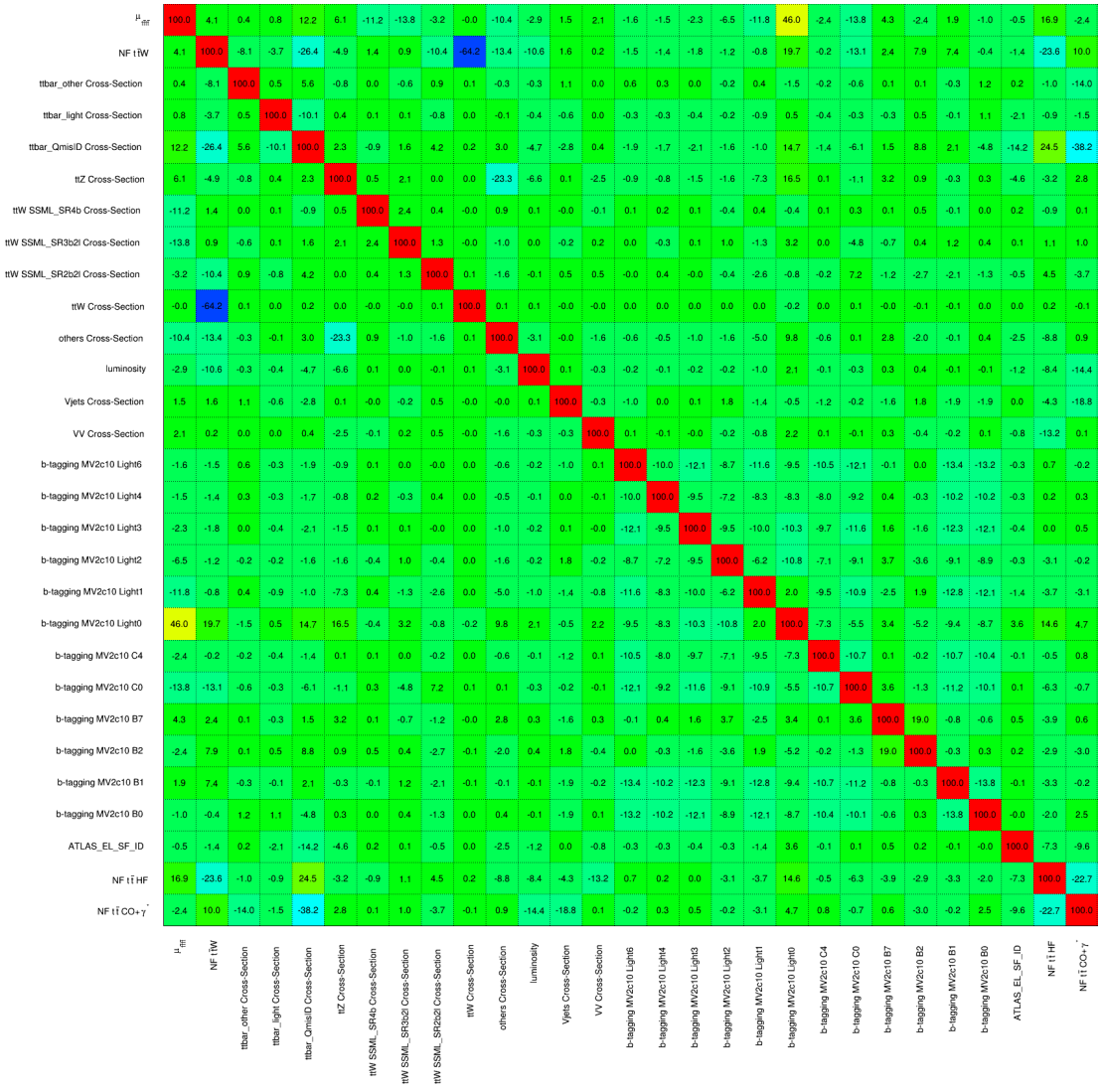


Figure B.3: Correlation matrix for a configuration from the "Combined" set of variations where the $t\bar{t}W$ region has been split by flavour.

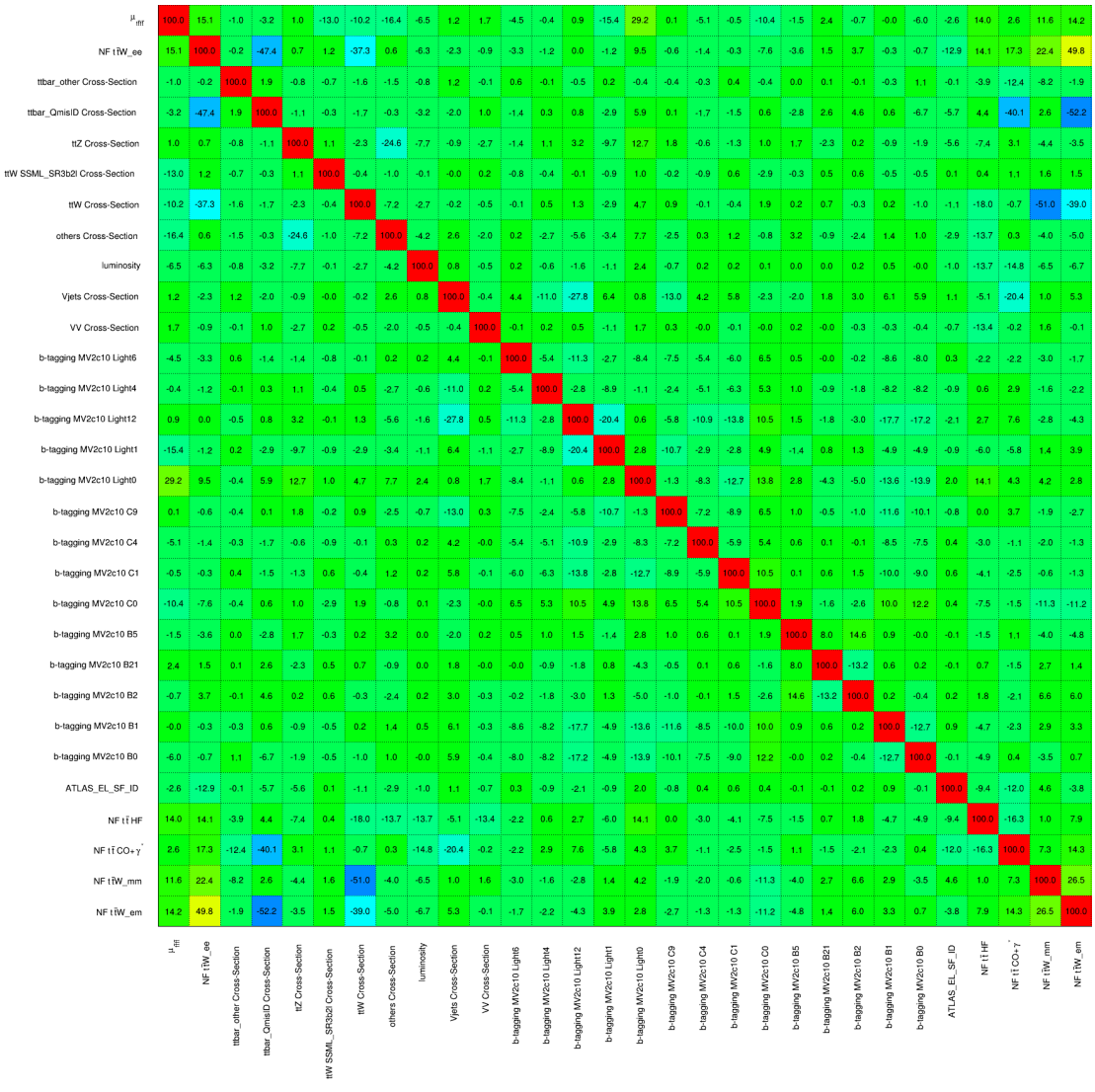


Figure B.4: Correlation matrix for a configuration from the "Combined" set of variations where both the $t\bar{t}W$ region and the control regions have been split by flavour.

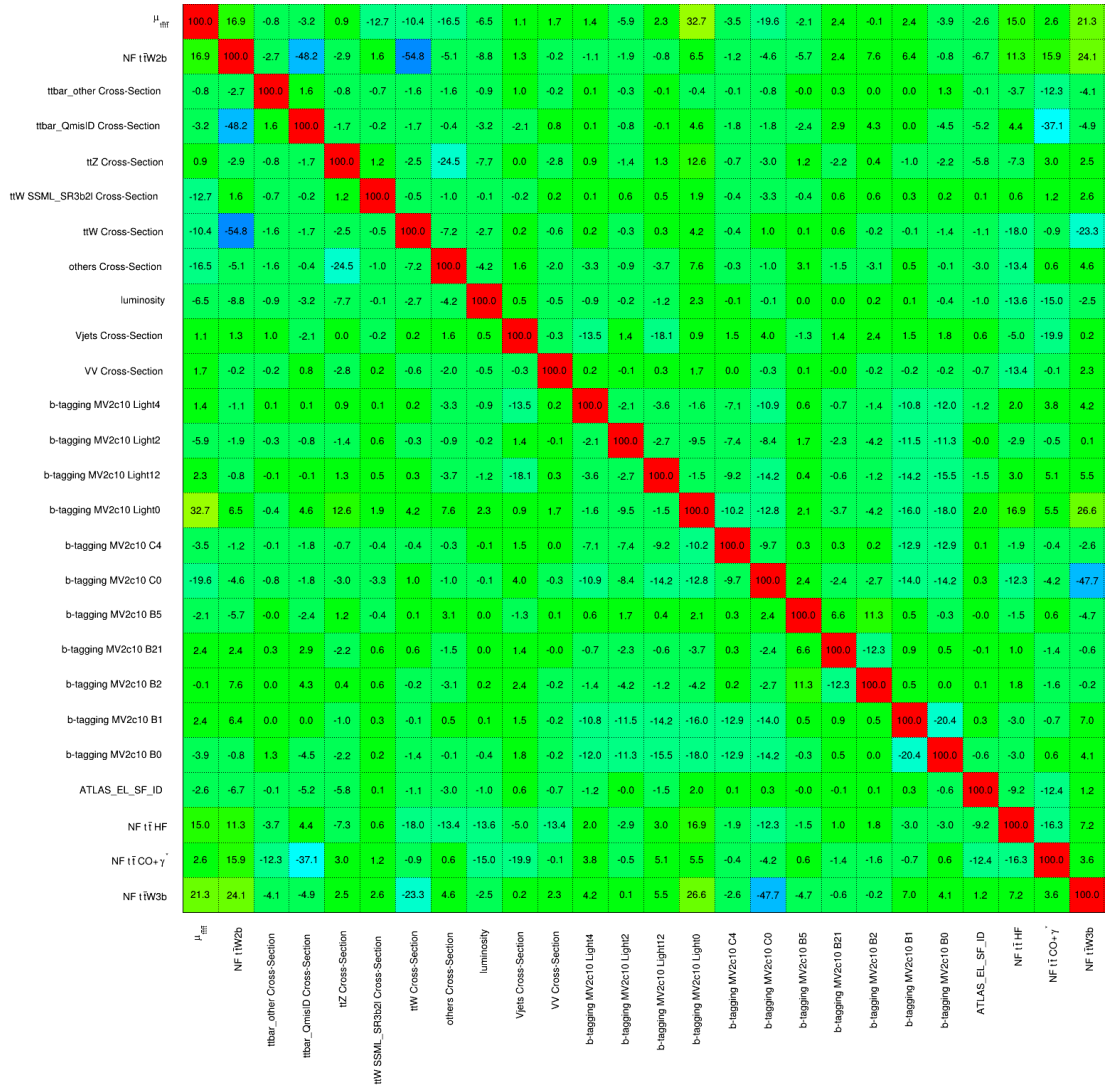


Figure B.5: Correlation matrix for a configuration from the "Combined" set of variations where the $t\bar{t}W$ region has been split by number of $b$-jets and the signal regions have been split by flavour.

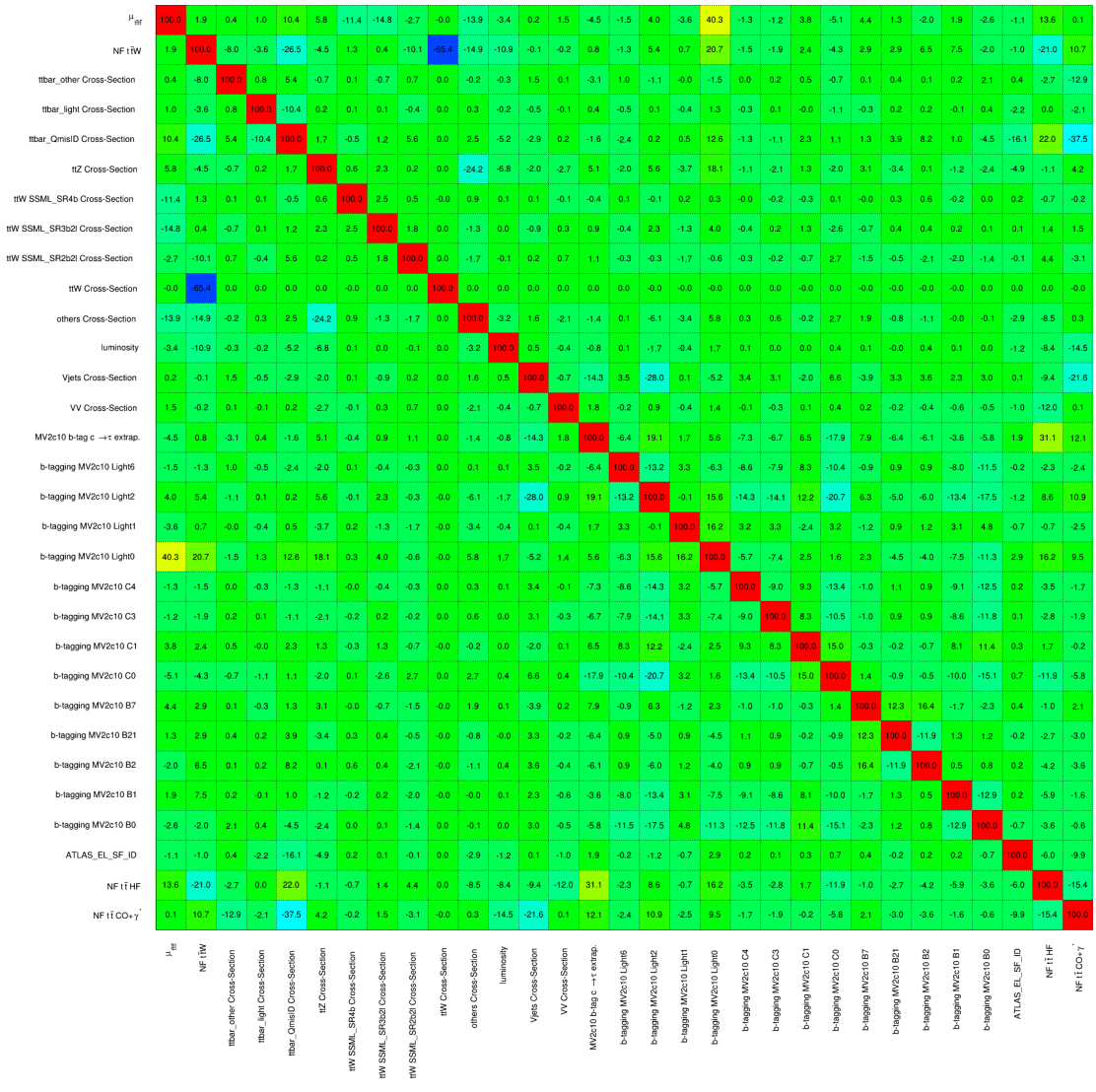


Figure B.6: Correlation matrix for a configuration from the "Combined" set of variations where the $t\bar{t}W$ region has been split by both flavour and number of $b$-jets, and the signak regions have been split by flavour.

Appendix C

# Additional figures for anomaly investigation in the four-top-quark analysis

The following figures show the distributions of the total number of jets, lepton $\eta$, lepton $p_{\mathrm{T}}$ and lepton flavour composition for events within the 2b3l validation region. Compared to the figures shown in Section 5.6.2, the events further are split over data taking period in addition to lepton flavour category. The intent of these figures was to identify features characteristic of the events constituting the data excess that was found in the 2b3l region, in the hope that this would lead to an understanding of why this excess was present.

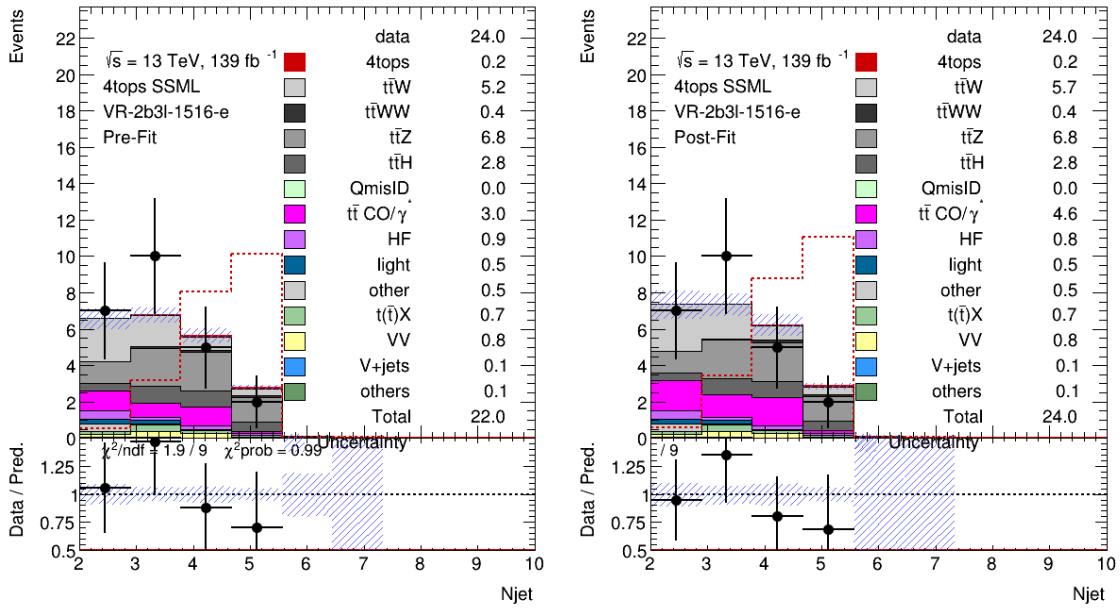


(a) $eee + eem$ events, pre-fit




(b) $eee + eem$ events, post-fit

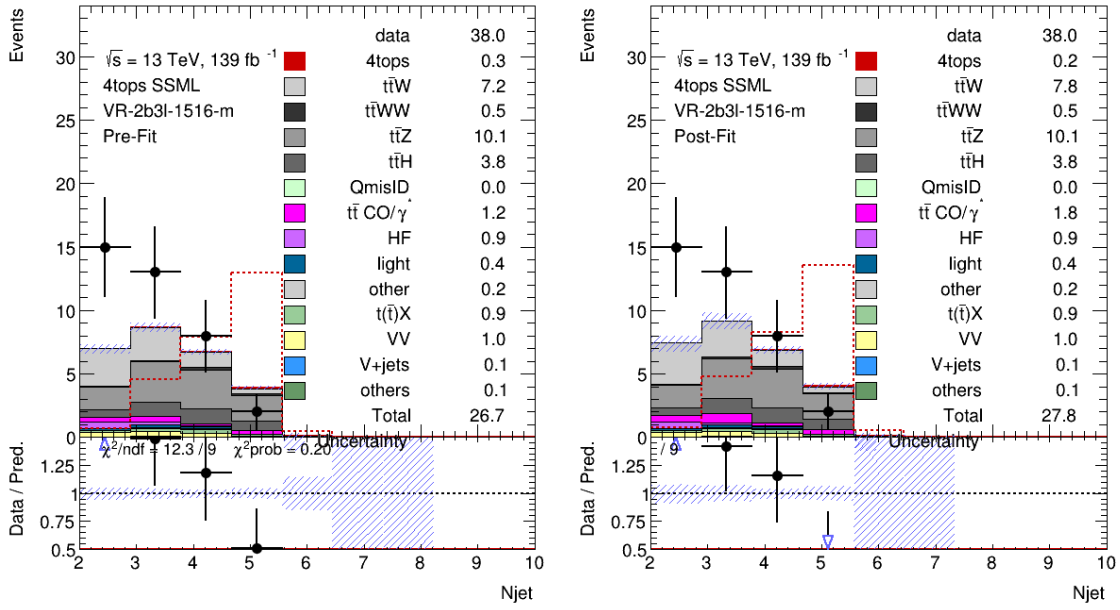


(c) $emm + mmm$ events, pre-fit




(d) $emm + mmm$ events, post-fit

Figure C.1: Flavour category split of the 2b3l validation region for the 2015-2016 data taking period, showing the distribution of the Njets variable.

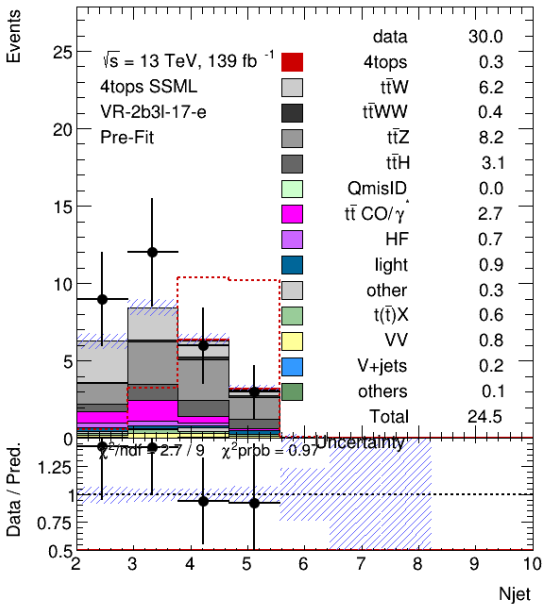


(a) $eee + eem$ events, pre-fit

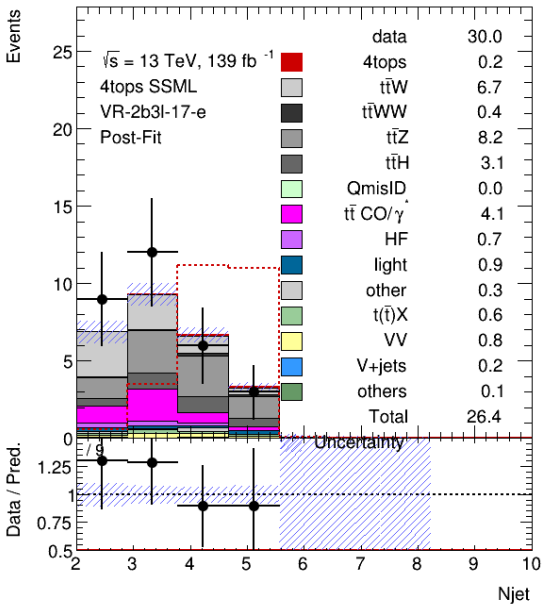


(b) $eee + eem$ events, post-fit

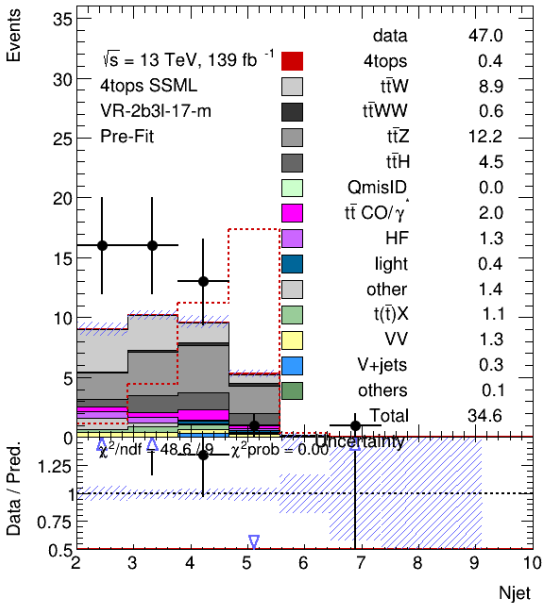


(c) $emm + mmm$ events, pre-fit

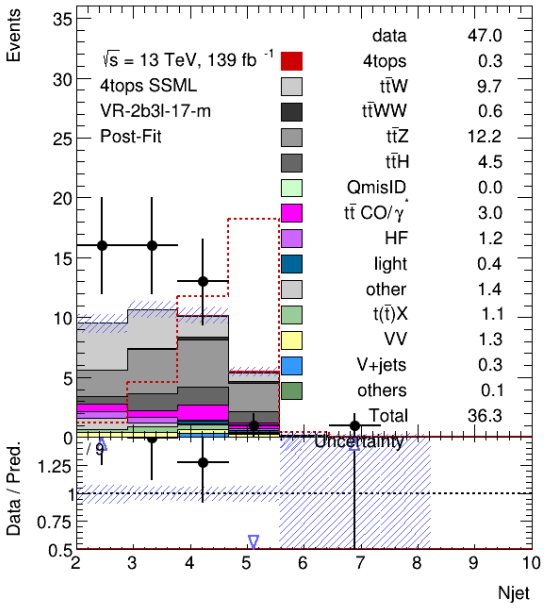


(d) $emm + mmm$ events, post-fit

Figure C.2: Flavour category split of the 2b3l validation region for the 2017 data taking period, showing the distribution of the Njets variable.

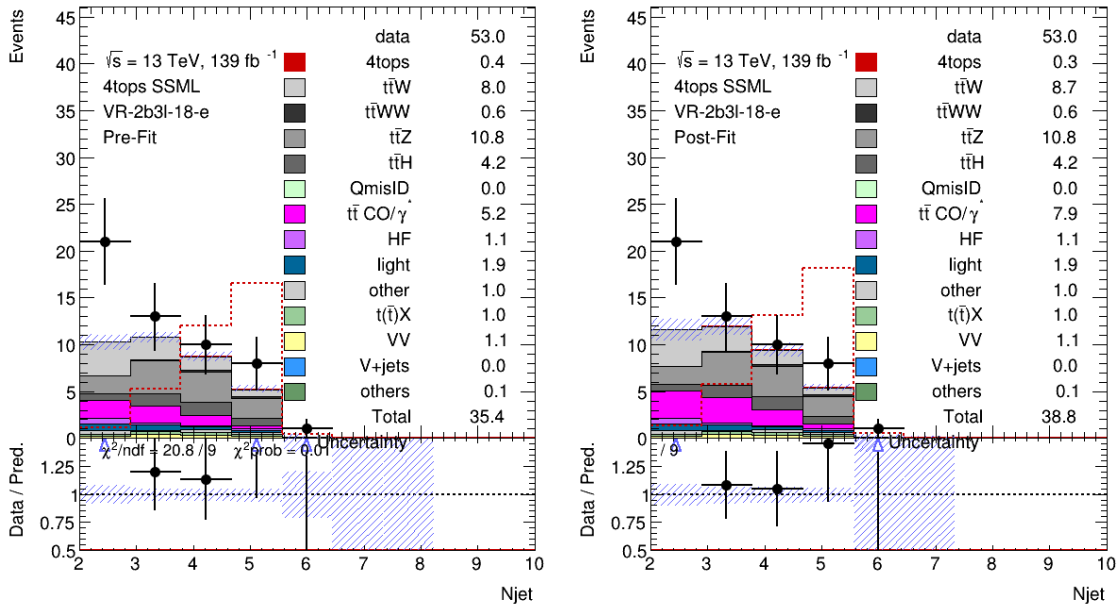


(a) $eee + eem$ events, pre-fit

(b) $eee + eem$ events, post-fit

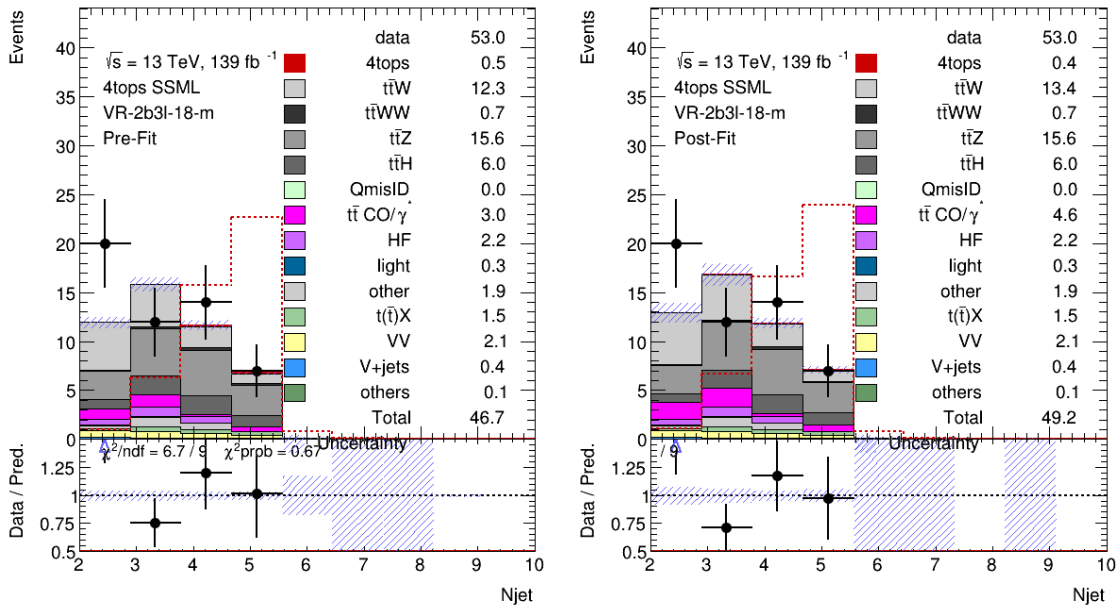


(c) $emm + mmm$ events, pre-fit

(d) $emm + mmm$ events, post-fit

Figure C.3: Flavour category split of the 2b3l validation region for the 2018 data taking period, showing the distribution of the Njets variable.

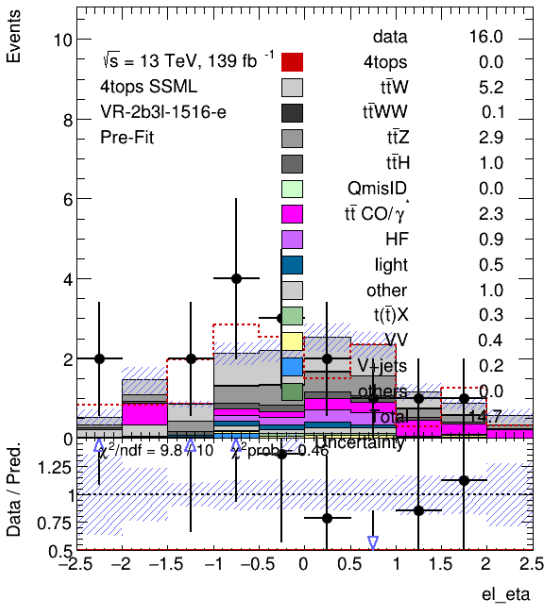


(a) $eee + eem$ events, pre-fit

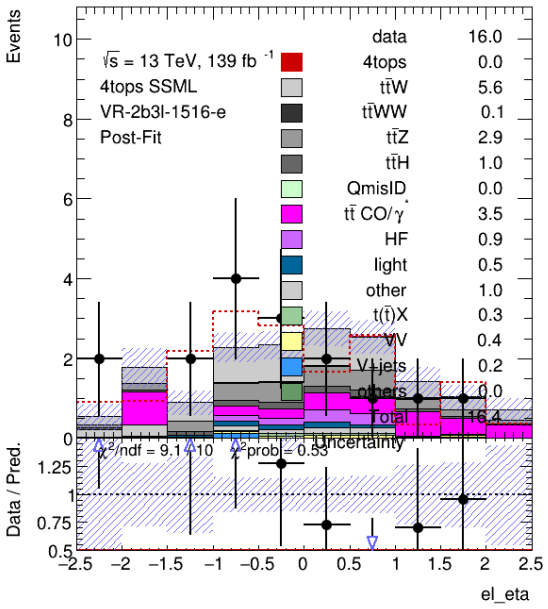


(b) $eee + eem$ events, post-fit

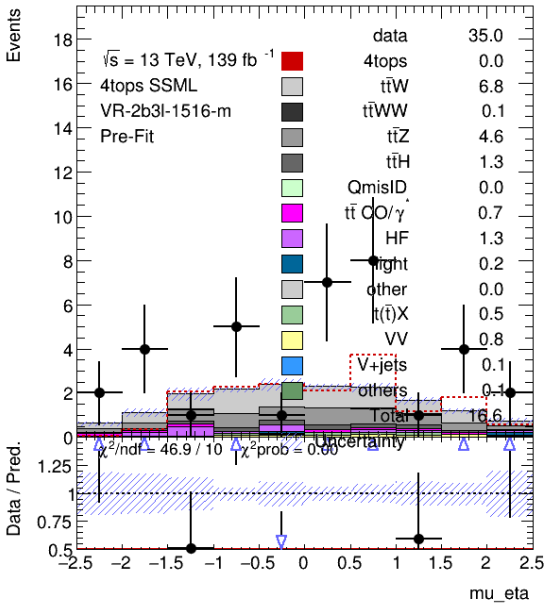


(c) $emm + mmm$ events, pre-fit

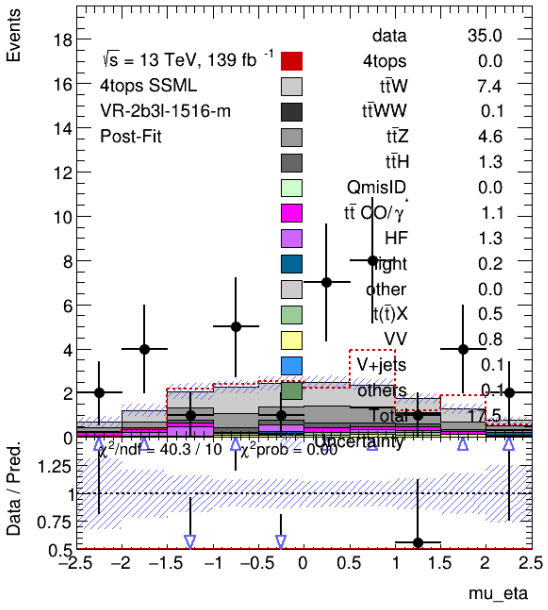


(d) $emm + mmm$ events, post-fit

Figure C.4: Flavour category split of the 2b3l validation region for the 2015-2016 data taking period, showing the distribution of the $\eta$ variable.

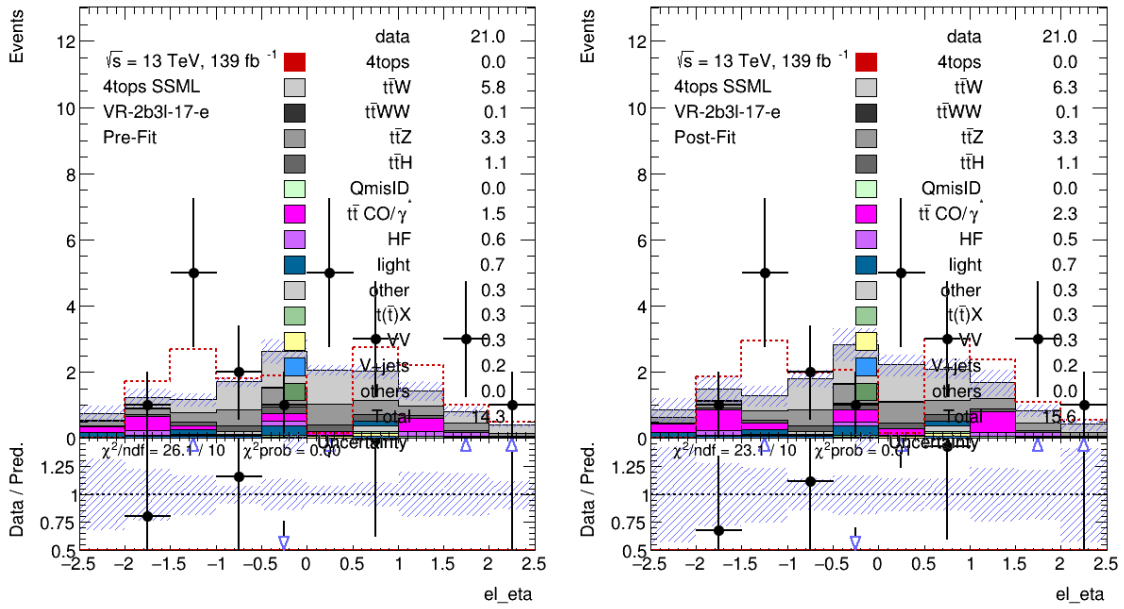


(a) *eee* + *eem* events, pre-fit

(b) *eee* + *eem* events, post-fit

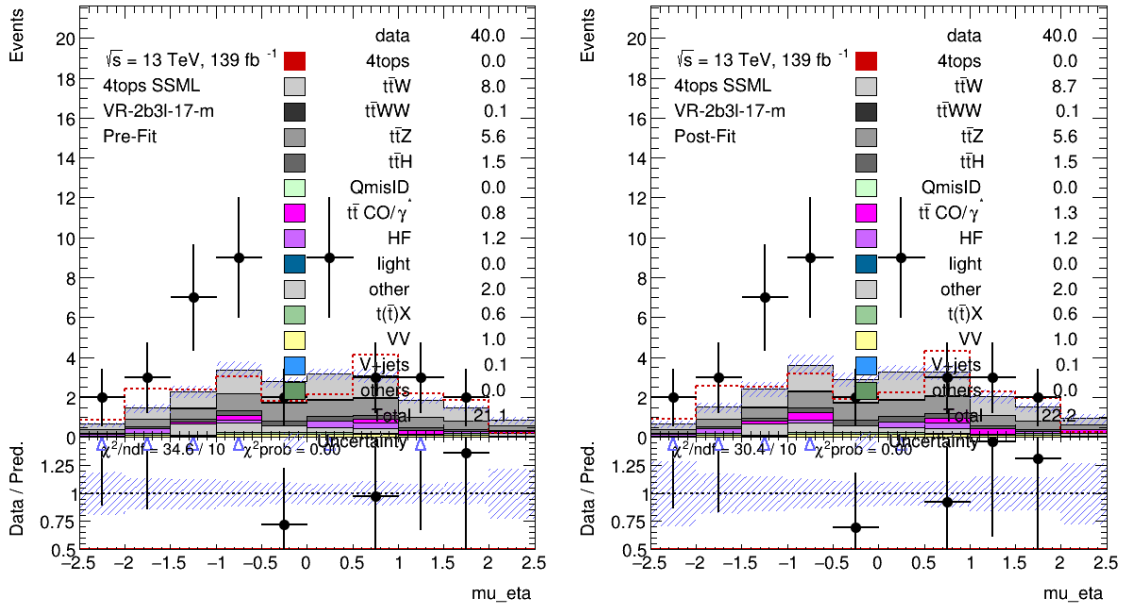


(c) *emm* + *mmm* events, pre-fit

(d) *emm* + *mmm* events, post-fit

Figure C.5: Flavour category split of the 2b3l validation region for the 2017 data taking period, showing the distribution of the $\eta$ variable.

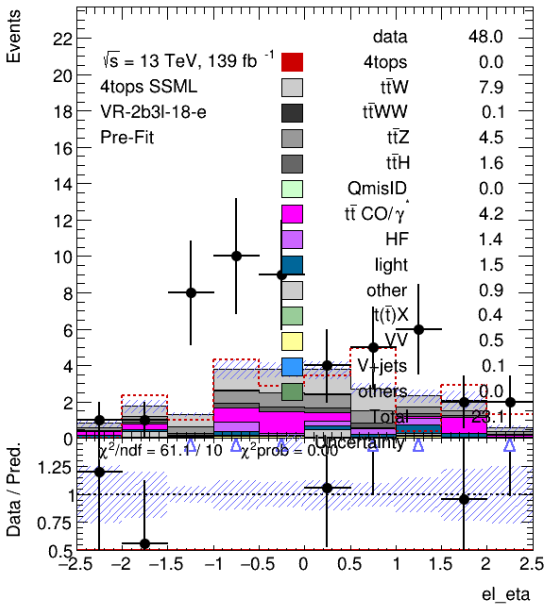


(a) $eee + eem$ events, pre-fit

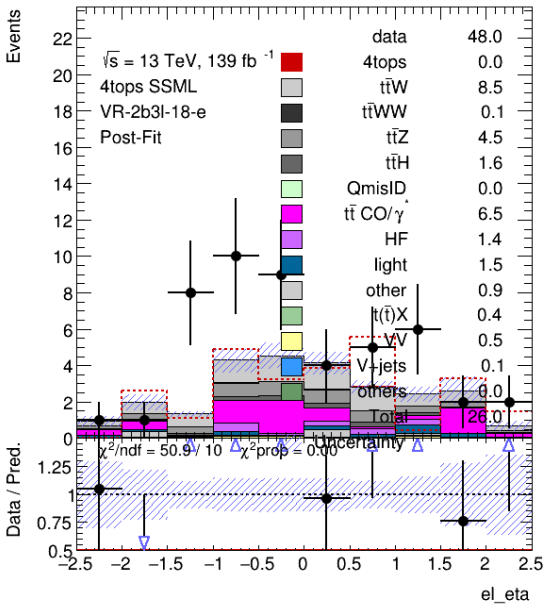


(b) $eee + eem$ events, post-fit

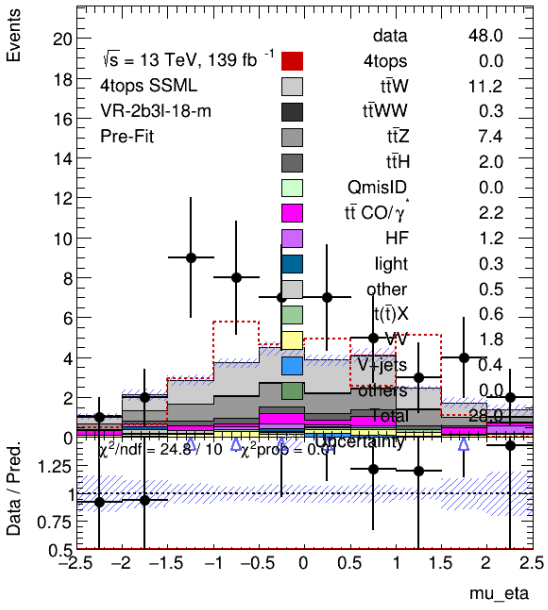


(c) $emm + mmm$ events, pre-fit

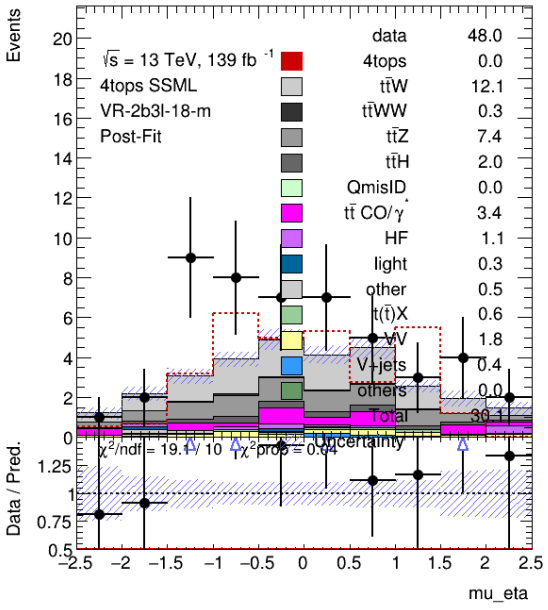


(d) $emm + mmm$ events, post-fit

Figure C.6: Flavour category split of the 2b3l validation region for the 2018 data taking period, showing the distribution of the $\eta$ variable.

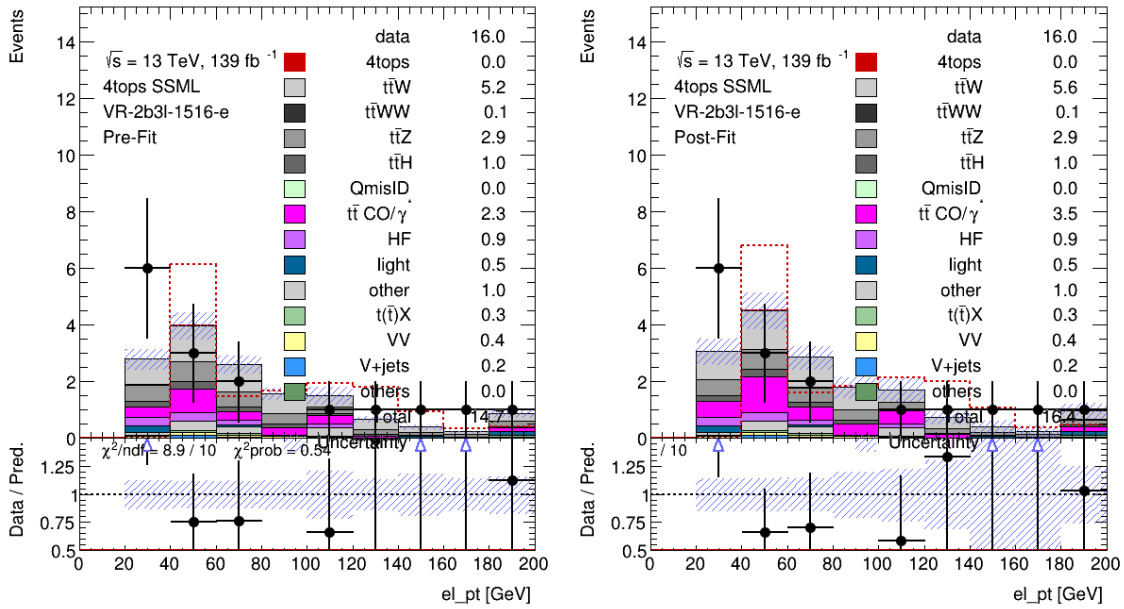


(a) $eee + eem$ events, pre-fit

(b) $eee + eem$ events, post-fit

(c) $emm + mmm$ events, pre-fit

(d) $emm + mmm$ events, post-fit

Figure C.7: Flavour category split of the 2b3l validation region for the 2015-2016 data taking period, showing the distribution of the $p_{\mathrm{T}}$ variable.

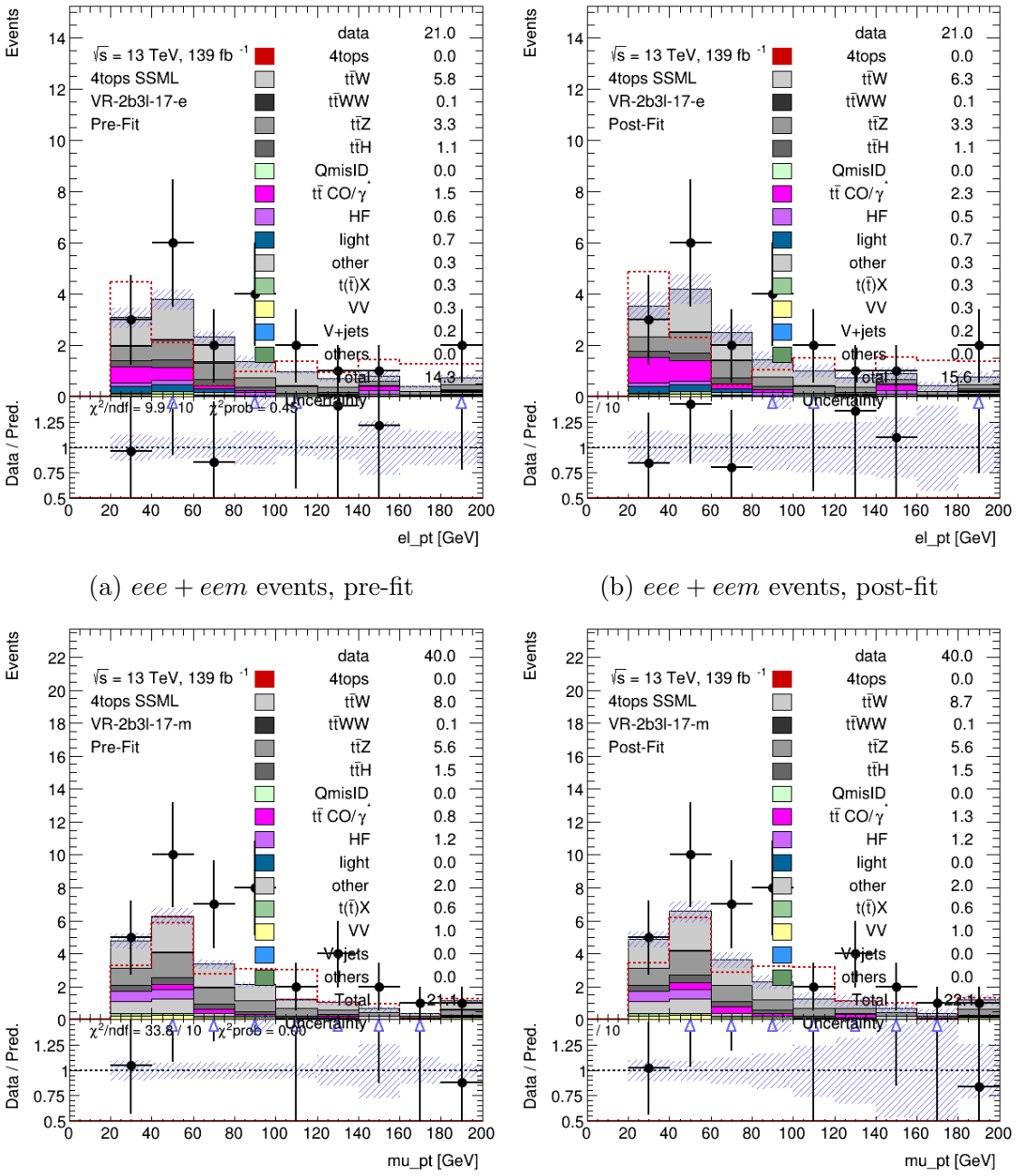


(a) $eee + eem$ events, pre-fit

(b) $eee + eem$ events, post-fit

(c) $emm + mmm$ events, pre-fit

(d) $emm + mmm$ events, post-fit

Figure C.8: Flavour category split of the 2b3l validation region for the 2017 data taking period, showing the distribution of the $p_{\mathrm{T}}$ variable.

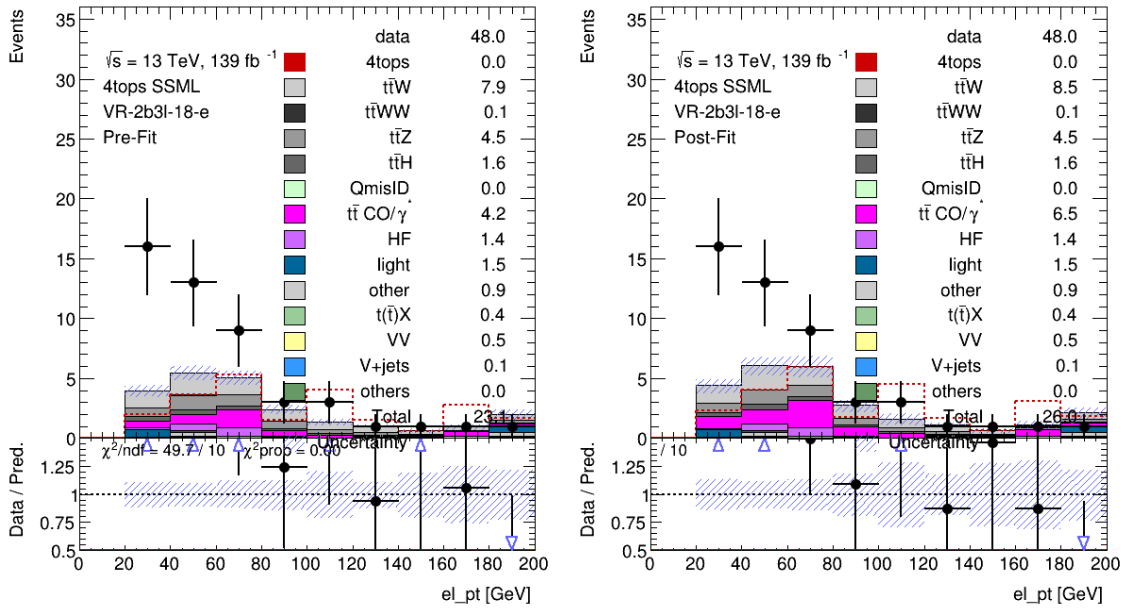


(a) $eee + eem$ events, pre-fit

(b) $eee + eem$ events, post-fit

(c) $emm + mmm$ events, pre-fit

(d) $emm + mmm$ events, post-fit

Figure C.9: Flavour category split of the 2b3l validation region for the 2018 data taking period, showing the distribution of the $p_{\mathrm{T}}$ variable.

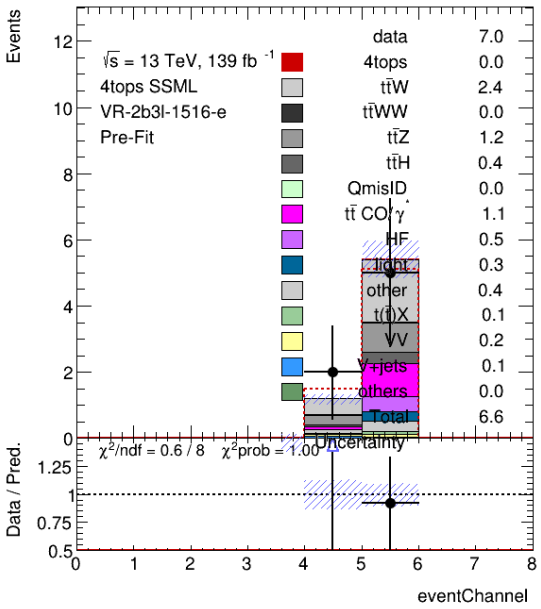


(a) $eee + eem$ events, pre-fit

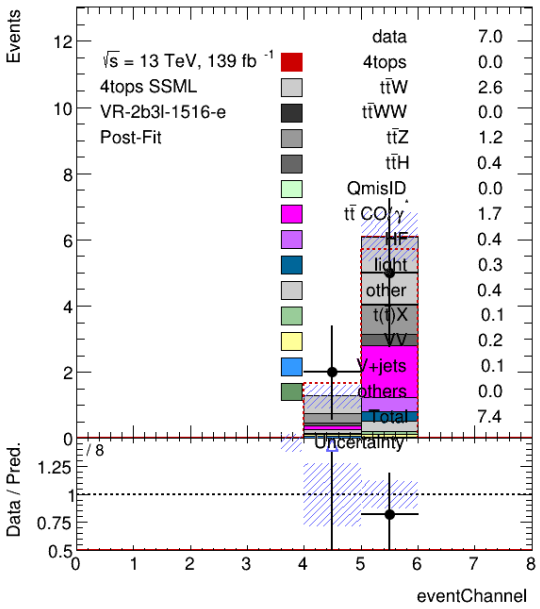


(b) $eee + eem$ events, post-fit

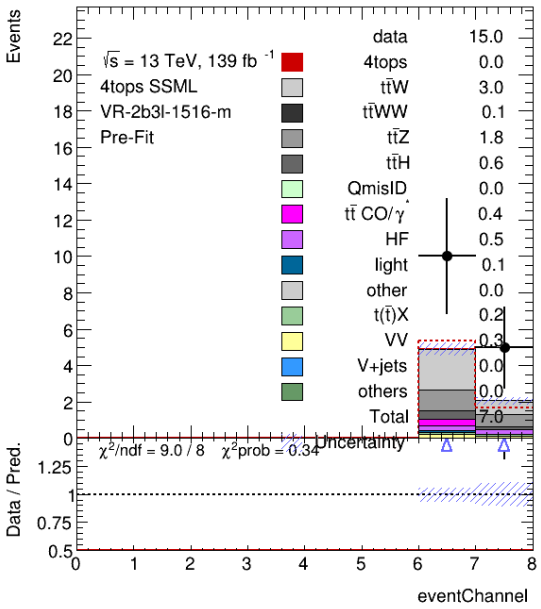


(c) $emm + mmm$ events, pre-fit

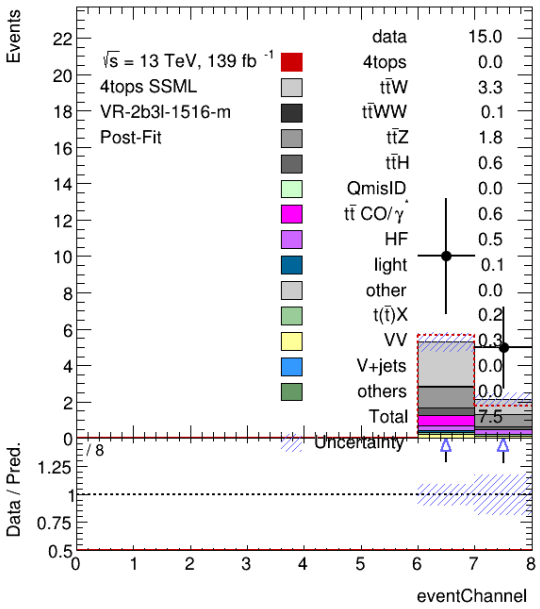


(d) $emm + mmm$ events, post-fit

Figure C.10: Flavour category split of the 2b3l validation region for the 2015-2016 data taking period, showing the distribution of lepton flavour combinations within each category. Here a value of 4 represents $eee$ events, 5 for $eem$, 6 for $emm$, and 7 for $mmm$ events.

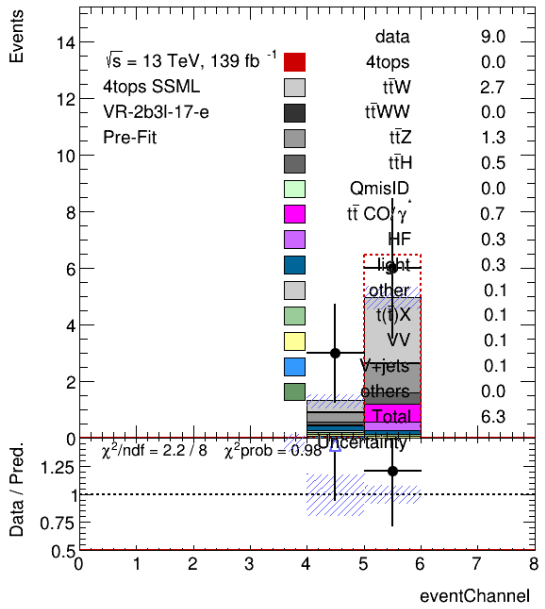


(a) *eee* + *eem* events, pre-fit

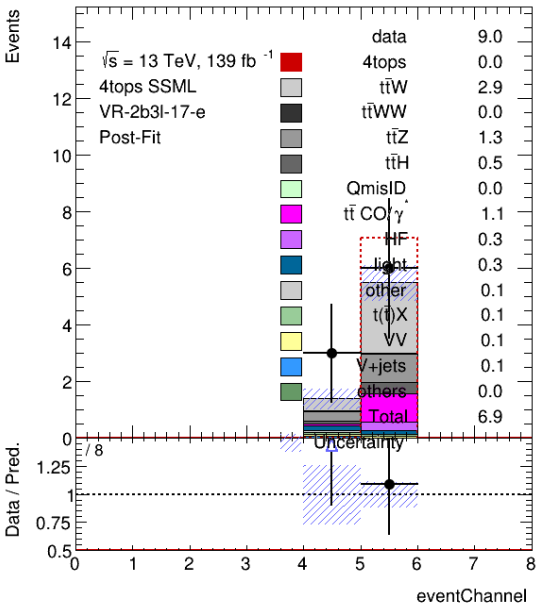


(b) *eee* + *eem* events, post-fit

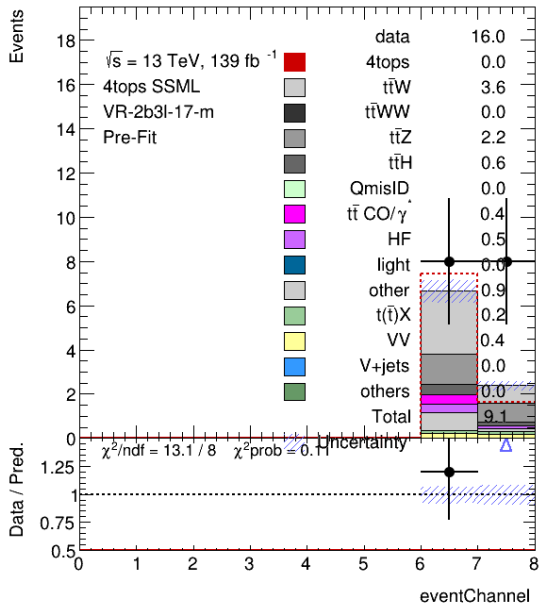


(c) *emm* + *mmm* events, pre-fit

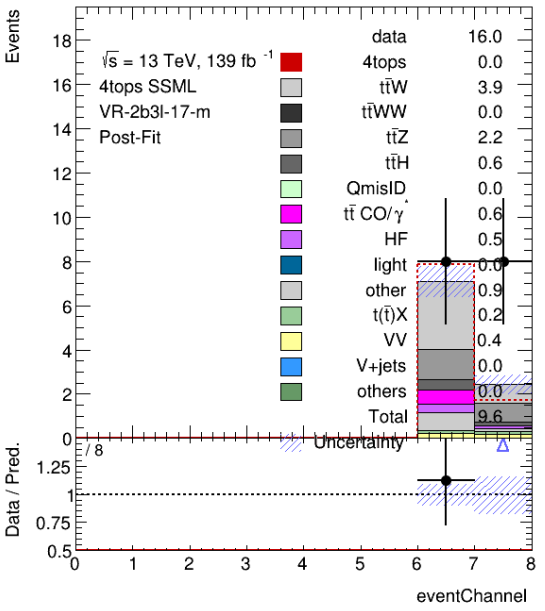


(d) *emm* + *mmm* events, post-fit

Figure C.11: Flavour category split of the 2b3l validation region for the 2017 data taking period, showing the distribution of lepton flavour combinations within each category. Here a value of 4 represents *eee* events, 5 for *eem*, 6 for *emm*, and 7 for *mmm* events.

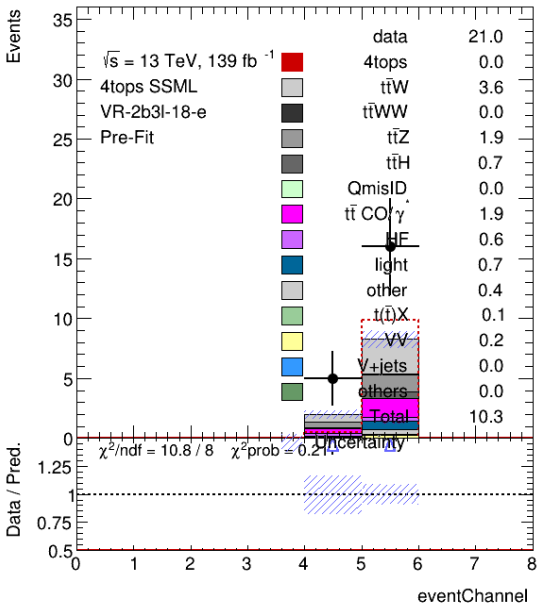


(a) $eee + eem$ events, pre-fit

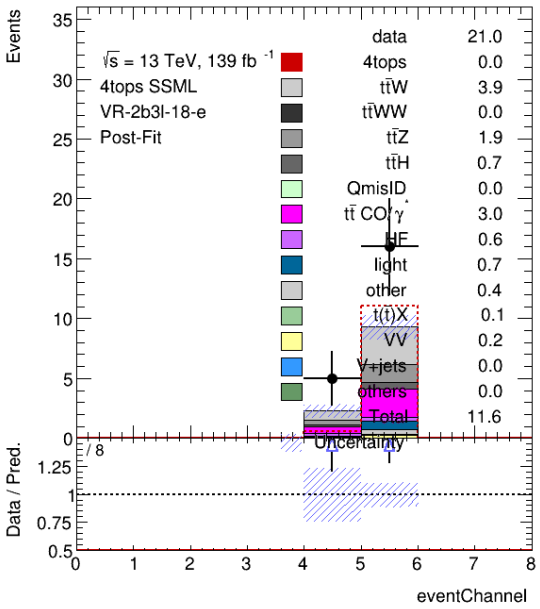


(b) $eee + eem$ events, post-fit

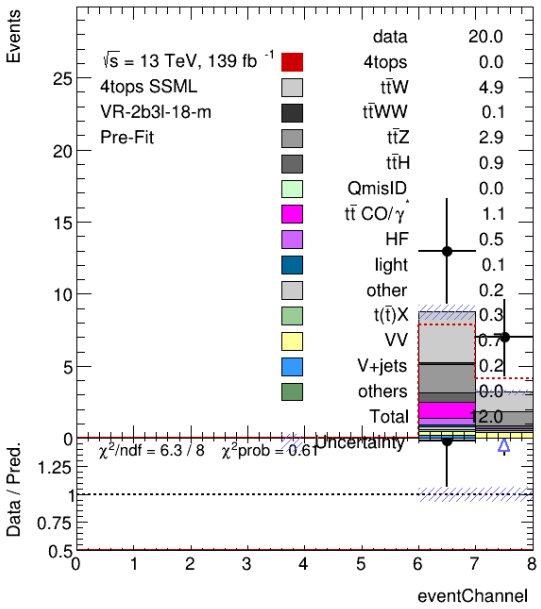


(c) $emm + mmm$ events, pre-fit

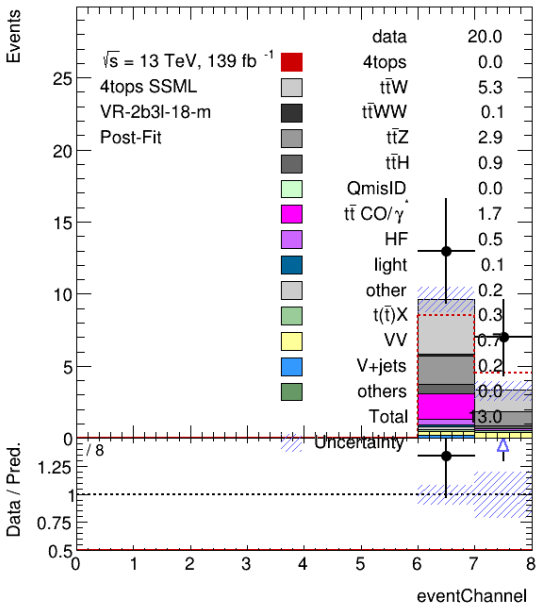


(d) $emm + mmm$ events, post-fit

Figure C.12: Flavour category split of the 2b3l validation region for the 2018 data taking period, showing the distribution of lepton flavour combinations within each category. Here a value of 4 represents $eee$ events, 5 for $eem$, 6 for $emm$, and 7 for $mmm$ events.

# Bibliography


[1] Glashow, SL 1961, 'Partial-symmetries of weak interactions', *Nuclear Physics*, vol. 22, no. 4, pp. 579 – 588, ISSN 0029-5582, URL https://doi.org/10.1016/0029-5582(61)90469-2.

[2] Weinberg, S 1967, 'A model of leptons', *Phys. Rev. Lett.*, vol. 19, pp. 1264–1266, doi:10.1103/PhysRevLett.19.1264, URL https://link.aps.org/doi/10.1103/PhysRevLett.19.1264.

[3] Salam, A 1980, 'Gauge unification of fundamental forces', *Rev. Mod. Phys.*, vol. 52, pp. 525–538, doi:10.1103/RevModPhys.52.525, URL https://link.aps.org/doi/10.1103/RevModPhys.52.525.

[4] CERN 2019, 'Standard Model particles', https://atlas.cern/sites/atlas-public.web.cern.ch/files/ATLAS-Standard-model-2.png, [Online; Accessed 3/10/2019].

[5] 2019, 'Standard Model Summary Plots Summer 2019', Tech. Rep. ATL-PHYS-PUB-2019-024, CERN, Geneva, URL http://cds.cern.ch/record/2682186.

[6] Zannoni, A 1999, 'On the quantization of the monoatomic ideal gas', https://arxiv.org/abs/cond-mat/9912229.

[7] Dirac, PAM 1926, 'On the theory of quantum mechanics', *Proceedings of the Royal Society of London. Series A, Containing Papers of a Mathematical and Physical Character*, vol. 112, no. 762, pp. 661–677, ISSN 09501207, URL http://www.jstor.org/stable/94692.

[8] Bose 1924, 'Plancks gesetz und lichtquantenhypothese', *Zeitschrift für Physik*, vol. 26, no. 1, pp. 178–181, ISSN 0044-3328, doi:10.1007/BF01327326.

[9] Englert, F & Brout, R 1964, 'Broken symmetry and the mass of gauge vector mesons', *Phys. Rev. Lett.*, vol. 13, pp. 321–323, doi:10.1103/PhysRevLett.13.321, URL https://link.aps.org/doi/10.1103/PhysRevLett.13.321.

[10] Higgs, PW 1964, 'Broken symmetries and the masses of gauge bosons', *Phys. Rev. Lett.*, vol. 13, pp. 508–509, doi:10.1103/PhysRevLett.13.508, URL https://link.aps.org/doi/10.1103/PhysRevLett.13.508.

[11] de Boer, W (CMS) 2013, The Discovery of the Higgs Boson with the CMS Detector and its Implications for Supersymmetry and Cosmology, URL http://inspirehep.net/record/1252561/files/arXiv:1309.0721.pdf.

[12] Abe, F, Akimoto, H, Akopian, A, Albrow, MG, Amendolia, SR, Amidei, D, Antos, J, Anway-Wiese, C, Aota, S, Apollinari, G *et al.* 1995, 'Observation of Top Quark Production in p-p Collisions with the Collider Detector at Fermilab', *Physical Review Letters*, vol. 74, no. 14, p. 26262631, ISSN 1079-7114, doi:10.1103/physrevlett.74.2626, URL http://dx.doi.org/10.1103/PhysRevLett.74.2626.

[13] Abachi, S, Abbott, B, Abolins, M, Acharya, BS, Adam, I, Adams, DL, Adams, M, Ahn, S, Aihara, H, Alitti, J *et al.* 1995, 'Observation of the top quark', *Physical Review Letters*, vol. 74, no. 14, p. 26322637, ISSN 1079-7114, doi:10.1103/physrevlett.74.2632, URL http://dx.doi.org/10.1103/PhysRevLett.74.2632.

[14] Tanabashi, M, Hagiwara, K, Hikasa, K, Nakamura, K, Sumino, Y, Takahashi, F, Tanaka, J, Agashe, K, Aielli, G, Amsler, C, Antonelli, M, Asner, DM, Baer, H, Banerjee, S, Barnett, RM, Basaglia, T, Bauer, CW, Beatty, JJ, Belousov, VI, Beringer, J, Bethke, S, Bettini, A, Bichsel, H, Biebel, O, Black, KM, Blucher, E, Buchmuller, O, Burkert, V, Bychkov, MA, Cahn, RN, Carena, M, Ceccucci, A, Cerri, A, Chakraborty, D, Chen, MC, Chivukula, RS, Cowan, G, Dahl, O, D'Ambrosio, G, Damour, T, de Florian, D, de Gouvêa, A, DeGrand, T, de Jong, P, Dissertori, G, Dobrescu, BA, D'Onofrio, M, Doser, M, Drees, M, Dreiner, HK, Dwyer, DA, Eerola, P, Eidelman, S, Ellis, J, Erler, J, Ezhela, VV, Fetscher, W, Fields, BD, Firestone, R, Foster, B, Freitas, A, Gallagher, H, Garren, L, Gerber, HJ, Gerbier, G, Gershon, T, Gershtein, Y, Gherghetta, T, Godizov, AA, Goodman, M, Grab, C, Gritsan, AV, Grojean, C, Groom, DE, Grünewald, M, Gurtu, A, Gutsche, T, Haber, HE, Hanhart, C, Hashimoto, S, Hayato, Y, Hayes, KG, Hebecker, A, Heinemeyer, S, Heltsley, B, Hernández-Rey, JJ, Hisano, J, Höcker, A, Holder, J, Holtkamp, A, Hyodo, T, Irwin, KD, Johnson, KF, Kado, M, Karliner, M, Katz, UF, Klein, SR, Klempt, E, Kowalewski, RV, Krauss, F, Kreps, M, Krusche, B, Kuyanov, YV, Kwon, Y, Lahav, O, Laiho, J, Lesgourgues, J, Liddle, A, Ligeti, Z, Lin, CJ, Lippmann, C, Liss, TM, Littenberg, L, Lugovsky, KS, Lugovsky, SB, Lusiani, A, Makida, Y, Maltoni, F, Mannel, T, Manohar, AV, Marciano, WJ, Martin, AD, Masoni, A, Matthews, J, Meißner, UG, Milstead, D, Mitchell, RE, Mönig, K, Molaro, P, Moortgat, F, Moskovic, M, Murayama, H, Narain, M, Nason, P, Navas, S, Neubert, M, Nevski, P, Nir, Y, Olive, KA, Pagan Griso, S, Parsons, J, Patrignani, C, Peacock, JA, Pennington, M, Petcov, ST, Petrov, VA, Pianori, E, Piepke, A, Pomarol, A, Quadt, A, Rademacker, J, Raffelt, G, Ratcliff, BN, Richardson, P, Ringwald, A, Roesler, S, Rolli, S, Romaniouk, A, Rosenberg, LJ, Rosner, JL, Rybka, G, Ryutin, RA, Sachrajda, CT, Sakai, Y, Salam, GP, Sarkar, S, Sauli, F, Schneider, O, Scholberg, K, Schwartz, AJ, Scott, D, Sharma, V, Sharpe, SR, Shutt, T, Silari, M, Sjöstrand, T, Skands, P, Skwarnicki, T, Smith, JG, Smoot, GF, Spanier, S, Spieler, H, Spiering, C, Stahl, A, Stone, SL, Sumiyoshi, T, Syphers, MJ, Terashi, K, Terning, J, Thoma, U, Thorne, RS, Tiator, L, Titov,

M, Tkachenko, NP, Törnqvist, NA, Tovey, DR, Valencia, G, Van de Water, R, Varelas, N, Venanzoni, G, Verde, L, Vincter, MG, Vogel, P, Vogt, A, Wakely, SP, Walkowiak, W, Walter, CW, Wands, D, Ward, DR, Wascko, MO, Weiglein, G, Weinberg, DH, Weinberg, EJ, White, M, Wiencke, LR, Willocq, S, Wohl, CG, Womersley, J, Woody, CL, Workman, RL, Yao, WM, Zeller, GP, Zenin, OV, Zhu, RY, Zhu, SL, Zimmermann, F, Zyla, PA, Anderson, J, Fuller, L, Lugovsky, VS & Schaffner, P (Particle Data Group) 2018, 'Review of Particle Physics', *Phys. Rev. D*, vol. 98, p. 030001, doi:10.1103/PhysRevD.98.030001, URL https://link.aps.org/doi/10.1103/PhysRevD.98.030001.

[15] The ATLAS Collaboration 2019, 'Luminosity determination in *pp* collisions at $\sqrt{s} = 13$ TeV using the ATLAS detector at the LHC', Tech. Rep. ATLAS-CONF-2019-021, CERN, Geneva, URL http://cds.cern.ch/record/2677054.

[16] The ATLAS Collaboration 2019, 'Luminosity Public Results Run 2', https://twiki.cern.ch/twiki/bin/view/AtlasPublic/LuminosityPublicResultsRun2, [Online; Accessed 9/10/2019].

[17] The ATLAS Collaboration 2008, 'The ATLAS experiment at the CERN large hadron collider', *Journal of Instrumentation*, vol. 3, no. 08, pp. S08003–S08003, doi:10.1088/1748-0221/3/08/s08003, URL https://doi.org/10.1088%2F1748-0221%2F3%2F08%2Fs08003.

[18] CERN 2008, 'Computer generated image of the whole ATLAS detector', https://cds.cern.ch/images/CERN-GE-0803012-01, [Online; Accessed 10/10/2019].

[19] Vrba, V 2001, 'The ATLAS pixel detector', *Nuclear Instruments and Methods in Physics Research Section A: Accelerators, Spectrometers, Detectors and Associated Equipment*, vol. 465, no. 1, pp. 27 – 33, ISSN 0168-9002, doi:https://doi.org/10.1016/S0168-9002(01)00342-4, sPD2000.

[20] Haywood, S, Rossi, L, Nickerson, R & Romaniouk, A (ATLAS Collaboration) 1997, ATLAS inner detector: Technical Design Report, 2, Technical Design Report ATLAS, CERN, Geneva, URL https://cds.cern.ch/record/331064.

[21] Aaboud, M, Aad, G, Abbott, B, Abdallah, J, Abdinov, O, Abeloos, B, Abidi, S, AbouZeid, O, Abraham, N, Abramowicz, H *et al.* 2017, 'Performance of the ATLAS Transition Radiation Tracker in Run 1 of the LHC: tracker properties', *Journal of Instrumentation*, vol. 12, no. 05, p. P05002P05002, ISSN 1748-0221, doi:10.1088/1748-0221/12/05/p05002, URL http://dx.doi.org/10.1088/1748-0221/12/05/P05002.

[22] Marcisovsky, M 2011, 'ATLAS insertable B-layer', *Nuclear Instruments and Methods in Physics Research Section A: Accelerators, Spectrometers, Detectors and Associated Equipment*, vol. 633, pp. S224 – S225, ISSN 0168-9002, doi:https://doi.org/10.1016/j.nima.2010.06.173, 11th International Workshop on Radiation Imaging Detectors (IWORID).

[23] CERN 2008, 'Computer generated image of the ATLAS inner detector', https://cds.cern.ch/images/CERN-GE-0803014-01, [Online; Accessed 1/10/2019].

[24] Aaboud, M, Aad, G, Abbott, B, Abdallah, J, Abdinov, O, Abeloos, B, Aben, R, AbouZeid, OS, Abraham, NL *et al.* 2016, 'Luminosity determination in pp collisions at $\sqrt{s} = 8$ tev using the ATLAS detector at the LHC', *The European Physical Journal C*, vol. 76, no. 12, ISSN 1434-6052, doi:10.1140/epjc/s10052-016-4466-1.

[25] Aaboud, M, Aad, G, Abbott, B, Abdallah, J, Abdinov, O, Abeloos, B, Aben, R, AbouZeid, OS, Abraham, NL *et al.* 2017, 'Performance of the ATLAS trigger system in 2015', *The European Physical Journal C*, vol. 77, no. 5, ISSN 1434-6052, doi:10.1140/epjc/s10052-017-4852-3, URL http://dx.doi.org/10.1140/epjc/s10052-017-4852-3.

[26] Panduro Vazquez, W (ATLAS Collaboration) 2017, 'The ATLAS Data Acquisition system in LHC Run 2', Tech. Rep. ATL-DAQ-PROC-2017-007. 3, CERN, Geneva, doi:10.1088/1742-6596/898/3/032017.

[27] Salzburger, A 2007, 'The ATLAS Track Extrapolation Package', http://inspirehep.net/record/1196562/.

[28] The ATLAS Collaboration 2015, 'The Optimization of ATLAS Track Reconstruction in Dense Environments', Tech. Rep. ATL-PHYS-PUB-2015-006, CERN, Geneva, URL https://cds.cern.ch/record/2002609.

[29] Aaboud, M, Aad, G, Abbott, B, Abdallah, J, Abdinov, O, Abeloos, B, Abidi, SH, AbouZeid, OS, Abraham, NL *et al.* 2017, 'Performance of the ATLAS track reconstruction algorithms in dense environments in LHC Run 2', *The European Physical Journal C*, vol. 77, no. 10, ISSN 1434-6052, doi:10.1140/epjc/s10052-017-5225-7, URL http://dx.doi.org/10.1140/epjc/s10052-017-5225-7.

[30] Lampl, W, Laplace, S, Lelas, D, Loch, P, Ma, H, Menke, S, Rajagopalan, S, Rousseau, D, Snyder, S & Unal, G 2008, 'Calorimeter Clustering Algorithms: Description and Performance', Tech. Rep. ATL-LARG-PUB-2008-002. ATL-COM-LARG-2008-003, CERN, Geneva, URL https://cds.cern.ch/record/1099735.

[31] Aaboud, M *et al.* (ATLAS) 2019, 'Electron reconstruction and identification in the ATLAS experiment using the 2015 and 2016 LHC proton-proton collision data at $\sqrt{s} = 13$ TeV', *Eur. Phys. J.*, vol. C79, no. 8, p. 639, doi:10.1140/epjc/s10052-019-7140-6, 1902.04655.

[32] Aad, G *et al.* (ATLAS) 2016, 'Muon reconstruction performance of the ATLAS detector in protonproton collision data at $\sqrt{s}$ =13 TeV', *Eur. Phys. J.*, vol. C76, no. 5, p. 292, doi:10.1140/epjc/s10052-016-4120-y, 1603.05598.

[33] Aad, G *et al.* (ATLAS) 2017, 'Topological cell clustering in the ATLAS calorimeters and its performance in LHC Run 1', *Eur. Phys. J.*, vol. C77, p. 490, doi:10.1140/epjc/s10052-017-5004-5, 1603.02934.

[34] Cacciari, M, Salam, GP & Soyez, G 2008, 'The anti-ktjet clustering algorithm', *Journal of High Energy Physics*, vol. 2008, no. 04, pp. 063–063, doi:10.1088/1126-6708/2008/04/063, URL https://doi.org/10.1088%2F1126-6708%2F2008%2F04%2F063.

[35] Aad, G *et al.* (ATLAS) 2019, 'ATLAS b-jet identification performance and efficiency measurement with $t\bar{t}$ events in pp collisions at $\sqrt{s} = 13$ TeV', *Eur. Phys. J.*, vol. C79, no. 11, p. 970, doi:10.1140/epjc/s10052-019-7450-8, 1907.05120.

[36] 2017, 'Optimisation and performance studies of the ATLAS $b$-tagging algorithms for the 2017-18 LHC run', Tech. Rep. ATL-PHYS-PUB-2017-013, CERN, Geneva, URL https://cds.cern.ch/record/2273281.

[37] Aad, G *et al.* (ATLAS) 2015, 'Identification and energy calibration of hadronically decaying tau leptons with the ATLAS experiment in $pp$ collisions at $\sqrt{s}$=8 TeV', *Eur. Phys. J.*, vol. C75, no. 7, p. 303, doi:10.1140/epjc/s10052-015-3500-z, 1412.7086.

[38] Höche, S 2015, 'Introduction to parton-shower event generators', in 'Proceedings, Theoretical Advanced Study Institute in Elementary Particle Physics: Journeys Through the Precision Frontier: Amplitudes for Colliders (TASI 2014): Boulder, Colorado, June 2-27, 2014', pp. 235–295, doi:10.1142/9789814678766_0005, 1411.4085.

[39] Agostinelli, S, Allison, J, Amako, K, Apostolakis, J, Araujo, H, Arce, P, Asai, M, Axen, D, Banerjee, S, Barrand, G, Behner, F, Bellagamba, L, Boudreau, J, Broglia, L, Brunengo, A, Burkhardt, H, Chauvie, S, Chuma, J, Chytracek, R, Cooperman, G, Cosmo, G, Degtyarenko, P, Dell'Acqua, A, Depaola, G, Dietrich, D, Enami, R, Feliciello, A, Ferguson, C, Fesefeldt, H, Folger, G, Foppiano, F, Forti, A, Garelli, S, Giani, S, Giannitrapani, R, Gibin, D, Cadenas, JG, Gonzlez, I, Abril, GG, Greeniaus, G, Greiner, W, Grichine, V, Grossheim, A, Guatelli, S, Gumplinger, P, Hamatsu, R, Hashimoto, K, Hasui, H, Heikkinen, A, Howard, A, Ivanchenko, V, Johnson, A, Jones, F, Kallenbach, J, Kanaya, N, Kawabata, M, Kawabata, Y, Kawaguti, M, Kelner, S, Kent, P, Kimura, A, Kodama, T, Kokoulin, R, Kossov, M, Kurashige, H, Lamanna, E, Lampn, T, Lara, V, Lefebure, V, Lei, F, Liendl, M, Lockman, W, Longo, F, Magni, S, Maire, M, Medernach, E, Minamimoto, K, de Freitas, PM, Morita, Y, Murakami, K, Nagamatu, M, Nartallo, R, Nieminen, P, Nishimura, T, Ohtsubo, K, Okamura, M, O'Neale, S, Oohata, Y, Paech, K, Perl, J, Pfeiffer, A, Pia, M, Ranjard, F, Rybin, A, Sadilov, S, Salvo, ED, Santin, G, Sasaki, T, Savvas, N, Sawada, Y, Scherer, S, Sei, S, Sirotenko, V, Smith, D, Starkov, N, Stoecker, H, Sulkimo, J, Takahata, M, Tanaka, S, Tcherniaev, E, Tehrani, ES, Tropeano, M, Truscott,

P, Uno, H, Urban, L, Urban, P, Verderi, M, Walkden, A, Wander, W, Weber, H, Wellisch, J, Wenaus, T, Williams, D, Wright, D, Yamada, T, Yoshida, H & Zschiesche, D 2003, 'Geant4 - a simulation toolkit', *Nuclear Instruments and Methods in Physics Research Section A: Accelerators, Spectrometers, Detectors and Associated Equipment*, vol. 506, no. 3, pp. 250 – 303, ISSN 0168-9002, URL https://doi.org/10.1016/S0168-9002(03)01368-8.

[40] Richter-Was, E, Froidevaux, D & Poggioli, L 1998, 'ATLFAST 2.0 a fast simulation package for ATLAS', Tech. Rep. ATL-PHYS-98-131, CERN, Geneva, URL https://cds.cern.ch/record/683751.

[41] Maznas, Ioannis 2017, 'FTK: The hardware Fast TracKer of the ATLAS experiment at CERN', *EPJ Web Conf.*, vol. 137, p. 12001, doi:10.1051/epjconf/201713712001, URL https://doi.org/10.1051/epjconf/201713712001.

[42] Shochet, M, Tompkins, L, Cavaliere, V, Giannetti, P, Annovi, A & Volpi, G 2013, 'Fast TracKer (FTK) Technical Design Report', Tech. Rep. CERN-LHCC-2013-007. ATLAS-TDR-021, ATLAS Fast Tracker Technical Design Report, URL https://cds.cern.ch/record/1552953.

[43] The ATLAS Collaboration 2017, 'Technical Design Report for the Phase-II Upgrade of the ATLAS TDAQ System', Tech. Rep. CERN-LHCC-2017-020. ATLAS-TDR-029, CERN, Geneva, URL https://cds.cern.ch/record/2285584.

[44] Apollinari, G, Bjar, AI, Brning, O, Fessia, P, Lamont, M, Rossi, L & Tavian, L 2017, High-Luminosity Large Hadron Collider (HL-LHC): Technical Design Report V. 0.1, CERN Yellow Reports: Monographs, CERN, Geneva, doi:10.23731/CYRM-2017-004, URL http://cds.cern.ch/record/2284929.

[45] The ATLAS Collaboration 2012, 'Performance of the ATLAS Inner Detector Track and Vertex Reconstruction in the High Pile-Up LHC Environment', Tech. Rep. ATLAS-CONF-2012-042, CERN, Geneva, URL https://cds.cern.ch/record/1435196.

[46] Sotiropoulou, C, Maznas, I, Citraro, S, Annovi, A, Ancu, LS, Beccherle, R, Bertolucci, F, Biesuz, N, Calabr, D, Crescioli, F, Dimas, D, DellOrso, M, Donati, S, Gentsos, C, Giannetti, P, Gkaitatzis, S, Gramling, J, Greco, V, Kalaitzidis, P, Kordas, K, Kimura, N, Kubota, T, Iovene, A, Lanza, A, Luciano, P, Magnin, B, Mermikli, K, Nasimi, H, Negri, A, Nikolaidis, S, Piendibene, M, Sakellariou, A, Sampsonidis, D & Volpi, G 2017, 'The Associative Memory System Infrastructures for the ATLAS Fast Tracker', *IEEE Transactions on Nuclear Science*, vol. 64, no. 6, pp. 1248–1254, ISSN 1558-1578, doi:10.1109/TNS.2017.2703908.

[47] Ristori, L 2000, 'An artificial retina for fast track finding', *Nuclear Instruments and Methods in Physics Research Section A: Accelerators, Spectrometers,*

*Detectors and Associated Equipment*, vol. 453, no. 1, pp. 425 – 429, ISSN 0168-9002, doi:https://doi.org/10.1016/S0168-9002(00)00676-8, proc. 7th Int. Conf on Instrumentation for colliding Beam Physics.

[48] Amendolia, S, Galeotti, S, Morsani, F, Passuello, D, Ristori, L & Turini, N 1992, 'The AMchip: a VLSI associative memory for track finding', *Nuclear Instruments and Methods in Physics Research Section A: Accelerators, Spectrometers, Detectors and Associated Equipment*, vol. 315, no. 1, pp. 446 – 448, ISSN 0168-9002, doi:https://doi.org/10.1016/0168-9002(92)90744-O.

[49] The ATLAS Collaboration, Åkesson, T, Eerola, P, Hedberg, V, Jarlskog, G, Lundberg, B, Mjörnmark, U, Smirnova, O, Almehed, S & al. et 2005, ATLAS computing: Technical Design Report, vol. ATLAS TDR-017; CERN-LHCC-2005-022 of *LHCC Reports; ATLAS Techical Design Reports*, CERN, ISBN 92-9083-250-9.

[50] Nilles, HP 1984, 'Supersymmetry, Supergravity and Particle Physics', *Phys. Rept.*, vol. 110, pp. 1–162, doi:10.1016/0370-1573(84)90008-5.

[51] Farrar, GR & Fayet, P 1978, 'Phenomenology of the Production, Decay, and Detection of New Hadronic States Associated with Supersymmetry', *Phys. Lett.*, vol. 76B, pp. 575–579, doi:10.1016/0370-2693(78)90858-4.

[52] Plehn, T & Tait, TMP 2009, 'Seeking Sgluons', *J. Phys.*, vol. G36, p. 075001, doi:10.1088/0954-3899/36/7/075001, 0810.3919.

[53] Calvet, S, Fuks, B, Gris, P & Valery, L 2013, 'Searching for sgluons in multitop events at a center-of-mass energy of 8 TeV', *JHEP*, vol. 04, p. 043, doi:10.1007/JHEP04(2013)043, 1212.3360.

[54] Dicus, D, Stange, A & Willenbrock, S 1994, 'Higgs decay to top quarks at hadron colliders', *Phys. Lett.*, vol. B333, pp. 126–131, doi:10.1016/0370-2693(94)91017-0, hep-ph/9404359.

[55] Craig, N, D'Eramo, F, Draper, P, Thomas, S & Zhang, H 2015, 'The Hunt for the Rest of the Higgs Bosons', *JHEP*, vol. 06, p. 137, doi:10.1007/JHEP06(2015)137, 1504.04630.

[56] Craig, N, Hajer, J, Li, YY, Liu, T & Zhang, H 2017, 'Heavy Higgs bosons at low $\tan\beta$: from the LHC to 100 TeV', *JHEP*, vol. 01, p. 018, doi:10.1007/JHEP01(2017)018, 1605.08744.

[57] Frederix, R, Pagani, D & Zaro, M 2018, 'Large NLO corrections in $t\bar{t}W^{\pm}$ and $t\bar{t}t\bar{t}$ hadroproduction from supposedly subleading EW contributions', *JHEP*, vol. 02, p. 031, doi:10.1007/JHEP02(2018)031, 1711.02116.

[58] Avoni, G *et al.* 2018, 'The new LUCID-2 detector for luminosity measurement and monitoring in ATLAS', *JINST*, vol. 13, no. 07, p. P07017, doi:10.1088/1748-0221/13/07/P07017.

[59] Alwall, J, Frederix, R, Frixione, S, Hirschi, V, Maltoni, F, Mattelaer, O, Shao, HS, Stelzer, T, Torrielli, P & Zaro, M 2014, 'The automated computation of tree-level and next-to-leading order differential cross sections, and their matching to parton shower simulations', *JHEP*, vol. 1407, p. 079, doi:10.1007/JHEP07(2014)079, 1405.0301.

[60] NNPDF Collaboration, R.D. Ball and others (NNPDF) 2015, 'Parton distributions for the LHC Run II', *JHEP*, vol. 04, p. 040, doi:10.1007/JHEP04(2015)040, 1410.8849.

[61] Frixione, S, Laenen, E, Motylinski, P & Webber, BR 2007, 'Angular correlations of lepton pairs from vector boson and top quark decays in Monte Carlo simulations', *JHEP*, vol. 0704, p. 081, doi:10.1088/1126-6708/2007/04/081, hep-ph/0702198.

[62] Artoisenet, P, Frederix, R, Mattelaer, O & Rietkerk, R 2013, 'Automatic spin-entangled decays of heavy resonances in Monte Carlo simulations', *JHEP*, vol. 1303, p. 015, doi:10.1007/JHEP03(2013)015, 1212.3460.

[63] Sjöstrand, T, Ask, S, Christiansen, JR, Corke, R, Desai, N, Ilten, P, Mrenna, S, Prestel, S, Rasmussen, CO & Skands, PZ 2015, 'An Introduction to PYTHIA 8.2', *Comput. Phys. Commun.*, vol. 191, pp. 159–177, doi:10.1016/j.cpc.2015.01.024, 1410.3012.

[64] The ATLAS Collaboration 2014, 'ATLAS Pythia 8 tunes to 7 TeV data', ATL-PHYS-PUB-2014-021, https://cds.cern.ch/record/1966419.

[65] D. J. Lange 2001, 'The EvtGen particle decay simulation package', *Nucl. Instrum. Meth. A*, vol. 462, p. 152, doi:10.1016/S0168-9002(01)00089-4.

[66] Frixione, S, Nason, P & Ridolfi, G 2007, 'A Positive-weight next-to-leading-order Monte Carlo for heavy flavour hadroproduction', *JHEP*, vol. 09, p. 126, doi:10.1088/1126-6708/2007/09/126, 0707.3088.

[67] Nason, P 2004, 'A New method for combining NLO QCD with shower Monte Carlo algorithms', *JHEP*, vol. 0411, p. 040, doi:10.1088/1126-6708/2004/11/040, hep-ph/0409146.

[68] Frixione, S, Nason, P & Oleari, C 2007, 'Matching NLO QCD computations with Parton Shower simulations: the POWHEG method', *JHEP*, vol. 11, p. 070, doi:10.1088/1126-6708/2007/11/070, 0709.2092.

[69] Alioli, S, Nason, P, Oleari, C & Re, E 2010, 'A general framework for implementing NLO calculations in shower Monte Carlo programs: the POWHEG BOX', *JHEP*, vol. 1006, p. 043, doi:10.1007/JHEP06(2010)043, 1002.2581.

[70] ATLAS Collaboration 2016, 'Studies on top-quark Monte Carlo modelling for Top2016', ATL-PHYS-PUB-2016-020, https://cds.cern.ch/record/2216168.

[71] Re, E 2011, 'Single-top Wt-channel production matched with parton showers using the POWHEG method', *Eur. Phys. J. C*, vol. 71, p. 1547, doi:10.1140/epjc/s10052-011-1547-z, 1009.2450.

[72] Frederix, R, Re, E & Torrielli, P 2012, 'Single-top t-channel hadroproduction in the four-flavour scheme with POWHEG and aMC@NLO', *JHEP*, vol. 09, p. 130, doi:10.1007/JHEP09(2012)130, 1207.5391.

[73] Bothmann, E *et al.* 2019, 'Event Generation with Sherpa 2.2', 1905.09127.

[74] Cascioli, F, Maierhofer, P & Pozzorini, S 2012, 'Scattering Amplitudes with Open Loops', *Phys. Rev. Lett.*, vol. 108, p. 111601, doi:10.1103/PhysRevLett.108.111601, 1111.5206.

[75] Denner, A, Dittmaier, S & Hofer, L 2017, 'Collier: a fortran-based Complex One-Loop LIbrary in Extended Regularizations', *Comput. Phys. Commun.*, vol. 212, pp. 220–238, doi:10.1016/j.cpc.2016.10.013, 1604.06792.

[76] Schumann, S & Krauss, F 2008, 'A Parton shower algorithm based on Catani-Seymour dipole factorisation', *JHEP*, vol. 03, p. 038, doi:10.1088/1126-6708/2008/03/038, 0709.1027.

[77] Hoeche, S, Krauss, F, Schonherr, M & Siegert, F 2012, 'A critical appraisal of NLO+PS matching methods', *JHEP*, vol. 09, p. 049, doi:10.1007/JHEP09(2012)049, 1111.1220.

[78] Hoeche, S, Krauss, F, Schonherr, M & Siegert, F 2013, 'QCD matrix elements + parton showers: The NLO case', *JHEP*, vol. 04, p. 027, doi:10.1007/JHEP04(2013)027, 1207.5030.

[79] Catani, S, Krauss, F, Kuhn, R & Webber, BR 2001, 'QCD matrix elements + parton showers', *JHEP*, vol. 11, p. 063, doi:10.1088/1126-6708/2001/11/063, hep-ph/0109231.

[80] Hoeche, S, Krauss, F, Schumann, S & Siegert, F 2009, 'QCD matrix elements and truncated showers', *JHEP*, vol. 05, p. 053, doi:10.1088/1126-6708/2009/05/053, 0903.1219.

[81] Gleisberg, T & Hoeche, S 2008, 'Comix, a new matrix element generator', *JHEP*, vol. 12, p. 039, doi:10.1088/1126-6708/2008/12/039, 0808.3674.

[82] Anastasiou, C, Dixon, LJ, Melnikov, K & Petriello, F 2004, 'High precision QCD at hadron colliders: Electroweak gauge boson rapidity distributions at NNLO', *Phys. Rev. D*, vol. 69, p. 094008, doi:10.1103/PhysRevD.69.094008, hep-ph/0312266.

[83] Albertsson, K 2018, 'TMVA Summary', https://root.cern.ch/tmva/summary, [Online; Accessed 5/2/2020].

[84] Zhang, C 2017, 'Theoretical aspects of the study of top quark properties', 1708.09201.